

FINAL REPORT

Compact, Low-Noise Magnetic Sensor with Fluxgate (DC) and Induction (AC) Modes of Operation

SERDP Project MM-1444

JULY 2009

Dr. Yongming Zhang, Ph.D

QUASAR Federal Systems, Inc.
5754 Pacific Center Blvd. Suite 203
San Diego, CA 92121

This document has been approved for public release.



Strategic Environmental Research and
Development Program

Report Documentation Page				Form Approved OMB No. 0704-0188	
Public reporting burden for the collection of information is estimated to average 1 hour per response, including the time for reviewing instructions, searching existing data sources, gathering and maintaining the data needed, and completing and reviewing the collection of information. Send comments regarding this burden estimate or any other aspect of this collection of information, including suggestions for reducing this burden, to Washington Headquarters Services, Directorate for Information Operations and Reports, 1215 Jefferson Davis Highway, Suite 1204, Arlington VA 22202-4302. Respondents should be aware that notwithstanding any other provision of law, no person shall be subject to a penalty for failing to comply with a collection of information if it does not display a currently valid OMB control number.					
1. REPORT DATE JUL 2009		2. REPORT TYPE N/A		3. DATES COVERED -	
4. TITLE AND SUBTITLE Compact, Low-Noise Magnetic Sensor with Fluxgate (DC) and Induction (AC) Modes of Operation				5a. CONTRACT NUMBER	
				5b. GRANT NUMBER	
				5c. PROGRAM ELEMENT NUMBER	
6. AUTHOR(S)				5d. PROJECT NUMBER	
				5e. TASK NUMBER	
				5f. WORK UNIT NUMBER	
7. PERFORMING ORGANIZATION NAME(S) AND ADDRESS(ES) QUASAR Federal Systems, Inc. 5754 Pacific Center Blvd. Suite 203 San Diego, CA 92121				8. PERFORMING ORGANIZATION REPORT NUMBER	
9. SPONSORING/MONITORING AGENCY NAME(S) AND ADDRESS(ES)				10. SPONSOR/MONITOR'S ACRONYM(S)	
				11. SPONSOR/MONITOR'S REPORT NUMBER(S)	
12. DISTRIBUTION/AVAILABILITY STATEMENT Approved for public release, distribution unlimited					
13. SUPPLEMENTARY NOTES The original document contains color images.					
14. ABSTRACT					
15. SUBJECT TERMS					
16. SECURITY CLASSIFICATION OF:			17. LIMITATION OF ABSTRACT UU	18. NUMBER OF PAGES 86	19a. NAME OF RESPONSIBLE PERSON
a. REPORT unclassified	b. ABSTRACT unclassified	c. THIS PAGE unclassified			

This report was prepared under contract to the Department of Defense Strategic Environmental Research and Development Program (SERDP). The publication of this report does not indicate endorsement by the Department of Defense, nor should the contents be construed as reflecting the official policy or position of the Department of Defense. Reference herein to any specific commercial product, process, or service by trade name, trademark, manufacturer, or otherwise, does not necessarily constitute or imply its endorsement, recommendation, or favoring by the Department of Defense.

TABLE OF CONTENTS

Table of Contents	i
List of Tables	iii
List of Figures	iv
List of Acronyms	viii
Keywords	viii
Acknowledgement	viii
Abstract	ix
1. Project Objective and Approach	1
2. Background	2
2.1 The need for combined AC and DC magnetic sensors	2
2.2 Innovation of this work	2
2.3 TDEM measurement	3
2.4 Challenges for using high-permeability induction sensor	3
2.5 Requirements	3
2.6 Comparison with commercial and R&D systems	4
3. Work Summary	5
4. Materials and Methods - Sensor Development	10
5. Materials and Methods - Research Prototype	12
5.1 Receiver system overview	12
5.2 Dual-mode sensor	13
5.2.1 Dual-mode sensing probe	13
5.2.2. Receiver circuit board	22
5.3 DAQ and software	24
5.4 Other system components	26
5.5 Dual-mode operation	26
5.5.1 Dual-mode operation with serial time-sharing	26
5.5.2 Dual-mode operation with interleaved time sharing	28
6. Materials and Methods - DATA Modeling	30
6.1 EM induction	30
6.2 DC magnetometry	31
6.3 Bandwidth requirements	31
7. Results and Discussion - System Performance	35
7.1 Sensor performance	35
7.1.1 EM induction	35

7.1.2 DC magnetometry	38
7.1.3 Discussion on the comparison results	40
7.2 Three-component data	41
7.3 Receiver system performance summary	43
8. Results and Discussion – Target Discrimination	45
8.1 TD3D implementation	45
8.2 Ordnance discrimination by shape classification.....	45
8.3 Results.....	46
8.3.1 EM induction	46
8.3.2 DC magnetometry	57
8.4 Concluding discussion on FIS data.....	60
9. Results and Discussion - Field Deployment Studies	60
9.1 Current monitor and background drift	60
9.2 Develop system for outdoor operation.....	62
9.3 Spatial resolution of scan-in-motion operation.....	62
9.4 Environmental effects	66
9.5 Motion effects	70
9.6 Conclusions on field deployment issues	71
10. Conclusions and Implications for Future Research	72
Future Research	73
Literature Cited	74
Appendices.....	75
List of Scientific/Technical Publications	75

LIST OF TABLES

Table 1 - Comparison of FIS with commercial and other advanced R&D systems	5
Table 2 - Options for obtaining an existing transmitter that has a fast turnoff or/and larger moment than our existing transmitter (coil #1B)	9
Table 3 - Properties of compact coils	15
Table 4 - Improving the 3” coil with Kapton tape between winding layers	16
Table 5 - Improving the coil with multi-section winding	17
Table 6 - Properties of different core materials.....	17
Table 7 - Coil properties with different cores	18
Table 8 - Time-Domain Model Parameters for Selected Ordnance	33
Table 9 - Median Frequencies of Peak Quadrature Responses	33
Table 10 - TD3D model results	37
Table 12 - Comparison of TD3D modeling between vertical IS and 3-axis IS.	43
Table 13 - Operational Parameters of FIS system.....	44
Table 14 - Single-axis (sphere) fits for 47-cm and 75-cm height data.....	54
Table 15 - Two- and three-axis fits, classification, and representative inversion results (VR, position X, Y, Z of the target in meter, rotations in degree, and shape parameters)....	55
Table 16 - Model fit based on measured magnetic data.....	58

LIST OF FIGURES

Figure 1.1 - Overall technical approach.....	1
Figure 2.1 - Cross-sectional view of the dual-mode sensor probe. The same coils are used for both the induction sensor and the fluxgate magnetometer.	2
Figure 3.1 - Impulse response of a 4” long coil (#6) with P cores ($L = 70.8$ mH, damping $R = 27.5$ kOhm each side). The field strength at the sensor location from the peak primary field is about $30 \mu\text{T}$. (a) DAQ card at low resolution; (b) DAQ card at a higher resolution (the output voltage has been divided by the amplifier gain).....	6
Figure 3.2 - Block diagram of the Year 2, Task 2 fluxgate magnetometer.	6
Figure 3.3 - FIS-prototype magnetic-field induction response collected in Year 2 for Left) a 37-mm vertical projectile (blue crosses) at 31 cm below Tx, and time-domain model fit (red line), and bin-averaged data (red dots). Right) 20-mm projectile at 23-cm and 31-cm. Black and green crosses are measured data. The magnetic moment of Tx coil is $3.5 \text{ A}\cdot\text{m}^2$ for the data collected.	7
Figure 3.4 - Year 2 testing setup to quantify dual-mode sensor operation. The driver generates 2 Amps bi-polar currents in the Tx coil ($200 \mu\text{T}$ field in the coil center), with a decay time constant of $20 \mu\text{s}$, and a total turn-off time of $100 \mu\text{s}$ (moment of $80 \text{ A}\cdot\text{m}^2$) and $150 \mu\text{s}$ (for $160 \text{ A}\cdot\text{m}^2$).	8
Figure 3.5 - Year 4 testing setup (research prototype system) for evaluating fluxgate-induction sensor. The Rx coil sits in the middle of the Tx coil, 47 cm above a test grid. The transmit coil and a driver generate a magnetic moment of $420 \text{ A}\cdot\text{m}^2$ and have a recovery time of about $220 \mu\text{s}$	10
Figure 4.1 - System architecture for measuring the sensor impulse response. Same architecture was used for later systems except coil size and magnetic moment were greatly increased for characterizing the sensor performance in target detection.	11
Figure 4.2 - Year 1 testing setup for measuring sensor impulse response, especially the core material evaluation. The Tx coil is constructed with 20 turns of copper strip and has a diameter of 35 cm. The setup generates a step field with a decay time of less than $30 \mu\text{s}$, from about $100 \mu\text{T}$ to less than 50 pT	11
Figure 5.1 - System block diagram for FIS receiver.....	13
Figure 5.2 - Dual mode receiver probe. Left: a photo of the 3-axis probe; Right: details of the probe. Two ferrite core excitation coils sit inside one larger diameter induction coil. Bucking coil is implemented one the Z-axis coil (blue wire).	14
Figure 5.3 - Photo of coils built under this task for evaluation.....	15
Figure 5.4 - Improving the 6” coil with Kapton tape between winding layers.....	16
Figure 5.5 - (a) Coil former for multi-section winding. A 3” long nanocrystalline bar is also shown (b) Coil #6 made of multi-section winding (four 1” long P-rods at background). An anti-pulsing coil was wound for the anti-pulsing study	16

Figure 5.6 - Impulse response of coil #1 with different core materials (a) Nanocrystalline bar; (b) Ferrite 78 rods; (c) P-1103 rods	19
Figure 5.7 - Detection of a small target with coil-6 and P-cores at two different amplifier gains. The voltage on the plot is the sensor output voltage divided by the amplifier gain. The orange line is the sensor response with the target, the blue line is the background response (without the target), and the red line is the difference between two responses.	20
Figure 5.8 - Anti-pulsing Approach to reduce the field in the core	21
Figure 5.9 - High-level circuit diagram for the dual-mode receiver. Multiple switches on the circuit board control the operation mode.	23
Figure 5.10 - Electronics of 3-axis dual-model receiver.....	23
Figure 5.11 - Flow-chart of the program, for an FIS receiver operating in dual-mode operation between the induction sensor (IS) mode and fluxgate (FG) mode.....	24
Figure 5.12 - User Interface for the dual-mode sensor	25
Figure 5.13 - Timing for the dual-mode operation with serial time-sharing during one scan. Inset shows the timing for the excitation current.	27
Figure 5.14 - Dual-Mode Sensor Response for 37 mm & 40 mm shell aligned in the vertical direction, moving slowly in 10 cm steps across 1.1m centerline on the testing grid. Left: Induction response; Right: Fluxgate response.....	28
Figure 5.15 - Timing interleaved time-sharing (solution 1)	28
Figure 5.16 - Timing interleaved time-sharing (solution 2)	29
Figure 6.1 – Model fit to vertical induction sensor data collected for Copper Sphere.	31
Figure 6.2 - Example frequency-domain complex response of a magnetic object. Peak quadrature response occurs at f_p	33
Figure 6.3 - Frequency of peak quadrature response from canonical UXO and fragments in AETC GEM-3 database. There is little correlation between object size and quadrature-peak frequency.	34
Figure 7.1 - Sensor noise in the induction mode	35
Figure 7.2 - Comparison of FIS and Geonics EM63 induction data for 37 mm shell in vertical orientation (collected at QFS Lab), 55-cm distance. Signals (B for FIS, dB/dt for EM63) are normalized at each time slice. Light contours are model fits.....	36
Figure 7.3 - As Fig. 7.2, with 37-mm shell in horizontal orientation.	36
Figure 7.4 - Dependence of the response vs. depth for FIS and EM63 for a vertically aligned 37 mm shell, at the time gate 336 us.	37
Figure 7.5 - Comparison of Commercial Fluxgate (CFG) and FIS in DC fluxgate mode for 37 mm shell vertically aligned over the grid (same coil and receiver as the induction mode).....	39

Figure 7.6 - Dependence of magnetic response vs. target distance for FIS and CFG for a vertically aligned 37 mm shell	40
Table 11 - Dipole Model Fits to Magnetic Grid Data.....	40
Figure 7.7 - Tri-Axial induction sensor response to 37 mm shell at depth of 55 cm aligned vertically, time gate = 300 μ s; channels x, y, and z respectively.	41
Figure 7.8 - Surface plots generated by TD3D analysis. Shown for a 37 mm shell at depth of 55 cm, aligned both vertically (top) and horizontally (bottom), time gate = 290 μ s.	42
Figure 7.9 - Transfer function and noise power spectrum of IS receiver for fixed series coil resistance. For the final system, $R_{coil} = 7$ kohms, which was optimized for the early time response. The solid curves are sensor gain, and the dashed curves show sensor noise referred to the input.....	44
Figure 8.1 - Three-axis dipole performance of aggregate discriminator on canonical and ordnance test articles at $z = 47$ cm.	47
Figure 8.2 - As Fig. 8.1, but for 2-axis dipole (axisymmetry assumption). 100% of cylinders are correctly classified (PD), whereas 38% of disks are incorrectly classified (PFA)....	47
Figure 8.3 - Z component, steel rod at azimuth 45 inclination 45. Data values are multiplied by 1000 for clarity. Upper panels show spatial pattern of data (color) and model fit (white contours). Bottom panels compare time decay of model (red line) vs data (blue circles).	48
Figure 8.4 - X-component of same rod.	49
Figure 8.5 - Y-component of same rod.	50
Figure 8.6 - As Figure 8.3, but for Z-component of circular steel disk at azimuth 45° inclination 45°.	51
Figure 8.7 - X-component of disk.....	52
Figure 8.8 - Y-component of disk.....	53
Figure 8.9 - Three-component fluxgate (DC magnetic) data (top row) and sphere model fit (bottom row) to a vertical steel rod.	58
Figure 8.10 - As Fig. 8.9, but for vertical steel pipe. Sphere fit is also to Z-component alone and results in 97% variance reduction in that component and 96% in all three components; cf. 96% variance reduction using all 3 components.	59
Figure 8.11 - As Fig. 8.9, but for horizontal steel rod. Fit is worse than in previous examples but still useful.	59
Figure 9.1 - Plot of IS background (during acquisition) and IS transmitter current (during Tx pulse) as a function of time (and scans).	61
Figure 9.2 - Ratio of IS background (during acquisition) to IS transmitter current (during Tx pulse) as a function of time (and scans).	61
Figure 9.3 - FIS mounted on plastic cart with plastic wheels for outdoor and mobile data collection. The new DAQ is used for data collection.....	62

Figure 9.4 - Sensor response to a vertical steel rod, at 47 cm below, for varying Tx pulse/acquisition windows. SNR goes roughly linearly with pulse width. The legend symbol “bg” stands for background response (dashed line) when there was no target.	63
Figure 9.5 - Background variation of IS for varying pulse train parameters, along with standard deviation of each experiment. The nominal configuration, 10/10/20, has the least variation.	64
Figure 9.6 - Top: Concept for true interleaved operation, FG acquisition during IS Tx pulse. Bottom: Serial time sharing employed by current system.	65
Figure 9.7 - Concept for running FIS in a detection/discrimination mode rather than continuous serial time sharing dual mode; maximizes IS data collection (and thus discrimination) while over suspect objects.	66
Figure 9.8 - Sensor response over bare ground (top) and over buried target (bottom) with the sensor “cold” (straight from the lab) and “hot” (after warming in the sun several hours).	67
Figure 9.9 - Comparison of sensor response to steel pipe buried and on test grid; no significant difference is seen.	68
Figure 9.10 - Z-axis IS background outdoors for dry, wet, and drying soil; no significant difference is seen.	68
Figure 9.11 - Top: 3-day background collection at 1 site. Bottom: Day 3/3 at both sites. Data was collected twice daily (10 am, 3pm) over 3 days. No significant variation is seen. ...	69
Figure 9.12 - Comparison of IS noise while moving (blue) with the system stationary, over asphalt in QFS back parking. Neglecting several anomalies, noise performance appears roughly similar.	70
Figure 9.13 - Sensor induction response to buried steel pipe, at 47 cm, as the sensor is moved continuously over the target, a 10/10/10 pulse train was used. Left: 0.5 s wait between runs. Right: 0 s wait between runs.	71

LIST OF ACRONYMS

A/D	Analog-to-Digital
EM	Electromagnetic
D/A	Digital-to-Analog
DAQ	Data Acquisition
FG	Fluxgate
FIS	Fluxgate-Induction Sensor
IS	Induction Sensor
Mag	Magnetic
OE	Ordnance and Explosives
OPM	Optically Pumped Magnetometer
PD	Probability of Detection
PFA	Probability of False Alarm
QFS	QUASAR Federal Systems
Rx	Receiver
ROC curve	Receiver Operating Characteristic curve
SERDP	Strategic Environmental Research and Development Program
SNR	Signal-to-Noise Ratio
Tx	Transmitter
TD3D	Time-Domain Three Dimensional model
TDEM	Time-Domain Electromagnetic
UXO	Unexploded Ordnance
VR	Variance Reduction

KEYWORDS

Dual-mode operation, Dual-mode magnetic sensor, Electromagnetic measurement, Fluxgate sensor, Fluxgate-induction sensor, High permeability core, Induction sensor, Induction coil, Magnetic measurement, Primary field, Time-domain Three dimensional model, Time-domain electromagnetic measurement, Unexploded ordnance, UXO detection, UXO discrimination

ACKNOWLEDGEMENT

We are grateful for support of this work from SERDP office (under project MM-1444, contract # W912HQ-05-C-0010, PI : Dr. Yongming Zhang, Co-PI: Dr. Robert E. Grimm).

ABSTRACT

In this SERDP project, QUASAR Federal Systems (QFS) developed and demonstrated an innovative dual-mode, fluxgate-induction sensor (FIS) that combines a fluxgate magnetometer and an electromagnetic (EM) induction sensor to sense DC magnetic (Mag) field and EM field respectively. The FIS is based on a 5" long, high-permeability magnetic core and a sensing coil that are shared by both EM and Mag modes. This integration makes the sensor very compact and removes the potential crosstalk problem of the core material of one sensor dominating the response of the other. A prototype receiver was developed and true serial, dual-mode operation demonstrated. The FIS has sensitivity of 1 nT for the fluxgate, and 0.2 pT/rHz at 1 kHz for the induction sensor. It compared favorably to the Geonics EM63 system in induction mode and to a commercial fluxgate in fluxgate mode. Triaxial dipole modeling confirms that three-component EM data are better for shape characterization than one (vertical) component

Assuming axisymmetry, inversions of three-component EM measurements of 22 cylindrical and disk-shaped targets yielded 100% correct classification of UXO-like objects (cylinders) and 38% misclassification of disks as cylinders. The discrimination performance of the FIS was comparable to that achieved using the EM61-3D at the Blossom Point test grid (PD = 91%, PFA = 32%). In fluxgate mode, the FIS yields very high quality fits of the data and relatively accurate target locations and depths. Triaxial dipole modeling of the Mag data confirmed the FIS's utility for detecting deeper targets using only the vertical component.

The dual-mode, 3-axis measurement results demonstrate the feasibility of using the FIS for UXO surveys, and show great potential for one-pass surveys and reduction of false alarm rates. The compact design of the sensor coil makes it feasible to integrate an array of 3-axis sensors into a next-generation receiver which could increase the receiver SNR and scanning speed.

1. PROJECT OBJECTIVE AND APPROACH

The object of this project is to develop and demonstrate a single compact receiver that operates both as a fluxgate magnetometer to sense DC magnetic field and as an electromagnetic induction sensor for AC magnetic field, via the innovative step of using the same high-permeability material for both sensors. In this project, we focused on the sensor development and demonstrated unexploded ordnance (UXO) detection and discrimination with a dual-mode sensor in the lab.

We initially divided the tasks into three years. A fourth year task was added to the project to characterize the sensor. In the first year we focused on proof of concept and scientific validation of the compact, dual-mode sensor based on the high-permeability cores. In the second year, we focused on the demonstration of single-axis UXO detection with the combined sensor in the lab. The third year focused on the 3-axis receiver design and testing. The fourth year was intended to optimize the 3-axis dual mode receiver and assess its discrimination capability in controlled environments with a number of projectiles and “canonical” objects. The overall technical approach is shown in Figure 1.1.

There were two technical milestones for the project. The Year 1 milestone was to demonstrate a compact induction sensor with an impulse response to a primary field of 0.1 mT to decay to ~100 pT within about 100 μ s. The Year 2 milestone was to demonstrate a dual-mode sensor with noise of 1 nT RMS in fluxgate (DC) mode and verify that the dual-mode sensor met performance requirements.

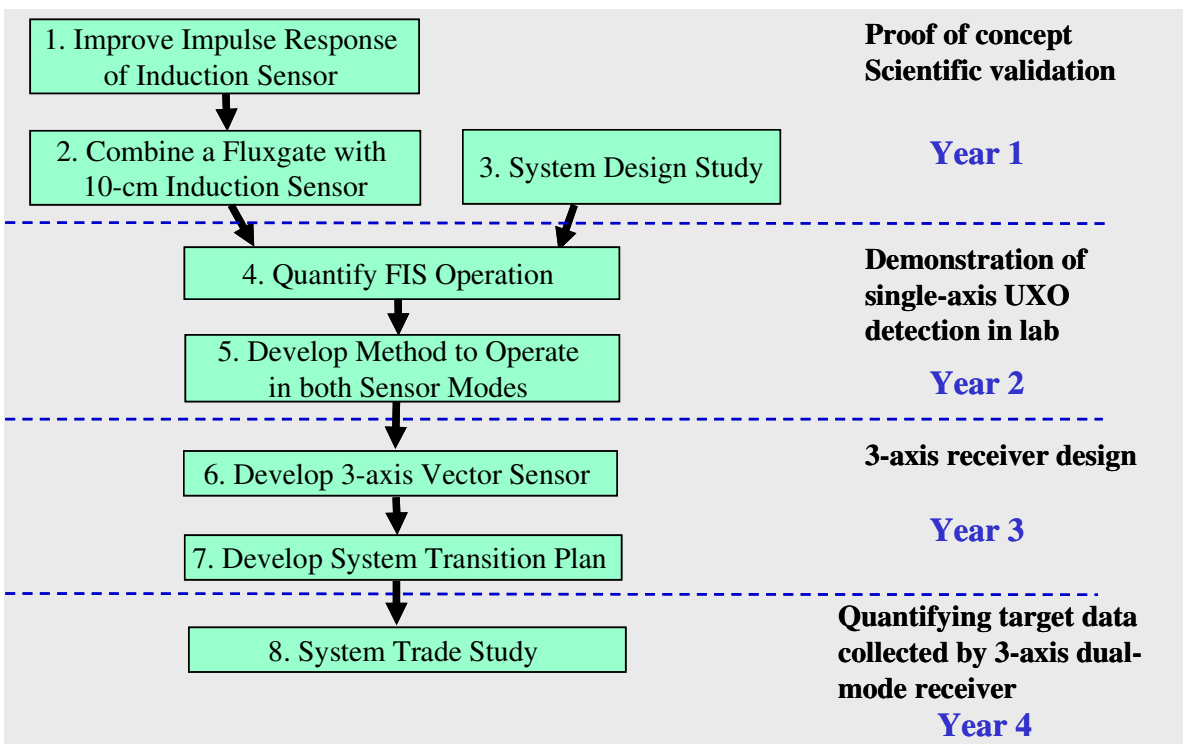


Figure 1.1 - Overall technical approach

2. BACKGROUND

2.1 The need for combined AC and DC magnetic sensors

Future advanced UXO detection and discrimination systems may require a combination of AC electromagnetic (EM) and DC magnetic (Mag) measurements and prefer 3-axis vector sensors to provide characterization of target shape and reduce false-alarm rate. The advantages of using a tri-axial system for UXO target classification have been demonstrated by *Grimm* (2003). The need for independent EM and Mag measurement increases system size, weight, and cost. Furthermore, a rigorously co-located measurement of the EM and Mag target response is difficult to achieve in practice. Present EM sensors used for UXO detection are predominantly air-core induction coils of order 0.5-m diameter (e.g., the EM61 coil has a size of 0.5 m x 1m, and EM63 coil has a size of 1m x 1m), a fact that makes them bulky and difficult to integrate into a compact 3-axis configuration. To measure the DC field, a second sensor, usually an optically pumped magnetometer (OPM), is required. An OPM is a total field sensor which does not contain vector information.

A fluxgate magnetometer has sufficient sensitivity for DC measurement of UXO. It is much cheaper than an OPM. However, using a separate induction sensor and fluxgate in close proximity is problematic because the signal detected will be dominated by the high permeability core and metal components of the other sensor, rather than by the target.

2.2 Innovation of this work

An integrated fluxgate-induction sensor using a common high-permeability core was invented by *Zhang et al*, (2008) under this project. A cross-sectional view of the sensor probe is shown in Figure 2.1. The magnetic field sensor constitutes a low-noise sensor and is able to operate in both a fluxgate mode to measure static (DC) magnetic field and an induction mode to measure an oscillating (AC) magnetic field. The resulting sensor provides for a compact magnetic sensor system capable of sensing magnetic fields from DC up to about 50 kHz. The use of two separate sensors results in crosstalk problems, whereby one sensor affects the response of the other. With the shared core structure, potential crosstalk problems between sensors are eliminated. The present sensor evinces an advantageous combination of bandwidth, sensitivity, size, and cost. Further, the present invention makes formation of a multi-axis receiver easier by minimizing the size of each combination DC and AC sensor channel.

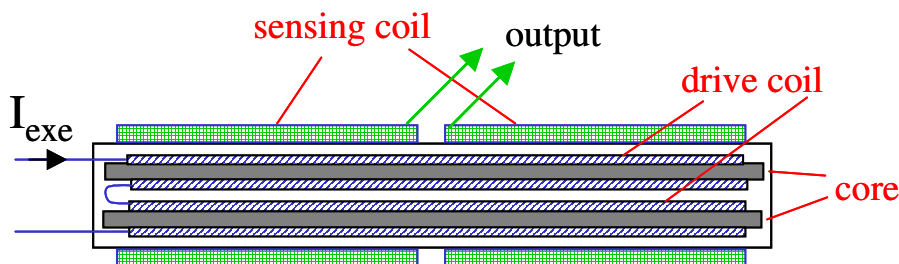


Figure 2.1 - Cross-sectional view of the dual-mode sensor probe. The same coils are used for both the induction sensor and the fluxgate magnetometer.

The shared core design means that the FIS cannot acquire fluxgate and induction sensor data simultaneously. Instead, the sensor can acquire data in either serial or interleaved operation. In serial operation, a fluxgate mode is operated for durations on the order of 0.1 s, with alternating induction modes. In interleaved operation, the sensor is operated in fluxgate mode during a transition period when the core is changing from a high permeability state to a low permeability state, or vice versa. In this case, the sensor operates in the induction mode when the core is in the high permeability state. A 3-axis version of the sensor was developed during this project and was applied to UXO detection with the capability of performing both EM and Mag measurements in serial operation.

2.3 TDEM measurement

Time-domain electromagnetic (TDEM) measurement is a common method for UXO detection and discrimination. In this type of measurement, a large primary magnetic pulse field is applied to the ground by a large transmitter (Tx) coil, and the primary field induces eddy currents in nearby metallic objects. The eddy current generates a secondary field that can be measured by a receiver (Rx) coil. The time decay of the response gives information about the size, shape, orientation, and material composition of the metal object.

TDEM data generally require very little data processing. The responses over numerous pulses are integrated or stacked in the receiver. It is convenient to time average or gate in the receiver in real-time, although that can be done in post-processing. The principal correction is generally for bias or drift, which is done by subtracting the instrument response that exists when no target is present. Also, statistical discrimination techniques based on model analysis such as the *Time-Domain Three Dimensional (TD3D) model* can separate UXO-like from scrap-like objects.

2.4 Challenges for using high-permeability induction sensor

Over the past few years, QUASAR has produced a class of high-sensitivity induction sensors with high permeability cores. The frequencies of the induction sensors range from a few Hz to about 30 MHz. Different cores were selected for different bands. With high-permeability cores the sensor is much more compact than an air-coil sensor. The challenge in using high permeability cores is that the primary pulse used in TDEM induces eddy currents in the sensor core. These eddy currents produce a signal in the core material that could obscure the early time target signal. It is perhaps this challenge that has prevented the use of high-permeability core based induction sensors by the UXO community for TDEM measurements.

2.5 Requirements

The sensor needs to detect ordnance ranging from 20-mm projectiles to 2000-lb bombs and provide data such that OE (Ordnance and Explosives) can be discriminated from scrap and other non-UXO. Theory by *Word et al* (2003) and measurement by *Grimm* (2003) indicate that the 20-mm projectile has a late-time relaxation constant of ~ 0.8 ms or equivalently a relaxation frequency of ~ 200 Hz. In order to capture the early-time decay at a fraction of the late-time constant, a bandwidth of ~ 2 kHz is required (~ 80 μ s). We adopt a high-frequency cutoff of 10 kHz to include a robust bandwidth margin for the sensor design. Time-domain amplitudes for the 20-mm projectile are ~ 1 nT for a transmitter moment comparable to the EM61, at an early time of about 80 μ s.

Based on the detection of 20-mm projectiles, we defined the system requirement as such: the *sensor response needs to decay from a peak field of 0.1 mT (approximately the field in the center of an EM61 coil) to 100 pT (a ratio of 120 dB) within about 100 μ s.*

2.6 Comparison with commercial and R&D systems

The standard UXO detection and discrimination systems for the UXO community are the EM61 and EM63, which have been commercially available for many years from Geonics Limited (www.geonics.com/html/metaldetectors.html). The 3-axis version, EM61-3D, was also made commercially available in 2007. A prototype system was tested by the UXO researchers in 2002, during a field test at Blossom Point by *Grimm (2003)*. To date there have been several R&D systems which employ some combination of: multiple receivers, multiple axes, and/or multiple detection modes. These R&D systems includes the Multi-Sensor Towed Array Detection System (MTADS) developed by the Naval Research Lab, the Man-Portable Simultaneous Magnetometer and EM System (MSEMS) developed by SAIC and CEHNC, the Berkeley UXO Discriminator (BUD) developed by the Lawrence Berkeley National Laboratory, and the MetalMapper developed by Geometrics. These systems greatly advanced the target discrimination capability, but no system is capable of doing one-pass Mag and EM survey (Table 1) except the MSEMS. Present EM sensors used for UXO detection are predominantly large air-core induction coils of order 0.5-m diameter (MTADS, and MSEMS); although small air-coils have also been utilized recently for the advanced R&D systems (BUD and MetalMapper). In these systems, optically pumped Cs magnetometers (OPM) are used to measure the DC magnetic field during the survey (MTADS, and MSEMS). Although the MSEMS collects Mag and EM data in a single pass, the OPM is more than 1 meter away from the center of the induction coil, and both sets of data are not co-located. According to the MM-0414 project report, it is challenging to co-locate an OPM with an EM sensor. Large magnetic fields from the primary pulse wipe out the Larmor signal and exceed the dynamic range of the OPM. An OPM is also relatively expensive, compared to a fluxgate.

A comparison of the FIS with other commercial systems and advanced R&D systems is listed in Table 1. The next generation UXO discriminator will collect co-located, dual-mode, 3-axis components in one-pass and use multiple receivers to increase throughput and reduce operating costs and time. The compact, dual-mode, fluxgate-induction sensor (FIS) developed under this work will expect to meet the requirements for next generation systems. Although only a single 3-axis sensor was developed for the prototype system, future systems can employ multiple 3-axis sensors in an array. The compact size of the sensor and the feasibility studies show FIS is suitable for integrating into an array for a future receiver system.

Table 1 - Comparison of FIS with commercial and other advanced R&D systems

System	Commercial product or SERDP/ESTCP R&D project #	Mag sensor	EM sensor	3-component for EM measurement	Receiver array	One-pass for Mag & EM survey
EM61/63	Commercial	no	large air coil	no	no	no
EM-61-3D	Commercial	no	3-axis large air coils	Yes	no	no
GEM-3	Commercial	no	large air coil	no	no	no
MTADS	UX-9812, UX-9526	Towed-array Cs magnetometer	three-coil receive array	no	Yes	no
MSEMS	MM-0414	Cs magnetometer	large air coil	no	no	OPM is 4 feet from EM61
BUD	MM-0437	no	small air-coil array	no	Yes	no
MetalMapper	MM-0603	no	small air-coil array	Yes	Yes	no
FIS	MM-1444	Yes	ferrite core coil	Yes	Yes*	Yes

* only one 3-axis dual-mode sensor for the R&D prototype, will use array to enhance performance in the future system

3. WORK SUMMARY

The project has been an extraordinary innovation and development experience for UXO instrumentation and good technical success was achieved on all tasks. Effective collaboration has been achieved between the QFS team and our consultants during the project, and the project objective was achieved. In this section, we summarize the results we achieved for each task. The goal for each task was met.

1) *Task 1 was aimed at improving the impulse response of the compact induction sensor.* By optimizing the coil design and selecting the fastest ferrite cores, we achieved a sensor response to a pulsed magnetic field, decaying from ~ 3 V to ~ 5 μ V within ~ 100 μ s. This corresponds to 116 dB of linear decay, shown in Figure 3.1. A field of 100 pT corresponds to a sensor response of 10 μ V for this coil. This coil is able to detect the EM response (about 1 nT) from a 20-mm projectile induced by a transmitter coil with a magnetic moment comparable to the EM-61 coil (field strength ~ 100 μ T). By subtracting the background digitally we achieved a dynamic range of 120 dB, which meets the milestone of Year 1. An anti-pulsing coil, which was implemented in the prototype receiver, reduces the primary field at the core volume by 10X to 20X. Based on these results we concluded (*Zhang, et al, 2005*) it is feasible to use high-permeability induction sensors for a time-domain UXO EM detection system.

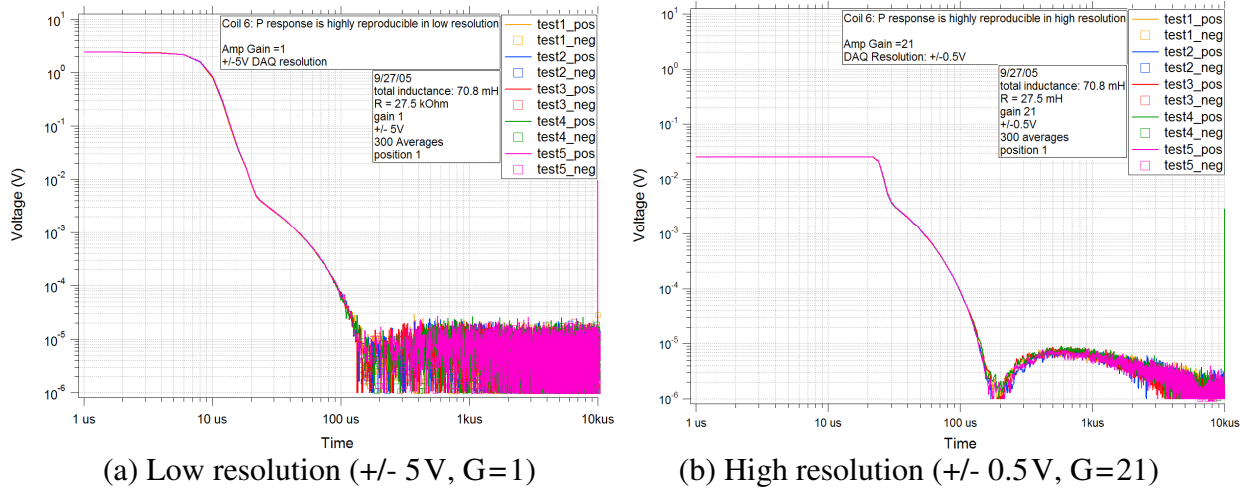


Figure 3.1 - Impulse response of a 4'' long coil (#6) with P cores ($L = 70.8$ mH, damping $R = 27.5$ kOhm each side). The field strength at the sensor location from the peak primary field is about $30 \mu\text{T}$. (a) DAQ card at low resolution; (b) DAQ card at a higher resolution (the output voltage has been divided by the amplifier gain)

2) Task 2's goal was to combine a fluxgate with an induction sensor. We designed a 10-cm long dual-mode sensor with two parallel cores in which the fluxgate (FG) shares the same magnetic core, sensing coil, and preamplifier as the induction sensor (IS). A proof-of-concept digital fluxgate was built based on Lab instruments (for clock generation, gain, and filtering) and NI DAQ (for data collection and demodulation). A block diagram of the Task 2 fluxgate design is shown below in Figure 3.2. We demonstrated that the fluxgate has a noise density of $100 \text{ pT}/\text{rtHz}$ at 1 Hz, and about 0.9 nT RMS noise in the band of DC to 30 Hz, with a detection sensitivity of $2.8 \text{ mV}/\text{nT}$. The sensor noise performance met the project requirements (Year 2 milestone).

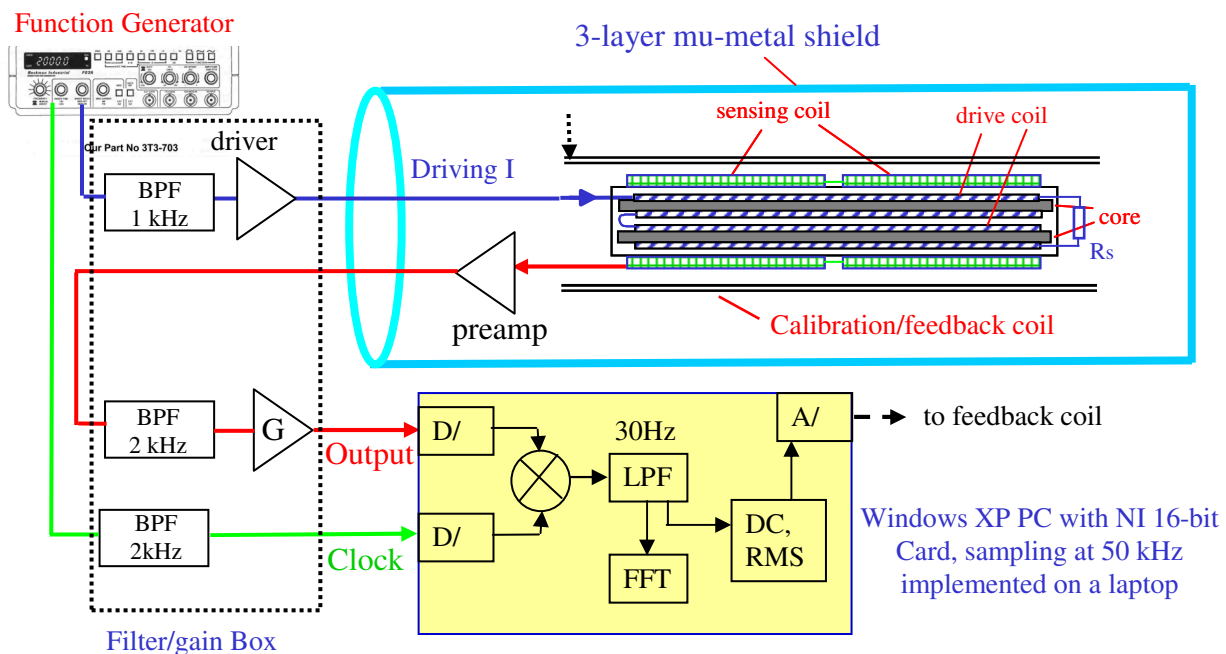


Figure 3.2 - Block diagram of the Year 2, Task 2 fluxgate magnetometer.

3) *Task 3 was focused on developing requirements for the sensor bandwidth and sensitivity using existing databases, models, and limited test data for the new fluxgate-induction sensor.* For specified types of ordnance, the bandwidths for induction should be 10 Hz – 100 kHz; however, we decided to limit our prototype receiver to a bandwidth of 100 Hz to 10 kHz, which is enough for all targets we planned to test. Target-unique parameters were derived from initial test data with the prototype sensor and a Tx coil with moment of 3.5 A-m^2 . Overall SNRs are good. When a large transmitter moment is ultimately implemented, 20-mm projectiles should be detectable with a signal-to-noise ratio (SNR) of > 10 to depths of 0.42 m. The IS response was compared to time-domain model fits for various targets at various depths; Figure 3.3. The model fits for smaller targets were poorer than for 37-mm projectile due to systematic errors in data.

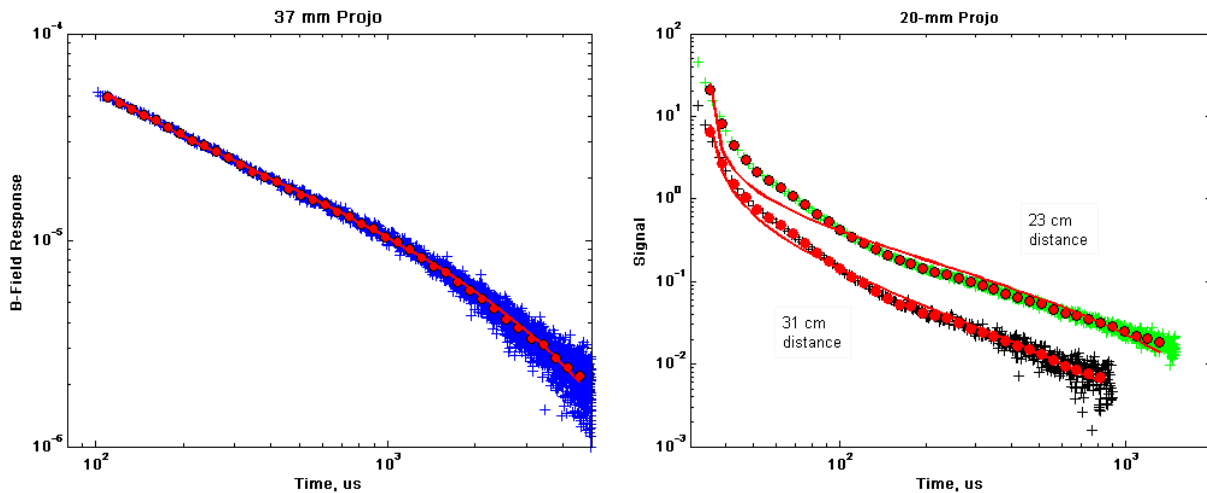


Figure 3.3 - FIS-prototype magnetic-field induction response collected in Year 2 for Left) a 37-mm vertical projectile (blue crosses) at 31 cm below Tx, and time-domain model fit (red line), and bin-averaged data (red dots). Right) 20-mm projectile at 23-cm and 31-cm. Black and green crosses are measured data. The magnetic moment of the Tx coil is 3.5 A-m^2 for the data collected.

4) *Task 4 was aimed at quantifying the fluxgate-induction sensor's operation.* We built a large transmit coil and a driver that generate a magnetic moment of 160 A-m^2 and have a fast recovery time of less than $150 \mu\text{s}$. We integrated all electronics for the fluxgate operation onto a circuit board. A photograph of the Task 4 system is shown below in Figure 3.4. Noise performance similar to what was achieved in Task 2 was also achieved in this task. We improved the induction sensor amplifier by adding blanking circuitry. With the modification, the sensor has better detection of low frequency components. The induction sensor can clearly detect 37-mm shells at 55 cm away with expected response in the time-domain. Target data was collected using the FIS and commercially available sensors (EM63 and a fluxgate magnetometer with 1 nTrms sensitivity). The data sets were modeled to recover the shape and orientation of the target (37mm shell). The performance and discrimination capabilities of the FIS were found to be roughly equivalent to the commercial systems. See Section 7 for details.

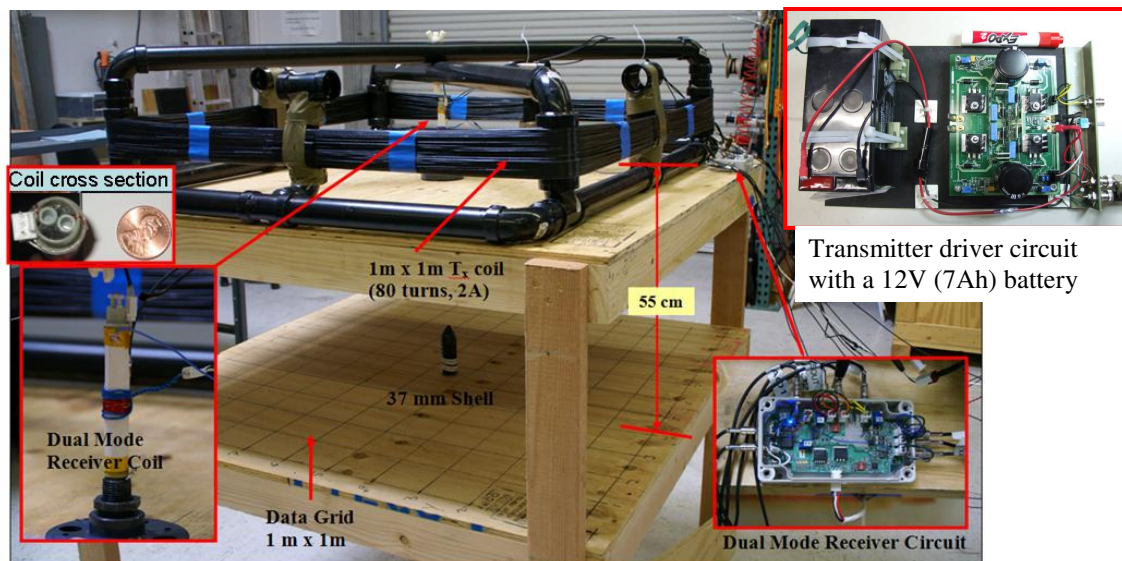


Figure 3.4 - Year 2 testing setup to quantify dual-mode sensor operation. The driver generates 2 Amps bi-polar currents in the Tx coil ($200 \mu\text{T}$ field in the coil center), with a decay time constant of $20 \mu\text{s}$, and a total turn-off time of $100 \mu\text{s}$ (moment of $80 \text{ A}\cdot\text{m}^2$) and $150 \mu\text{s}$ (for $160 \text{ A}\cdot\text{m}^2$).

5) *Task 5's goal was to develop a fully integrated dual-mode sensor.* A dual-mode Rx coil had been developed under Task 2, capable of operating in either fluxgate or induction sensor mode. This dual mode coil required a separate set of receiver and control circuitry and DAQ for each mode. Under this task, we developed the rest of the dual mode sensor, integrating both receivers into one circuit. A LabVIEW program was written to allow both sensors to be operated in succession, from a single DAQ. We then optimized individual parameters for each sensor, balancing for dual mode operation. The result was a fully integrated, single-axis, dual-mode fluxgate/induction sensor. SNR for a standard target (37 mm shell) was verified to be on par with that of the individual sensors. A serial time sharing scheme was tested and optimized for 20 stacked IS scans ($40 \text{ ms} \times 20 = 800 \text{ ms}$) followed by 0.2 s of FG operation.

6) *Task 6 was to build a 3-axis dual mode sensor.* A 3-axis coil assembly and a 3-axis receiver were designed, built, and tested. The coils and receiver were tuned such that their sensitivity and noise performance was equivalent to the original single axis sensor. The induction sensor had a noise floor less than 0.2 pT/rHz at 1 kHz , with the cross coupling less than 1% between axes. The fluxgate sensor had a noise floor of $2\text{-}3 \text{ nTrms}$ which is higher than the goal of 1 nT (achieved for the signal axis). The impulse response of the 3-axis sensor to the primary field was measured at different positions inside the transmitter loop. It was found that the receiver coil can be tuned to operate anywhere within Tx coil halo. Target data were collected and processed with the TD3D modeling. The vertical, or z, axis of the three-axis assembly performed equivalently to the original single axis during the data collection. The TD3D target shape and position recovery, with the three-axis receiver, was found to be an improvement over the original single axis.

7) *Task 7's goal was to develop a transition plan which would inform the design of the next phase system.* QFS contacted numerous companies and individuals in the UXO business; evaluating potential collaborators/customers and considering the design of the FIS system. QFS

also began designing the basic components of an improved system. There were several options to adapt existing transmitter coils and drivers from other R&D systems or commercial products, see Table 2. After comparing the cost, availability, and interfaces with the QFS sensor, we decided in 2008 to develop a higher moment transmitter coil and driver (Tx coil #2, the last option on Table 1) in house. The new transmitter was built and used in Year 4. A new NI DAQ, suitable for outdoor data collection, was also specified.

Table 2 - Options for obtaining an existing transmitter that has a fast turnoff or/and larger moment than our existing transmitter (coil #1B)

Transmitter	Moment [A-m ²]	Turn-off time [us]	Coil size	Note	Recommendation
QFS Tx coil #1B	160	180	1 m x 1m	80 turns, 2A, AWG 16, 12 V	Need to improve for better S/N
EM63	512	180	1 m x 1m	Hard to interface with our bucking coil	Not a solution
G&G Sciences	100	100	1 m x 1m	Possible to modify software to control the transmitter & the bucking coil	<ul style="list-style-type: none"> Limited available for evaluation Backup Tx solution for next term system
NT-20 Nano TEM Driver + QFS existing coil			1 m x 1m	Has a rapid current turnoff, supply up to 20 A into larger loops in slow turnoff mode	<ul style="list-style-type: none"> Suggested by Dr. Skip Snyder Only available for Zonge's internal R&D, or on-site evaluation
QFS Tx coil #2	420	200	1 m x 1m	96 turns, 4.5 A, AWG 14, 24 V, pull more power	Best Tx solution for near term system (built in Year 4)

8) Task 8 was an add-on task to the project. *The goal was to quantify the 3-axis sensor performance in a controlled environment.*

- QFS optimized the system performance by building a large moment Tx coil (coil #2, see Figure 3.5), minimizing the DC drift of the fluxgate, and eliminating a cross-coupling issue in the receiver design.
- QFS quantified the system performance on an indoor test grid, with EM and Magnetic data collected and analyzed for canonical shapes as well as typical UXO targets. The discrimination performance of the FIS, in induction mode, was comparable to that achieved by *Grimm* (2003) using the EM-61-3D at the Blossom Point test grid (PD = 91%, PFA = 32% for 3-axis models). In fluxgate mode the FIS achieved high quality fits of the data and yielded relatively accurate locations and depths for targets. This suggests that simple magnetization models of vertical, or total-field data, are capturing the vast majority of the data structure.
- QFS also addressed some practical issues for future field deployment: a) developed an outdoor DAQ system based on a laptop platform; b) used a current monitor on the transmitter coil to compensate IS background drift due to the power droop in the Tx batteries; c) the prototype system can achieve a spatial resolution of 0.125 m with 0.5 m/s moving speed, but can be reduced further with a multiple-sensor configuration or a reduced Tx pulse width; d) testing data shows the sun heating does not change the receiver response; e) No obvious variation is seen for the Z-axis response between wet and dry ground, and as a function of time and location

- The prototype system was mounted on a plastic cart with a non-metallic wheel for outdoor and mobile data collection. SNR for the receiver was improved when the system was moved from the lab to outdoors.

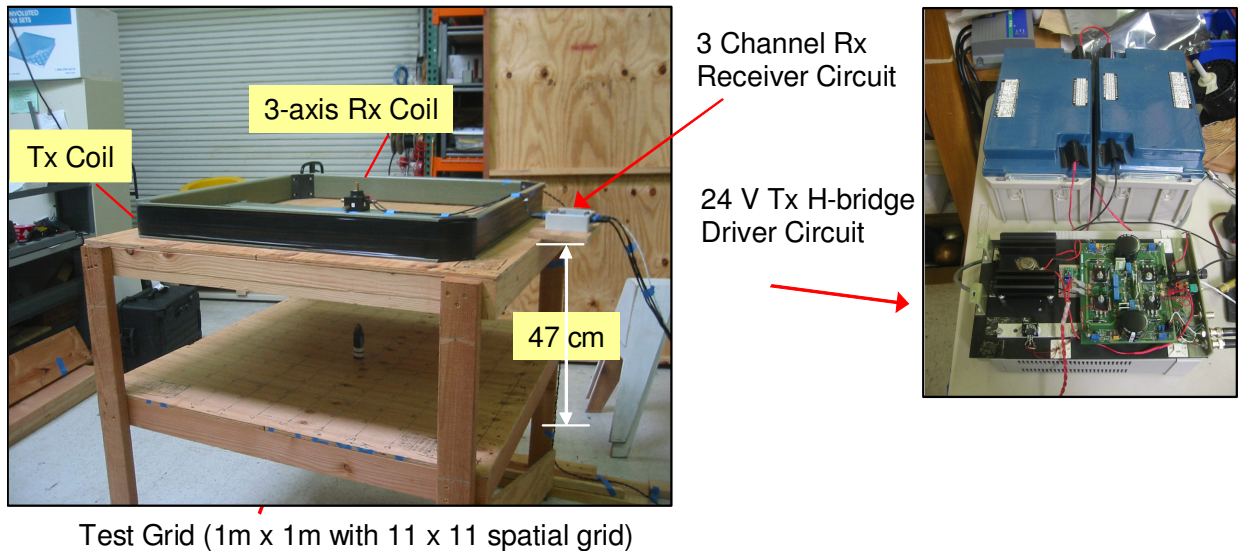


Figure 3.5 - Year 4 testing setup (research prototype system) for evaluating the fluxgate-induction sensor. The Rx coil sits in the middle of the Tx coil, 47 cm above a test grid. The transmit coil and a driver generate a magnetic moment of 420 A-m^2 and have a recovery time of about $220 \mu\text{s}$.

4. MATERIALS AND METHODS - SENSOR DEVELOPMENT

During the course of sensor development, several test setups were developed for evaluating the sensor performance. These setups were based on the standard time-domain UXO EM detection architecture, shown in Figure 4.1. All key components for the setups were custom made. The system includes the following key components:

- Transmitter driver circuit and battery power supply
- Transmitter coil
- Receiver coil (and core)
- Receiver amplifier
- DAQ card (with multiple A/D inputs, D/A outputs, and Digital lines)
- LabVIEW program
- Testing bed

Modifications were made to the transmitter driver, receiver coil, and amplifier, and the LabVIEW program to address the focus during different stage of the program. The Year 1 testing setup was mainly built for the core material evaluation and a small transmit coil with a magnetic moment of 3.3 A-m^2 was designed. The setup is shown in Figure 4.2.

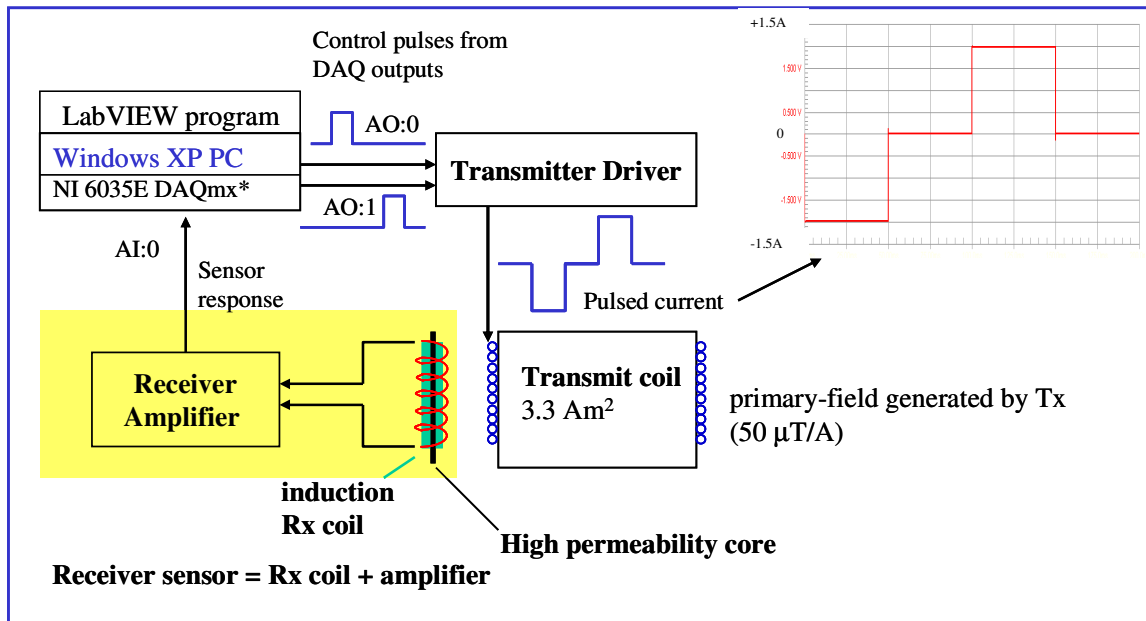


Figure 4.1 - System architecture for measuring the sensor impulse response. The same architecture was used for later systems except coil size and magnetic moment were greatly increased for characterizing the sensor performance in target detection.

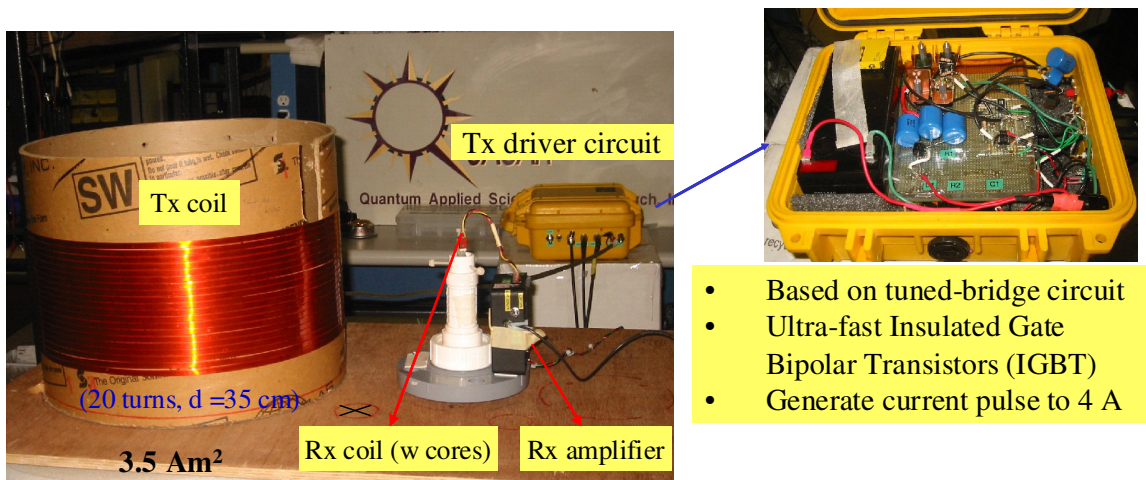


Figure 4.2 - Year 1 testing setup for measuring sensor impulse response, especially the core material evaluation. The Tx coil is constructed with 20 turns of copper strip and has a diameter of 35 cm. The setup generates a step field with a decay time of less than 30 µs, from about 100 µT to less than 50 pT.

In Year 2, large coils (#1A: 0.5m x 1m, 80 Am²; #1B: 1m x 1m, 160 Am²) were designed to quantify sensor operation, as shown in Fig. 3.4 above. A testing table with an 11 x 11 (10 cm

steps) spatial grid was built. The Tx driver was redesigned to drive the large coil, based on the H-bridge topology.

In Year 3, in order to match Tx coil with the EM63 system, we increased the moment to $420 \text{ A}\cdot\text{m}^2$ by increasing the driver current and coil turns. We also made a rigid structure to support the Tx coil, as shown in Fig. 3.5 above. This setup was used for the 3-axis, dual-mode sensor evaluation during Years 3 and 4. We called it the research prototype system for the FIS receiver. Since it is the final design for the FIS receiver system under this program and will be the base for developing a field deployable system, we will discuss key components of the prototype system in detail in the next section.

5. MATERIALS AND METHODS - RESEARCH PROTOTYPE

In this section we give a system overview of a prototype receiver system that was developed to demonstrate the capability of the 3-axis, dual-mode sensor.

5.1 Receiver system overview

A system block diagram for the 3-axis FIS receiver and other system components is shown in Figure 5.1. The wiring between blocks is also shown in the diagram. The receiver includes three components: 1) a receiver coil (R_x coil), 2) a receiver electronics box, and 3) data acquisition and control hardware with custom software. All the receiver components are shared for both induction and fluxgate operations. Other system components are a transmitter coil (T_x coil), a transmitter driver (T_x driver), and a battery power supply. The T_x coil and driver are only used during the EM measurement.

For the prototype system, a National Instruments data acquisition (DAQ) card is plugged into a laptop PC running on Windows. A LabVIEW program was developed to control the operation mode, data collection, and data processing (such as parameter setting, stacking, background subtraction, etc). The operation mode is controlled by the digital line D_0 from a DAQ card, while the switching time is controlled by the line D_1 (see more discussion in the section Dual-Mode Operation). According to comparison measurements we carried out, the system (in EM mode) has similar performance to the EM63 system in detecting a 37 mm shell at 55 cm depth, and similar performance to a commercial fluxgate sensor (with 1 nTrms sensitivity) in the Mag measurements. The dual-mode R_x coil and electronics box are very compact and are suitable for the sensor array implementation, as shown in Figure 5.2.

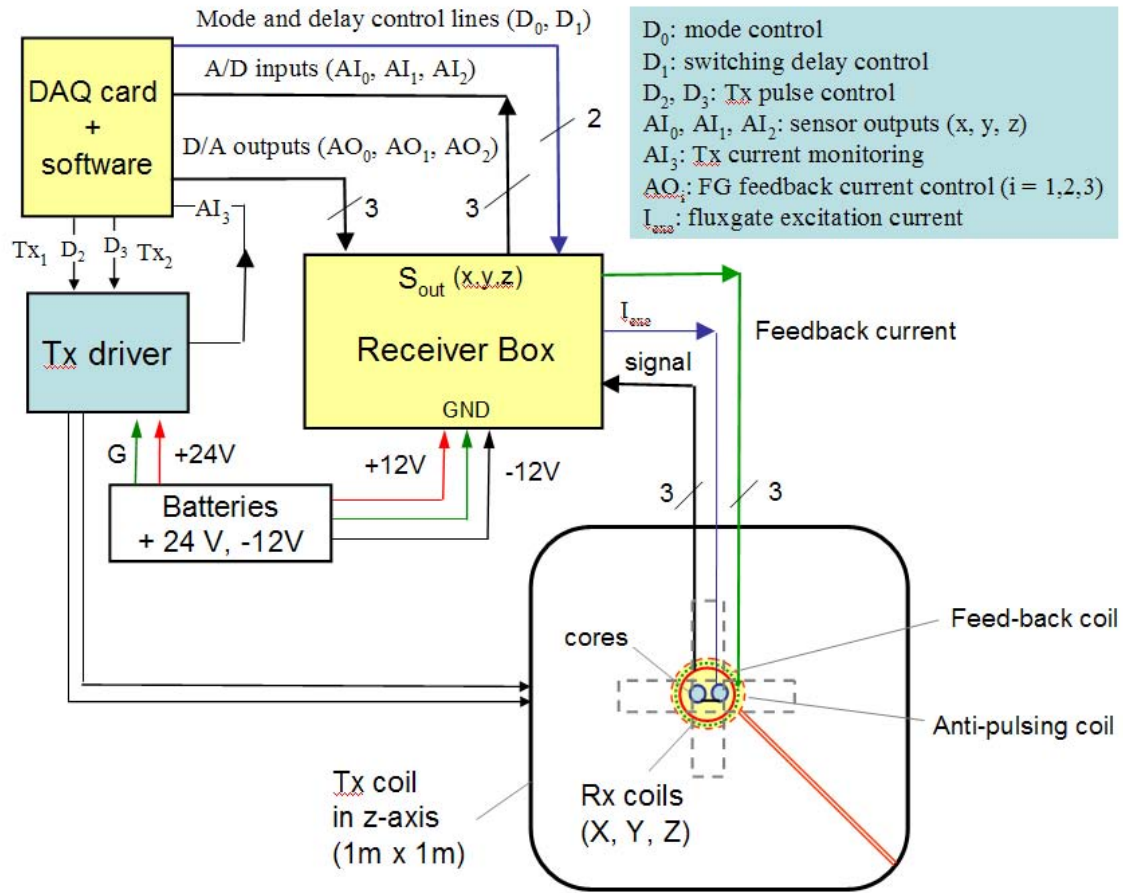


Figure 5.1 - System block diagram for FIS receiver.

5.2 Dual-mode sensor

The key components for the dual-mode sensor are a dual-mode sensing probe and a receiver circuit board. We will describe the details of these two components below.

5.2.1 Dual-mode sensing probe

In order to use an integrated coil for both Mag and EM measurements, we developed a sensing probe that includes several coils for each axis: a sensing coil for measuring the EM or magnetic field, a bucking coil for reducing the primary field on the cores (IS mode); excitation coils for generating a driving field on the cores, and a feedback coil for canceling the Earth's field (FG mode). To minimize the induced voltage on the sensing coil from the transmitted pulse (primary field), a thin copper sheet wrapped around the sensing coil as an electrostatic shield. The shield is connected to the ground of the receiver system. A photograph and basic design of the dual-mode receiver probe are shown in Fig. 5.2.

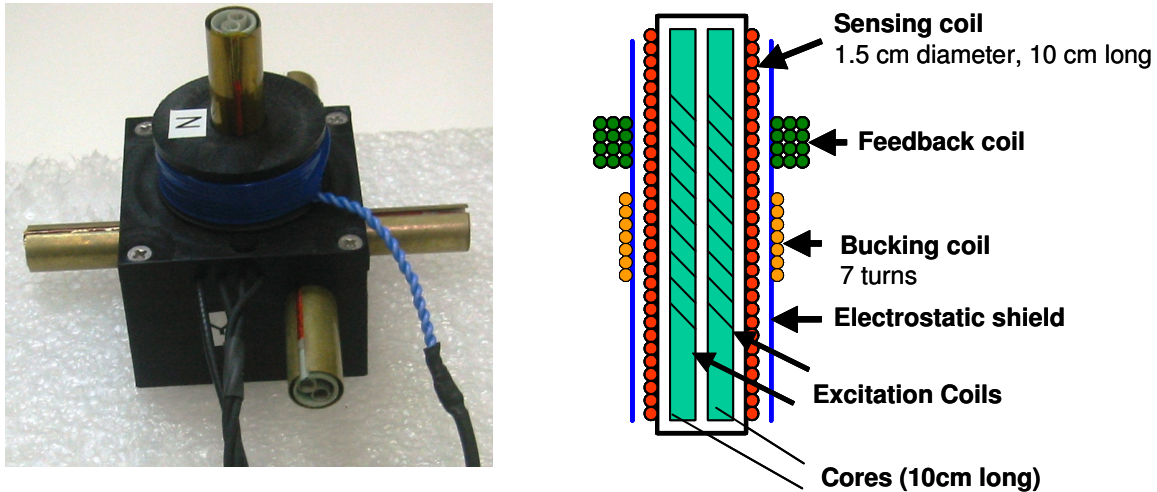


Figure 5.2 - Dual mode receiver probe. Left: a photo of the 3-axis probe; Right: details of the probe. Two ferrite core excitation coils sit inside one larger diameter induction coil. Bucking coil is implemented one the Z-axis coil (blue wire).

Using a high-permeability ferrite core can greatly reduce the sensing coil size of the receiver (R_x), thus enabling the arrangement of a sensor array inside a transmitter (T_x) coil. A fast response, low-loss, high-permeability core was selected for the R_x coil. The primary pulse field induces eddy currents in the sensor core, which could obscure the early time target signal. This challenge was overcome with *proper induction coil design, a bucking coil, fast cores, and digital subtraction*. In the following we describe the study on the coil optimization and core selection, as well as the digital subtraction and anti-pulsing.

A. Coil optimization for induction response

In order to design a coil that gives adequate response amplitude and has a fast decay, several compact induction coils were designed and used for core evaluation and for coil optimization, Figure 5.3. Five coils were used, where coil 0 was an old coil prepared for a previous project, and coils 1-4 were prepared during this project. To provide better common mode rejection, a split winding method was used for all these coils. Without external shunt resistors these ferrite core coils usually show ringing response to pulsed magnetic fields, due to their high-Q. The coil ringing was measured at the outputs with a high impedance probe connected to an oscilloscope. By measuring the ringing period, we extracted the properties of the coils.

The coil was designed so that high-permeability cores could be fitted inside the coil form. Coil 1 is similar to coil-0; both are 3" long. But Coil 1 has a double layer of Kapton[®] tape between the winding layers to reduce parasitic capacitance. Coil-2 (4") is longer than Coil-1 (3"), so there are more winding turns per layer. Coils 3 and 4 have the same number of winding turns, but Coil 3 has a larger form than Coil 4, so Coil 3 has a large inductance and effective area to capture the field. The properties of these coils are listed in Table 3.



Figure 5.3 - Photo of coils built under this task for evaluation

Table 3 - Properties of compact coils

Coil #	Length	Winding Layers	Tape between Layers	Core used	Inductance L_{coil} (mH)	Resonance Frequency f_0 (kHz)	R_p (kOhm)	Coil Capacitance C_{coil} (pF)	Decay Time's Constant (μs)	Sensitivity (V) (for 10 V pulse)
0	3"	6	None	3 Rods	154.6	38.4	18.64	111.23	8.29	1.4
1	3"	6	2	3 Rods	141.0	67	29.66	40.06	4.75	1.82
2	4"	1	N/A	3 Rods	8.1	200	5.09	78.26	1.59	1
3	6"	1	N/A	6 Rods	22.8	200	14.32	27.80	1.59	2.8
4	6"	1	N/A	6 Rods	18.5	200	11.62	34.26	1.59	2.34

Note

1. coil performance was evaluated with ferrite core rod (78 Material from Fair-Rite Products Corp), each is 1" long, 3 mm in diameter
2. The coil resonance frequency was measured by a scope from the resonances of the coil, measured with a high-impedance probe
3. Coil critical damping resistance $R_p = 2 \pi f_0 L/2$, where f_0 is the coil resonance frequency
4. The coil parasitic capacitance $C_{\text{coil}} = 1/[L_{\text{coil}} (\pi f_0)^2]$
5. The coil decay time constant $\tau = L/R$

A small capacitance gives a high frequency resonance and produces fast decay of an induction coil. We found the parasitic capacitance of the coil C_{coil} can be reduced by using Kapton[®] tape (1 mil thickness) between winding layers. The tape effectively separates two winding layers, and reduces the capacitance between these two layers. As shown in Table 3 for a 3" long coil, coil #1 is 35% faster than Coil #0. Also, Figure 5.4 shows that for a 6" long coil, double tape between winding layers reduces the ringing period by 33, reducing the coil impulse response time if the coil is critically damped. A larger inductance for the nanocrystalline bar in Table 4 is due to the fact that it has a larger cross-sectional area than the ferrite rod, although both of them have the same length of 6".

Table 4 - Improving the 3” coil with Kapton tape between winding layers

	coil-1 (3", 6 layer)			coil-0 (3", 6 layer)	
	with double tapes between layers			no tapes between layers	
Core material	L	ringing period		L	ringing period
Ferrite 78 rod	141 mH	17 μ s		154 mH	26 μ s
Nanocrystalline bar 1	183 mH	19 μ s		200 mH	30 μ s
Nanocrystalline bar 2	188 mH	19 μ s		204 mH	30 μ s

Coil: 6" long, 2 winding layers	
Tape between layers	Ringling period
no	22.5 μ s
1 layer	19 μ s
2 layer	15 μ s

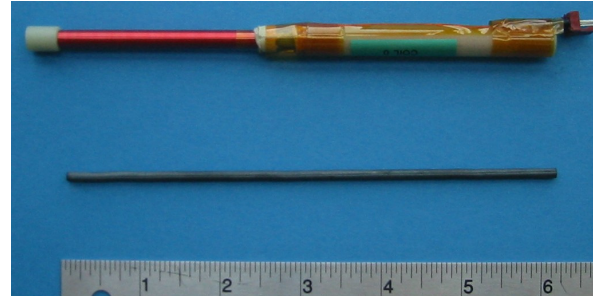
**Figure 5.4 - Improving the 6” coil with Kapton tape between winding layers**

Table 3 shows that the coil capacitance exists even for the single layer winding. It is from the coupling capacitance between winding turns on the same layer. One approach to reduce this coupling capacitance is to use “multi-section winding” for the coil. We prepared a coil form machined on G-10 tube for four-section winding on each side, Figure 5.5, and wound a coil (Coil #6) on this form. The coil has less parasitic capacitance between winding turns.

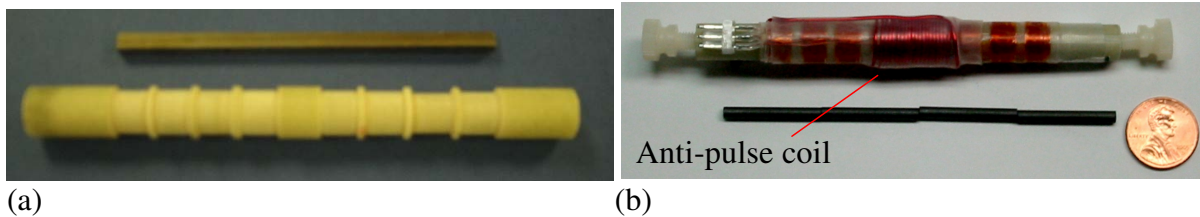


Figure 5.5 - (a) Coil former for multi-section winding. A 3” long nanocrystalline bar is also shown (b) Coil #6 made of multi-section winding (four 1” long P-rods at background). An anti-pulsing coil was wound for the anti-pulsing study

Table 5 shows a comparison of two coils of same length, one with double Kapton tape between winding layers (coil #1), and one with a multi-section winding method (coil #6). For a given core material, the total critical damping resistance R_c for the coil ($= \omega_c L/2$, twice the value for the damping resistance each side) is about 2x higher for the coil #6 than the coil #1. This means the decay time constant $\tau = L/R_c = 1/\pi f_c$, where f_c is the ringing frequency. *Multi-section winding increases the ringing frequency, and therefore reduces the decay time; a key step in improving the sensor impulse response.*

Table 5 - Improving the coil with multi-section winding

Coil #	Core (number of cores)	Total Inductance (mH)	Ringing		Damping resistance (kOhm) each side
			Period (μ s)	Frequency (kHz)	
1	nanocrystalline bar	193.1	29.6	33.8	20.5
	P (3)	109.7	21.8	45.9	15.8
	78 (3)	151.1	26.2	38.2	18.1
6	P (4)	71.3	8.1	123	27.5
	78 (4)	112.2	10.5	95.2	33.5

coil 1: 3" long, 6 layer winding, 2 Kapton tapes between layers

coil 6: 4" long, 6 layer winding, multi-section winding

B. High-permeability core evaluation

In order to use a high-permeability core for the dual-mode coil, we evaluated the available high permeability cores recommended for high frequency operation. These cores include three types of rods (M, R, P) from National Magnetics Group, the nanocrystalline (MMN-769) bars from Magnetic Metals, and the 78 rod from Fair-Rite. The nanocrystalline bars have a composition of 82% iron, with the remainder composed of silicon, niobium, boron, copper, carbon, nickel and molybdenum.

Properties for different core materials are listed in Table 6, where the loss factor ($\tan\delta/\mu_i$) is the core-material loss tangent ($\tan\delta$) divided by the core-material initial permeability (μ_i). Coil #1 and Coil #2 were used to study the ringing frequency of the coil. The results are shown in Table 7. As we can see from the results, although the initial permeability of the core material varies from 125 to 4000, the inductance only changes about 3x. This is due to the fact that the effective permeability μ_a depends on the intrinsic permeability of the core material, μ_r , and on the geometrical shape of the core. For rod geometry we used ($L/d = 25$); the latter tends to dominate the effective permeability μ_a .

Table 6 - Properties of different core materials

Core properties							
Coil	Core name	Material Description	core cross section	Vendor	initial perm-eability	Loss factor 10^{-6} @ Freq.	Resistivity Ω cm
1 (3")	M rod	NiZn	d = 3.14 mm	National Magnetics Group	125	< 40 [2.5 MHz]	10 M
	R rod	MnZn			450	< 100 [2.5MHz]	100 M
	P rod	MnZn			600	< 25 [0.2 MHz]	100
	78 rod	MnZn ferrite	d = 2.94 mm	Fair-Rite Products	2300	4.5 [0.1 MHz]	200
	old nanocrystalline bar	iron	3mm x	Magnetic Metals	4000	not available	120 μ
	new nanocrystalline bar	composition	3.15mm		4000	not available	120 μ

Table 7 - Coil properties with different cores

Core properties		coil properties with cores			
Coil	Core name	Coil L (mH)	Coil R (Ohm)	Ring. Freq. (kHz)	Ring. amplitude (w/ 10 V input) (mV)
#1 (3")	M rod	68.7	106.6	58.1	136
	R rod	106.6		46.7	144
	P rod	109.7		45.9	144
	78 rod	151.1		38.2	148
	old nanocrystalline bar	187.7		34.2	167
	new nanocrystalline bar	193.1		33.8	160
#2 (4")	M rod	3.42	18.1	588.2	376
	R rod	5.02		526.3	420
	P rod	5.15		490.2	404
	78 rod	8.13		371.7	444

To evaluate the impulse response, we measured the sensor response directly. The coil responses were measured at a location 15 cm away from the edge of the Tx coil (see Fig. 4.2). The Tx coil was sitting on a table of 80 cm in height, to avoid influence from metal objects under the floor. For each type of core material, we tuned the damping resistors to achieve critical damping for the coil.

The impulse response of Coil #1 (3" long coil with 6 layer winding) with core material P-rods, 78-rods, and a nanocrystalline bar is shown in Figure 5.6. The data were collected with a 200 kS/s DAQ system. Comparing the responses for each core material, we conclude that core material P has the fastest decay, and the 78-rod is faster than nanocrystalline bar. A small washer target (two stacked washers, inner/outer diameter = 1.8/4.5cm, thickness = 3mm each) was placed between the Tx coil and the Rx coil at the X mark position to validate the sensor performance. A clear target signal was observed when the coil had the P rod, but was hard to see when the coil had the nanocrystalline bar and the 78 rod. We found that the early time response collected with the 1.2 MS/s DAQ card is much more reproducible than the data collected with 200 kS/s DAQ. The response for Coil-6 with P-cores measured with the 1.2 MS/s DAQ system achieved 120 dB decay within 100 μ s, as shown in Fig. 3.1. We also evaluated the response from core materials M and R. These showed a slower response than material P. The hump at 400 μ s in Fig. 5.6 (c) could be from the response of iron re-bars in the floor.

We also used Coil #2 and Coil #6 to evaluate core materials P and 78. Similar to Coil #1, the coil with P cores has a faster response than that with the 78 cores. A clear target signal from the washers was observed. Based on these measurements, we conclude material P is better for building the induction sensor than the ferrite rod 78 and nanocrystalline bars. *P cores were selected for the receiver.*

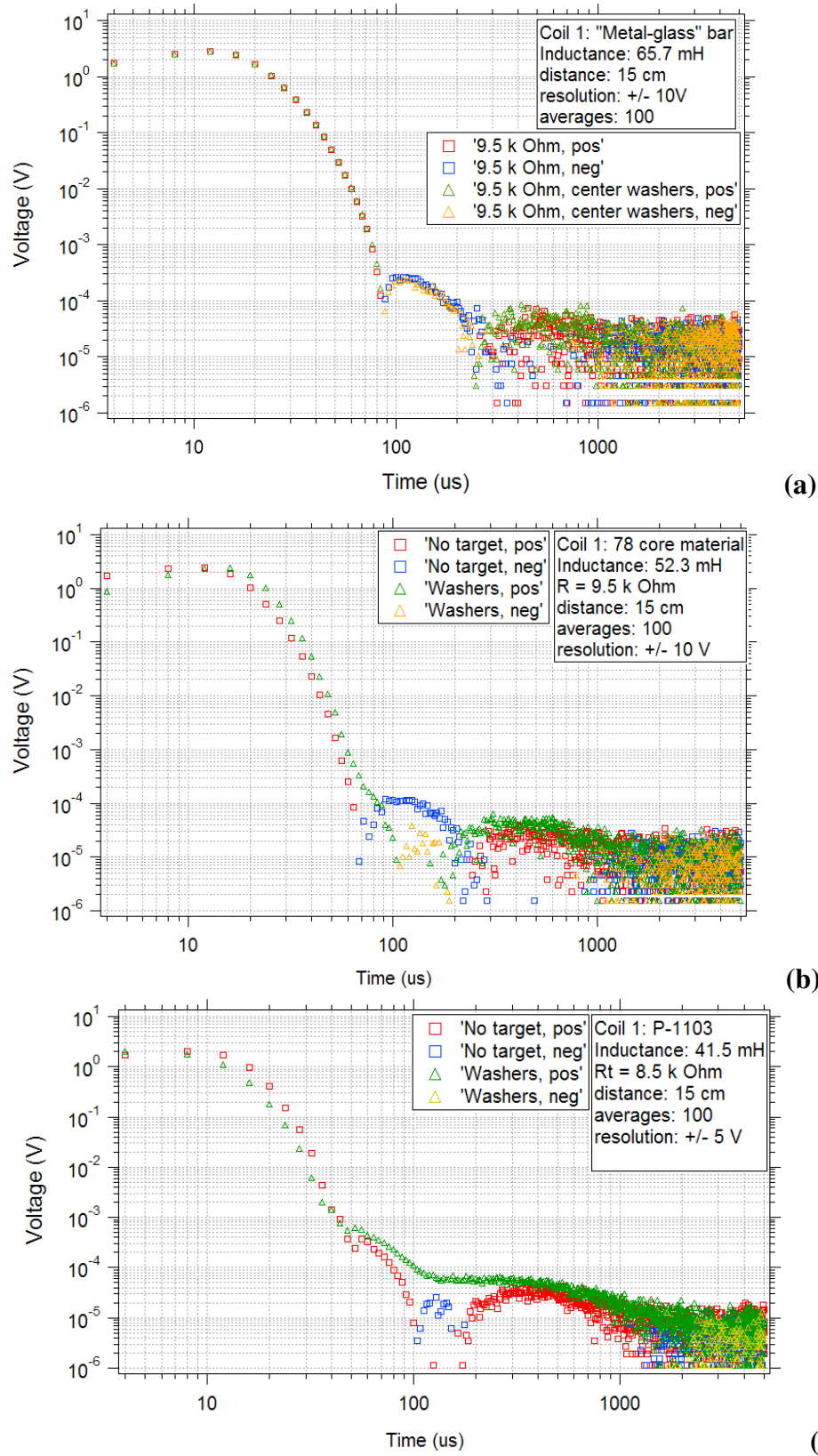
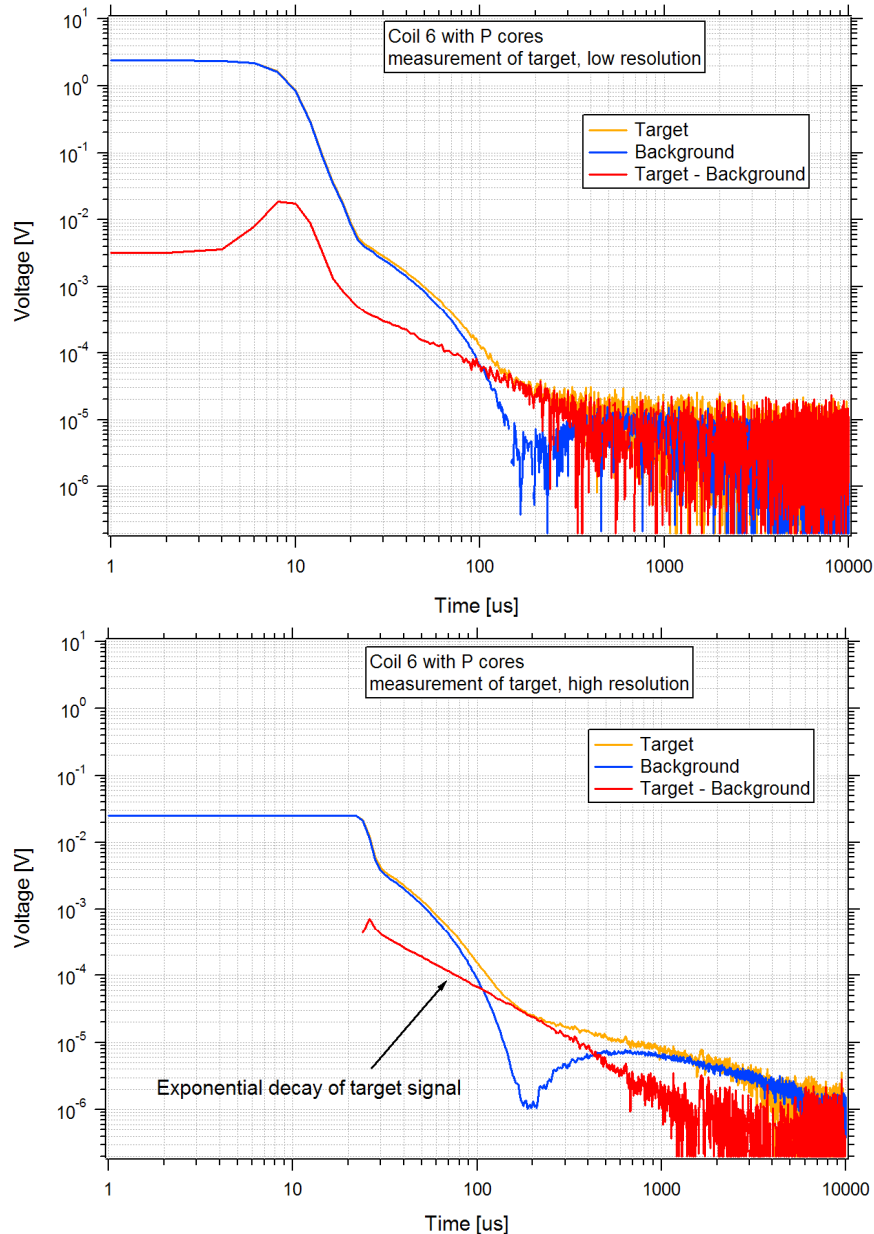


Figure 5.6 - Impulse response of coil #1 with different core materials (a) Nanocrystalline bar; (b) Ferrite 78 rods; (c) P-1103 rods

The sensor response for coil #6, for five different runs, with and without the wash target is shown in Figure 5.7. We used two separate measurements (one with low resolution for the DAQ, and one with high resolution) to improve the system dynamic range. A clear target response was observed. Several measurements are stacked on top of each other in Fig. 5.6, showing very good reproducibility between five runs. *The repeatability lays the foundation for the digital subtraction.* It also shows an impulse response with a fast decay from 3 V to about 5 μV (about 116 dB dynamic range) within about 100 μs .



(a) Low resolution
($\pm 5\text{V}$, $G = 1$)

(b) High resolution
($\pm 0.5\text{V}$, $G = 21$)

Figure 5.7 - Detection of a small target with coil-6 and P-cores at two different amplifier gains. The voltage on the plot is the sensor output voltage divided by the amplifier gain. The orange line is the sensor response with the target, the blue line is the background response (without the target), and the red line is the difference between two responses.

C. Anti-pulsing coil to reduce the primary pulse over the sensor cores

To evaluate the feasibility of using an anti-pulsing scheme to reduce the primary magnetic field over the sensor core material, we developed a simple lash-up at the early stage of the project. A second coil was wound on coil-6 to produce an opposite field to the primary field, as shown in Fig. 5.5(b). The field from the anti-pulsing coil is small and has negligible effect to the target. A driver circuit was developed to control the amplitude and phase of the current injected into the anti-pulsing coil. The lash-up was able to reduce the field in the sensor by a factor of 10 to 20. As we show in Figure 5.8 for a typical case, the anti-pulse coil reduces the field in the core by 10x, and improves sensor response at 100 – 200 μs duration where the system looks for early signals from a small target. The anti-pulse coil enables the sensor to reach a decay of about 120 dB within 100 μs even when the sensor is in the Tx coil with a field strength close to the field in the center of an EM-61 coil (about 100 μT).

In the final system, an anti-pulse coil was implemented for the Z-axis coil, see Fig. 5.2 above. The coil is simply connected in series with the Tx coil so it has the same phase as the primary field, with the strength controlled by the number of winding turns.

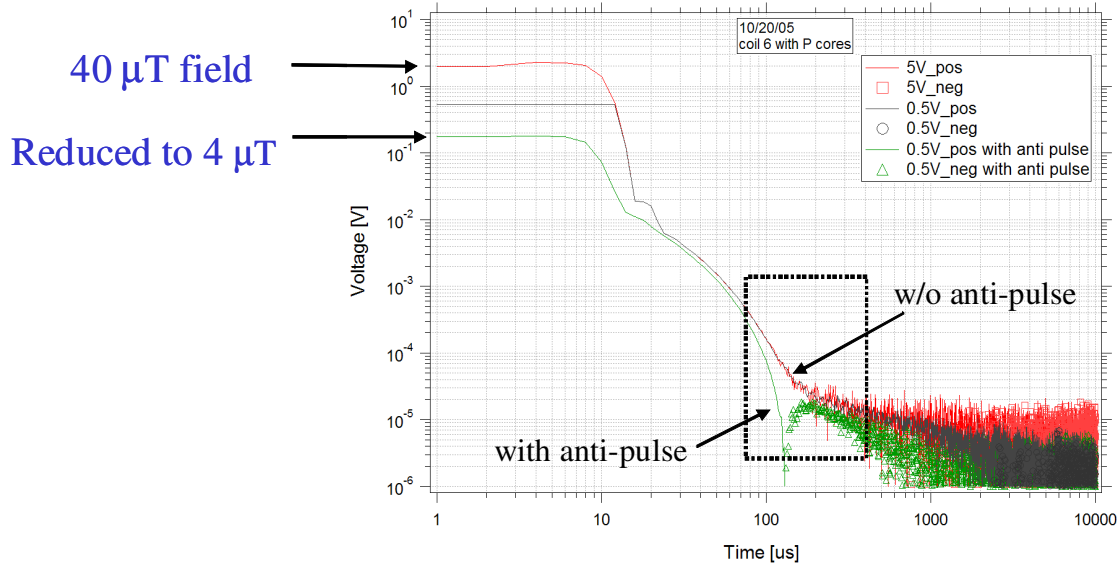


Figure 5.8 - Anti-pulsing Approach to reduce the field in the core

D. Vacquier Configuration for fluxgate

For the fluxgate magnetometer, we selected a two-core, parallel-gated sensor configuration (Vacquier) operating in the second-harmonic detection method (Ripka, 1991). It is classified as a parallel-gated fluxgate because the signal field, H_s , is parallel to the driving field that is generated by the current in the excitation coil. Each 4.5" long core is wound with an excitation coil see Fig. 5.2 above. The two excitation coils are connected in series, but oriented anti-parallel, such that they generate fields in opposite directions along the axis. Changes of the core permeability μ_r , due to the presence of an external magnetic field, cause the core field to change. An imbalance in the core fields then induces a voltage in the sensing coil. The two inner cores act as two separate coils in FG mode, and as a single high permeability coil in IS mode.

For the 3-axis implementation the driving field for the FG mode is turned on at the same time for all three axes. The excitation coils for 3 axes are connected in series with a serial resistor R_L ($1\ \Omega$) to limit the output current and a serial capacitor C_L ($3.6\ \mu\text{F}$) to resonant out the coil inductance and remove the DC component. The excitation coil for each axis has 100 winding turns (gauge #26 wire) wound on a small 5" long G-10 tube, with a winding length of 1.85". The magnetic field generated along the axis can be estimated using the long solenoid formula. The field is 0.26 Oersted for a driving current of 10 mA. The coercive force H_c of the selected core material is about 0.6 Oe. The dual-mode system uses an excitation current of 200 mA (amplitude) which corresponds to a field of approximately 5.2 Oe which is high enough to drive the core into a magnetic flux deep saturation state.

5.2.2. Receiver circuit board

The low-noise amplifier is another key component of the sensor. A high-level circuit diagram for a single-axis dual-mode receiver is shown in Figure 5.9. The blue parts are for induction mode, the red parts are for fluxgate mode, and black parts are shared for both modes. Multiple switches on the circuit board set the operation mode, controlled by the digital line D_0 and D_1 from the DAQ board. Two additional digital lines D_2 and D_3 (not shown in Fig. 5.9) on the DAQ generate the bi-polar Tx pulses for the induction mode. The time window for each mode and the switching sequence are programmed by the user via software on the PC. The fluxgate DC feedbacks are controlled by the D/A outputs (one for each axis). A clock of 4 kHz is selected for the final receiver, trading the switching speed and optimized sensor bandwidth; where half of the clock frequency, 2 kHz, sets the excitation frequency for the FG mode.

As we can see from the diagram, the receiver for the induction mode is fairly simple. A low-noise trans-impedance preamplifier measures the current which is proportional to the field in the sensing coil, and is followed by a voltage gain block. *The output voltage represents the B-field directly.* The serial resistor R_{coil} determines the low corner frequency of the induction sensor, $f_1 = R_{\text{coil}}/(2\pi L_{\text{coil}})$, and the impulse response time (also called recovery time). A larger R_{coil} gives a faster response, but also gives a higher low corner frequency (= less response at low frequency region). To balance the bandwidth and the recovery time, we selected $R_{\text{coil}} = R_{\text{damp}}/2$ for the receiver, where $R_{\text{damp}} = \omega_1 L_{\text{coil}}/2$ is the critical damping resistor of the sensing coil, and ω_1 is the resonance frequency of the coil.

The amplifier for the fluxgate mode is relatively complex, but follows the conventional fluxgate circuitry as described in the review paper by Ripka (1991). It includes an oscillator, filters, a current driver, a demodulator, and gain stages. The coil serial resistor R_{coil} is shorted during the FG mode to optimize signal-to-noise ratio (SNR). The oscillator generates a 2 kHz sine-wave current to the excitation coil and drives the core into a deep saturation state twice during each cycle. The DC magnetic field along the core direction is proportional to the amplitude of the second harmonic component (4 kHz) on the sensing coil. After demodulation, the output presents the DC magnetic field directly.

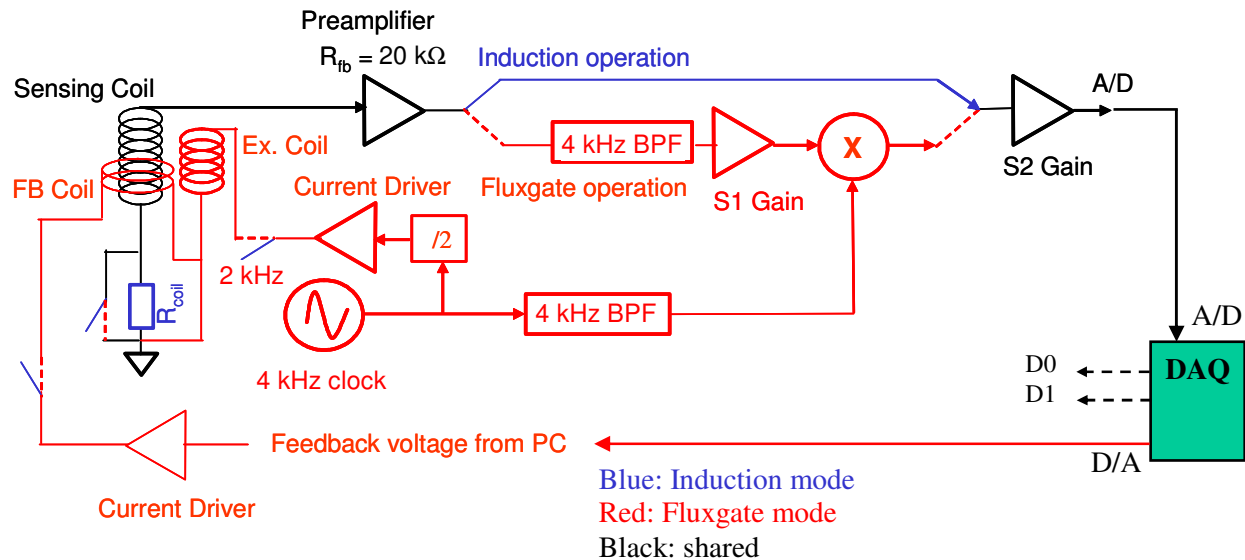
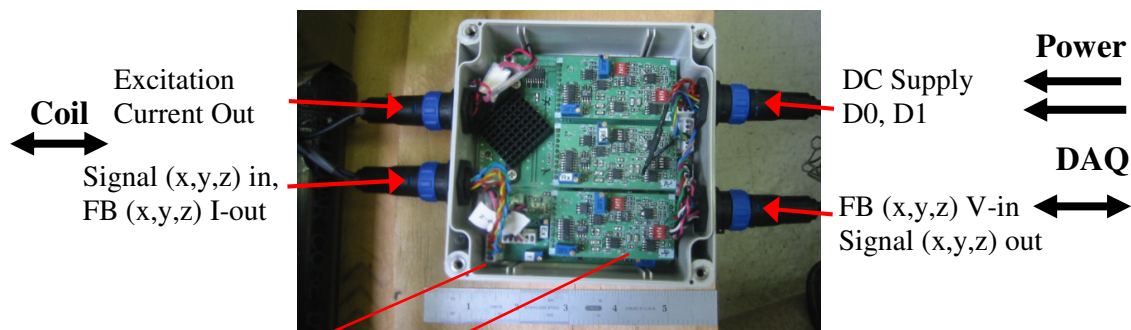


Figure 5.9 - High-level circuit diagram for the dual-mode receiver. Multiple switches on the circuit board control the operation mode.

In the FG mode, the receiver also outputs a feedback current for the "closed loop" operation. The DAQ generates a DC feedback voltage which is proportional to the output voltage, at the D/A output. The current driver converts the voltage into a current in the feedback coil. The feedback current creates an opposite field to the ambient DC field, and intends to zero out the DC field at sensor cores. The feedback current represents the measured DC field. This "closed loop" operation has much wider dynamic range than the "open loop" operation by virtue of bringing the signals of interest close to zero level.



Mother board: power conditioning circuitry, frequency source, excitation current driver

Daughter board (x3): preamp, mixer, filter, feedback current driver

Figure 5.10 - Electronics of 3-axis dual-model receiver

A photo of the integrated 3-channel receiver is shown in Figure 5.10. It has three daughter boards and one mother board. Each daughter board acts as the preamplifier for each axis, with the clock, excitation current driver, and power conditioning circuitry located on the mother board. The

design is very compact with robust connectors for signal inputs and output, excitation and feedback current outputs, and inputs for power supplies.

5.3 DAQ and software

The dual-mode receiver uses a 1 MS/s COTS DAQ card plugged into a PC to collect sensor data for all three channels and control the operation mode. The DAQ hardware has the following features:

- Uses a digital line D_0 from the DAQ to control switches in the receiver box and the sensor mode ($D_0 = 0$ for fluxgate mode; $D_0 = 1$ for induction mode)
- Uses a digital line D_1 to control delay of some components in the receiver box during the switching between two modes
- Collects sensor data by the channel A/D-0, 1, 2 for x-, y-, z-axis sensors, respectively
- Generates the bipolar T_x pulses for the induction mode by two digital lines D_2 , D_3 that have pulse width of 10 ms (can be adjusted by the software)
- Controls the Fluxgate DC feedback current for the fluxgate mode through digital-to-analog outputs D/A-0, 1, 2 for x-, y-, z-axis fluxgate, respectively

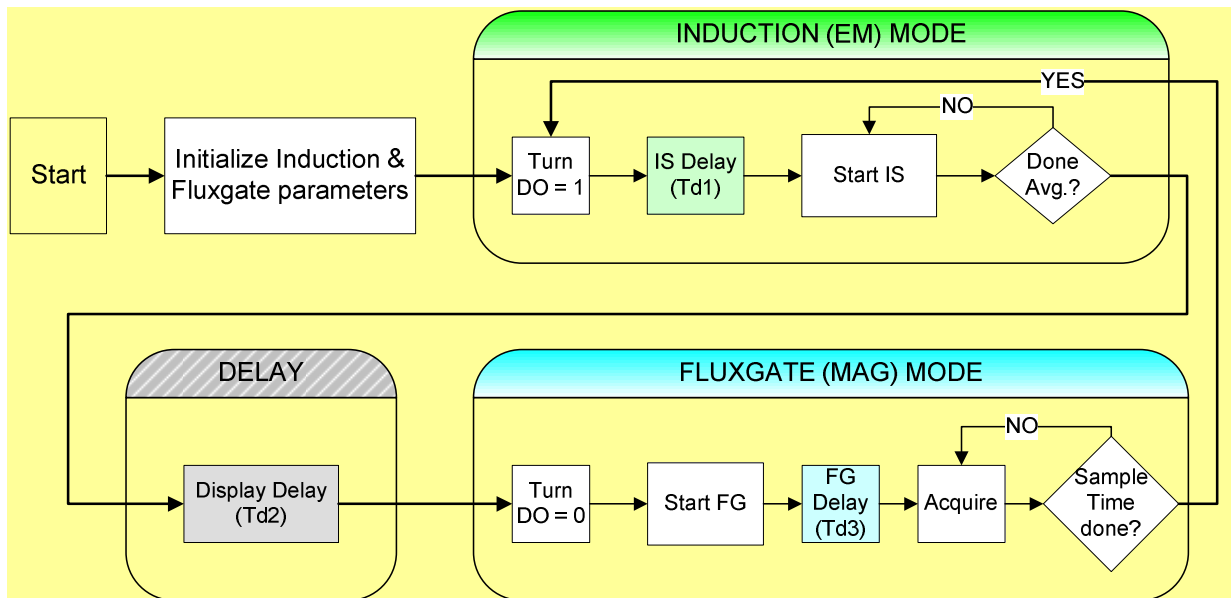


Figure 5.11 - Flow-chart of the program, for an FIS receiver operating in dual-mode operation between the induction sensor (IS) mode and fluxgate (FG) mode

A LabVIEW program to control the DAQ was developed. The program configures the receiver to operate in dual-mode sensing with serial time-sharing. The software consists of two core modules, one for the EM measurement (IS mode) in the time-domain, and one for the Mag measurement (FG mode). A flow-chart for the program is shown in Figure 5.11 and the user interface (UI) is shown in Figure 5.12. The parameter and control sections set the operation mode, DAQ channels, and measurement parameters for each mode. Four display windows show the measurement results. The time-domain response of the IS and FG modes, for the last scan, are shown in the upper left and lower left respectively. The IS response for fixed time gates is shown in upper right and the FG response vs. number of scan is plotted at lower right. The

number of scans represents the target-sensor position during the measurement. The code is optimized to minimize the program delay during switching from IS mode to FG mode, or from FG to IS mode, in the serial operation.

Stacking for induction measurement

Mode selection: Induction; Fluxgate; Dual-mode

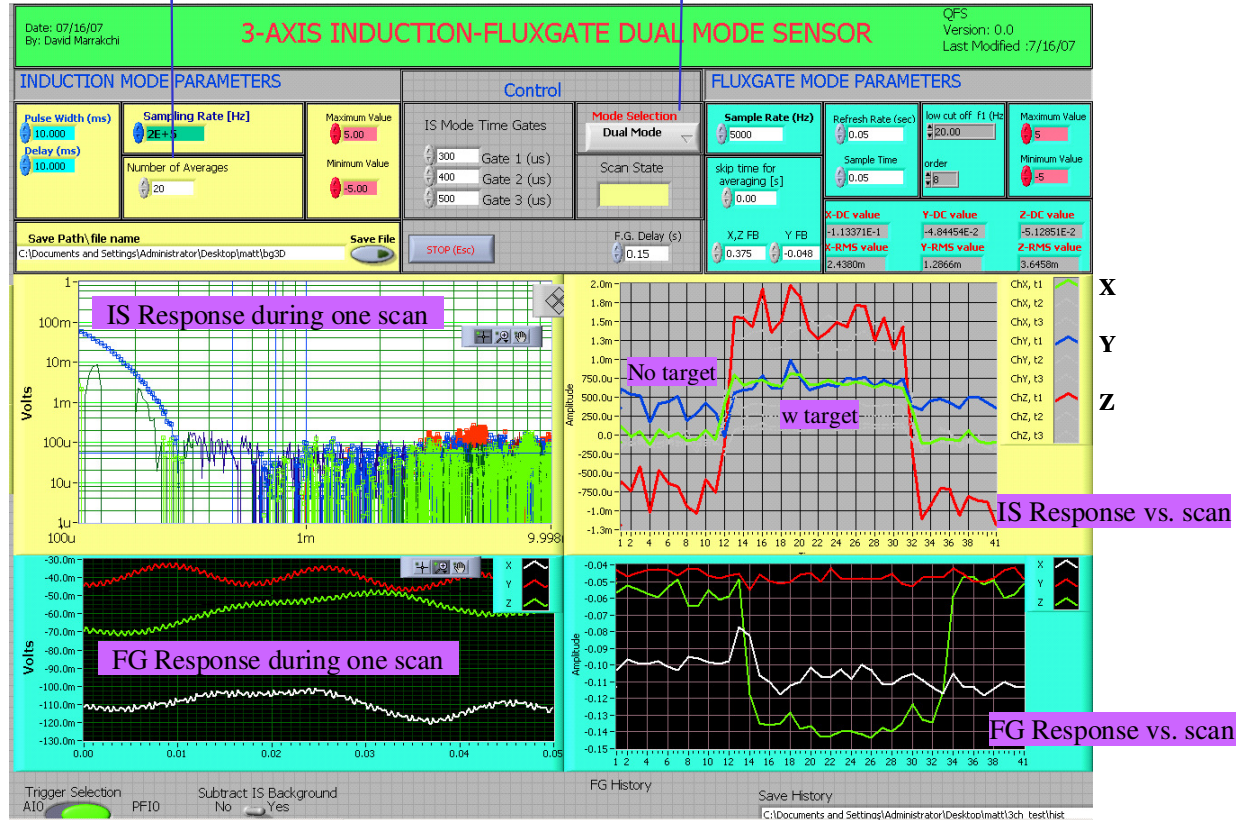


Figure 5.12 - User Interface for the dual-mode sensor

The program provides the following functions for the receiver:

- Set the measurement parameters and DAQ channels
- Send the pulses to the T_x coil, and collect IS time-domain response during the data collection windows; set the excitation and feedback currents, and measure the FG time-domain response;
- Perform data processing (such as stacking, background subtracting, averaging values inside the gate for the IS mode; and filtering, computing DC value and RMS noise for the FG mode)
- Save data for post processing

The code has been implemented for a 3-axis system. Some modifications are expected for the field unit. The code can also be modified for interleaved operation.

5.4 Other system components

The other system components are the T_x coil, the transmitter driver, and the power supply. The driver utilizes an H-bridge topology to generate bipolar current pulses in the coil with the positive pulses controlled by the digital line D_2 and the negative pulses controlled by the digital line D_3 .

During receiver system development, several large T_x coils were developed. Since we will mainly present results from two large coils in this report, we label them T_x coil #1 and T_x coil #2. The 1st coil (T_x coil #1) has a magnetic moment of $160 \text{ A}\cdot\text{m}^2$; the coil is $1 \text{ m} \times 1 \text{ m}$ and is made of 80 turns of 16 AWG copper wire, shown in Fig. 3.4. The wire resistance, $R = 5.2 \text{ Ohm}$, sets the maximum current of 2A when the driver is powered by a 12 V lead-acid battery. The coil generates $200 \text{ }\mu\text{T}$ (amplitude) bipolar magnetic fields at the center of the T_x coil, with a decay time constant of $20 \text{ }\mu\text{s}$, and a total turn-off time of $150 \text{ }\mu\text{s}$. As a comparison, the EM-63 system has a 3x high magnetic moment, $512 \text{ A}\cdot\text{m}^2$.

A higher magnetic moment can improve the FIS performance. We therefore made the 2nd coil (T_x coil #2) with the magnetic moment increased to $420 \text{ A}\cdot\text{m}^2$. The coil size was kept the same ($1 \text{ m} \times 1 \text{ m}$), but it was constructed of 96 turns of 14 AWG wire, shown in Fig. 3.5. The battery supply was also changed to 24 V from 12 V. The total turn-off time is slightly longer than coil #1, at about $200 \text{ }\mu\text{s}$.

5.5 Dual-mode operation

5.5.1 *Dual-mode operation with serial time-sharing*

The LabVIEW software, the sensing coil, and the circuit board have been fine tuned for dual-mode operation with serial time-sharing. We optimized the gating time for the dual-mode operation by minimizing the switching time between two sensing modes. The optimum gating time for the dual-mode operation with serial time-sharing is illustrated in Figure 5.13. In that case, the total operation time is about 1 second for one scan, which consists of 0.8 s for the IS mode, 50 ms for the FG mode, and 100 ms for the switching time. For the IS mode, 10 ms are needed for a T_x pulse, 10 ms for a measurement, 40 ms for a complete bi-polar cycle, and 20 stacked measurements are selected.

Two obstacles to dual-mode operation are magnetic hysteresis in the ferrite cores and thermally induced DC drift in the FG circuitry. Satisfactory results were achieved in minimizing these effects. In order to maintain the same magnetic flux in the core before and after the fluxgate mode, the system performs a slow (“soft”) turn-on/turn-off of the excitation current amplitude rather than employing a “hard” step change to the excitation current. The system needs 20 ms to turn-on/turn-off the excitation current. The switching time is limited partially by the LabVIEW program as well as the display, and partially by the ramp up time of the excitation current. It takes about 100 ms to switch between two modes for the prototype, but the switching time can be reduced by optimizing the code, using a faster PC, and a faster display. With a faster clock and optimized code, the switching time was reduced to 50 ms for a later version. For a commercial product, the delay could be minimized further with a customized DAQ and C-based code. The DC drift was greatly reduced with an improved circuit board with a larger thermal dissipating area, using an optimum excitation current, and utilizing a mini electric fan mounted on the circuit enclosure.

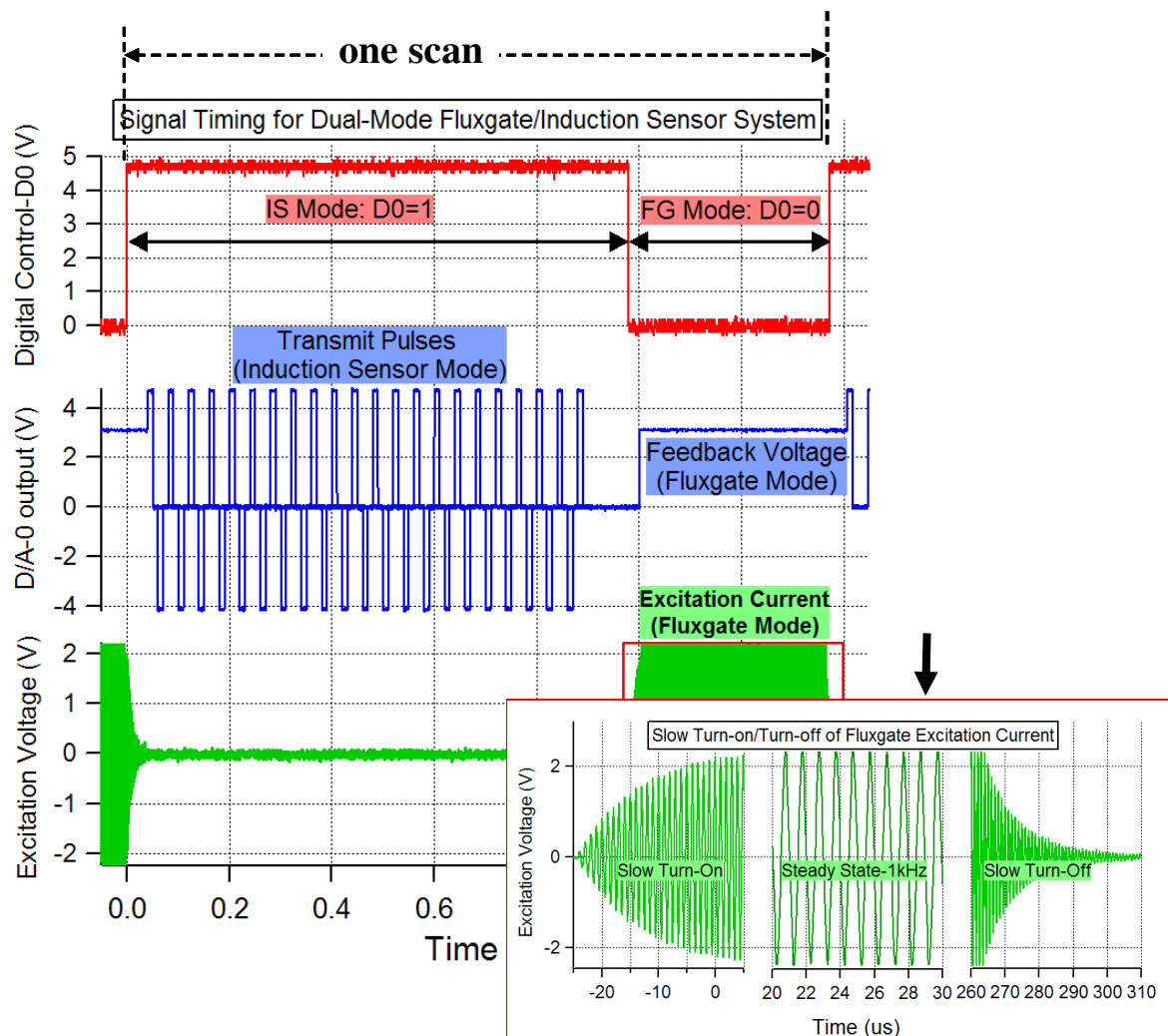


Figure 5.13 - Timing for the dual-mode operation with serial time-sharing during one scan. Inset shows the timing for the excitation current.

To qualify the dual-mode operation, sample data have been taken for the FIS in the lab for both 37 mm and 40 mm shells aligned in the vertical direction, moving slowly in 10 cm steps across 1.1 m centerline of the testing grid. The experiment was designed to simulate a simple outdoor one-pass survey case, with the FIS moving and scanning over a centered target, 55 cm below the sensor. Tx coil #1 was used for this data collection. Clear responses were observed with $\text{SNR} > 10$ when the target was directly below the sensor, at the 55 cm depth, Figure 5.14. The results demonstrate that the sensor system performs well for a true dual-mode operation. The final implementation of dual-mode operation for a field system will depend on the deployment concept and field test results.

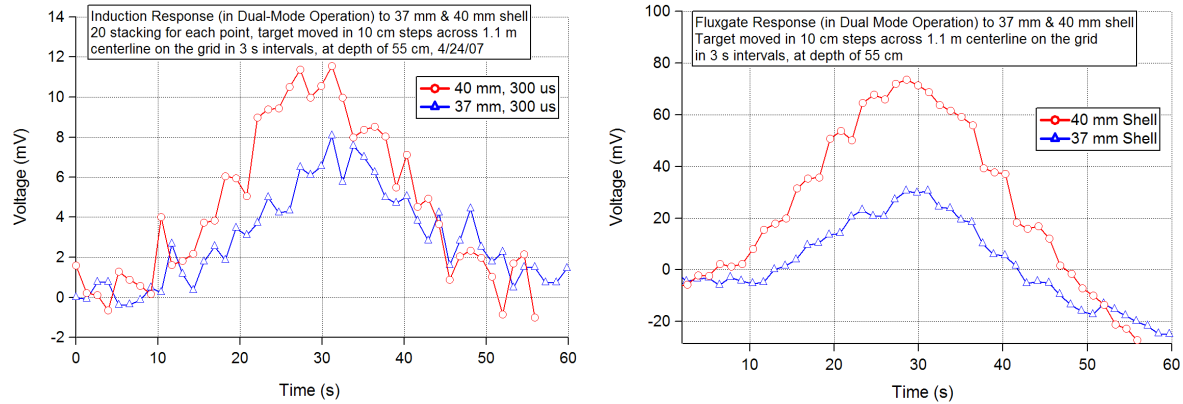


Figure 5.14 - Dual-Mode Sensor Response for 37 mm & 40 mm shell aligned in the vertical direction, moving slowly in 10 cm steps across 1.1m centerline on the testing grid. Left: Induction response; Right: Fluxgate response

5.5.2 Dual-mode operation with interleaved time sharing

Compared with serial operation, interleaved operation can have better spatial resolution for a sensor system on a moving platform during the survey. The time for each scan could be much shorter than 1 second. The interleaved operation may make field surveys faster. Two possible solutions have been identified.

Solution 1: Make fluxgate measurement after each induction measurement

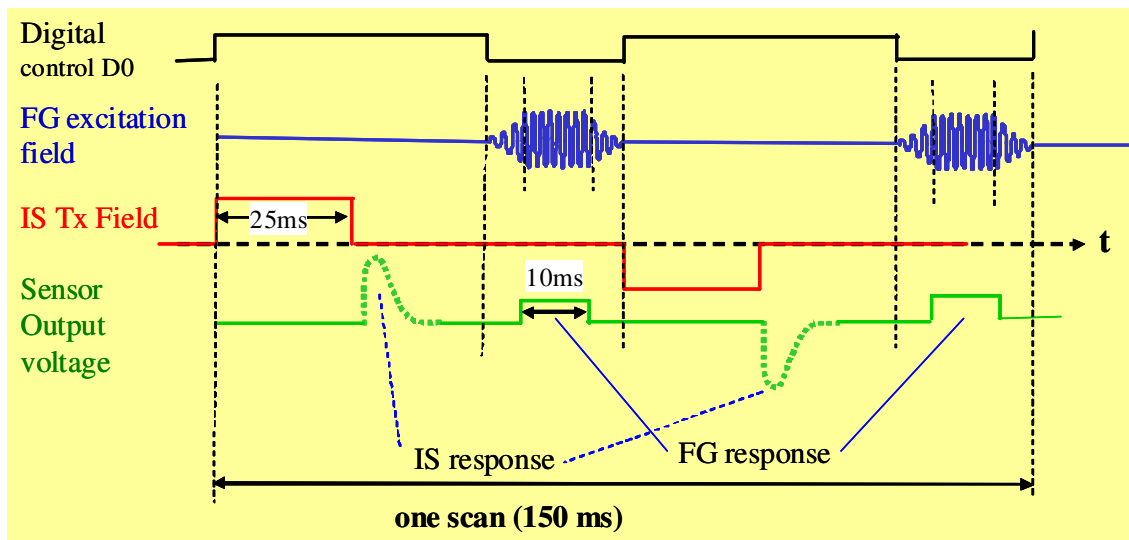


Figure 5.15 - Timing interleaved time-sharing (solution 1)

Basic interleaved operation, or serial time sharing, is achieved by making the Mag measurement after each EM measurement. The timing diagram is shown in Figure 5.15. The T_x pulse width is 25 ms, and the IS measurement window is 25 ms. The FG measurement window is 10 ms which is long enough for an excitation current of 2 kHz. The total time for one scan is about 150 ms. The turn-on/off time for the excitation current needs to be reduced to about 10 ms for solution 2.

Solution 2: Make fluxgate measurement while the Tx pulse field is on

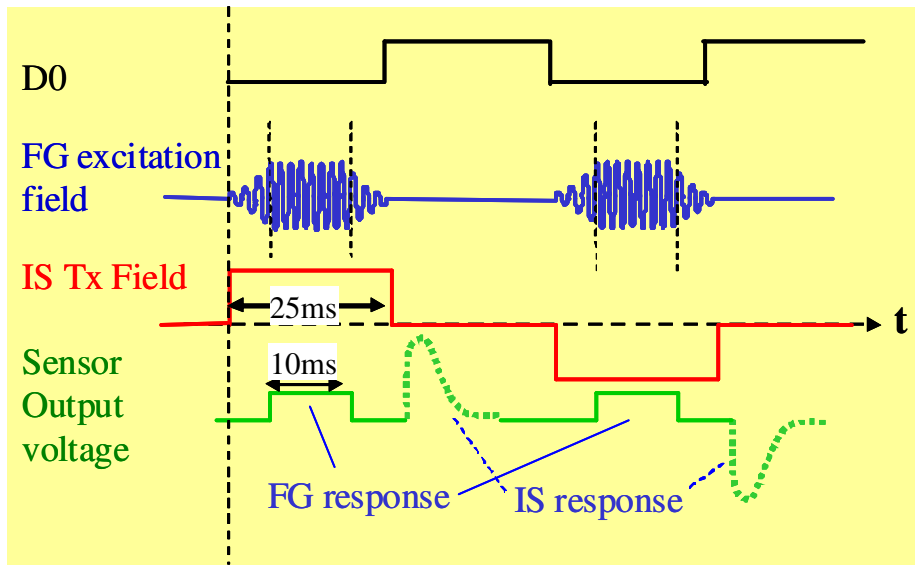


Figure 5.16 - Timing interleaved time-sharing (solution 2)

Solution 2 is a fast interleaved operation. The timing diagram is shown in Figure 5.16. The DC magnetic measurement is made when the T_x pulse field is on. The vertical DC magnetic field on the target is $B_{EARTH} \pm B_{TX}$ during the Mag measurement. The target magnetic response from B_{TX} can be cancelled by stacking two Mag measurements during one cycle. The magnetic flux induced by the T_x field in the two ferrite cores is negligible compared with the 2 kHz field generated by the excitation coil, because there is an anti-pulsing coil wound on the R_x probe. The T_x pulse width is 25 ms, and the IS measurement window is 25 ms. The FG measurement window is 10 ms. The total time for one scan is 100 ms. This solution is faster and has less delay between EM measurement and Mag measurement, but it needs more effort to implement than Solution 1.

The final implementation of the dual-mode operation will depend on the deployment concept and field test results of the dual-mode operation.

6. MATERIALS AND METHODS - DATA MODELING

The modeling effort is an important piece of the project. The modeling results help us to quantify the sensor performance. In this section, we describe the methods that were selected to model the FIS data, for the EM induction measurement and DC magnetometry measurement. We also detail a study on the bandwidth requirements.

6.1 EM induction

A parameterized approach to physics-based, time-domain EM modeling of compact, conductive objects was first suggested by *McNeill and Bosnar* (1996) and *McNeill* (2000) and subsequently implemented by *Pasion and Oldenburg* (2001) and *Grimm* (2003). Targets are treated as three orthogonal, infinitesimal dipoles. Geometric factors of field strength are computed from the position and orientation of each dipole with respect to the transmitter (i.e., the primary field) and the position and orientation of the receiver with respect to each dipole (i.e., the secondary field). The induced signal in each dipole is assumed to decay as $\beta(t+\delta)^{-\gamma}\exp(-\alpha t)$. This is a parameterization of an infinite sum of exponentials that describes the formal mathematical solutions to time-domain induction in spheres and plates; there are no analytic solutions to more complex objects. We call this temporal-spatial approximation the *Time-Domain Three Dimensional (TD3D) model*.

Physically, the β parameters are amplitude constants proportional to the overall polarizability, whereas the δ , γ , and α parameters describe the early, intermediate, and late-time responses of a conductor (*McNeill and Bosnar*, 1996). Early time, just after transmitter turn-off, is characterized by a near-constant magnetic field in the target that is established by surface eddy currents as a consequence of Faraday's Law. As eddy currents diffuse into the object's interior, the magnetic field decays approximately as $t^{-\gamma}$, with $\gamma \sim 1/2$ for the magnetic field and 1.5 for induction-voltage measurements. This is intermediate time. The time δ marks the early-to-intermediate transition. Finally, eddy currents penetrate the entire body during late time, which is characterized by an exponential decay of the magnetic field with time constant α . In a log-log plot, early time is flat, intermediate time is a straight line, and late time is concave down. A plot of sensor response (V), collected by the vertical axis of the 3-axis sensor over a copper sphere is shown in Figure 6.1. The figure also shows model fits to the intermediate and late times of the decay for the spherical target. Early time is obscured by transmitter recovery. The parameter, γ , is about 1 on the plot, which is due to the frequency response of the sensor; discussed/plotted in Section 7. Although γ value differs from the model, the discrimination results based on the ratio of γ between different axes of the target seem to not be affected.

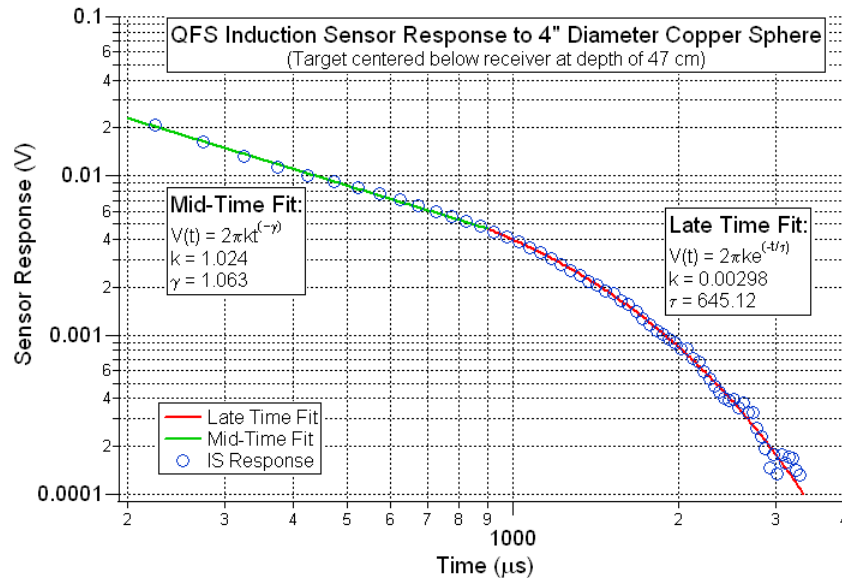


Figure 6.1 – Model fit to vertical induction sensor data collected for Copper Sphere.

With three orthogonal dipoles, the EM response of a variety of shapes can be approximated. The three dipoles representing a sphere are equal in all parameters. Cylinders and circular plates are axisymmetric but differ in that cylinders have the largest $\beta_1 > \beta_2 = \beta_3$, whereas circular plates have $\beta_3 < \beta_2 = \beta_1$. Other parameters have similar symmetries although not necessarily in the same order. A triaxial object (e.g., a rectangular block or plate) would have unequal parameters in all three dipoles. The TD3D parameterization requires up to 7 free parameters for a sphere ($x, y, z, \beta_1, \gamma_1, \alpha_1, \delta_1$), up to 13 for an axisymmetric object (3 for location, 2 for orientation, 2 each $\alpha, \beta, \gamma, \delta$), and up to 18 free parameters for a triaxial object (3 positions, 3 orientations, 3 each $\alpha, \beta, \gamma, \delta$). In practice, only those parameters are used to which a sensor system is sensitive. The FIS is limited to intermediate time in the objects analyzed here, so the α and δ parameters can be neglected. In this paper, therefore, a sphere model is 5 parameters, an axisymmetric model is 9, and a triaxial model is 12 parameters. For visualization purposes, target orientations (azimuth, inclination, and roll) are expressed with respect to a symmetry axis if present.

6.2 DC magnetometry

A similar model of three orthogonal dipoles was used to calculate the vector DC magnetic response by *Billings* (2006). It is considerably simpler than TD3D because there is no dependence on transmitter geometry (the source field is constant) and there is no time dependence. A sphere requires 4 parameters (3 position, 1 polarizability) and a triaxial object needs 9 parameters (3 position, 3 orientation, 3 polarizability). Parameter estimation was performed by gradient descent.

6.3 Bandwidth requirements

Two approaches can be employed to determine requirements: theory and experiment. Both can be examined in the time or frequency domain.

The equivalent four-parameter frequency-domain response can be written

$$A(f) = X + iY = q\{s + [(i\omega\tau)^c - 2]/[(i\omega\tau)^c + 1]\} \quad (1)$$

(Miller *et al.*, 2001). The zero-frequency intercept of the real component is the magnetization, and the real component approaches unity at infinite frequency as a perfect reflection. The quadrature component is asymptotically zero at low and high frequency but peaks at the point of maximum inflection in the real component. The late-time constant $\alpha = \omega_p = 2\pi f_p$ is shown in Figure 6.2.

Grimm *et al.* (2003) fit Eqn. (1) to synthetic data for axisymmetric ellipsoids produced by the numerical model of Shubitidze *et al.* (2002). These results are summarized in Table 8. A time series that spans $[\delta, \alpha]$ will robustly capture the principal inductive behaviors in the time domain. For the commonly considered range of ordnance (20 mm – 155 mm), the smallest time is $\delta = 1 \mu s$ for a 20-mm projectile and the longest time is $1/\alpha = 48 \text{ ms}$ for a 155-mm projectile. For $\omega\tau = 1$, these times translate to frequencies of 3 Hz – 160 kHz.

The great variety in ordnance construction and indeed variations even for similar ordnance tend to obscure most regular progression in model parameters with size. Under SERDP sponsorship, AETC, Inc. has developed a database including approximately 7000 GEM-3 frequency-domain spectra, comprising dozens of distinct objects at many distances and orientations from the sensor, Figure 6.3. The GEM-3, manufactured by Geophex Ltd., uses a fixed arrangement of circular coils to measure the in-phase and quadrature components of EM response up to 96 kHz. Jonathan Miller of AETC kindly provided that database for this investigation.

The frequency of peak quadrature response was selected as a simple indicator of the frequency around which maximum information on the target could be recovered. The data were screened to eliminate apparent peaks occurring at either the high or low end of the frequency band. In practice, model fitting is sensitive to quadrature peaks beyond the recorded bandwidth. "Canonical" UXO were selected from the remaining data (20 mm, 60 mm, 81 mm, and 105 mm projectiles), as well as UXO fragments.

The scatter in quadrature-peak frequencies is very broad, and shows little or no correlation with object size: lower frequencies (longer time constants) would be expected for larger objects, shown in Table 9. Quadrature peaks are distributed from $< 100 \text{ Hz}$ to $> 20 \text{ kHz}$, over essentially the full bandwidth of the GEM-3. These bounds nonetheless lie within those developed above (3 Hz – 160 kHz) for idealized UXO.

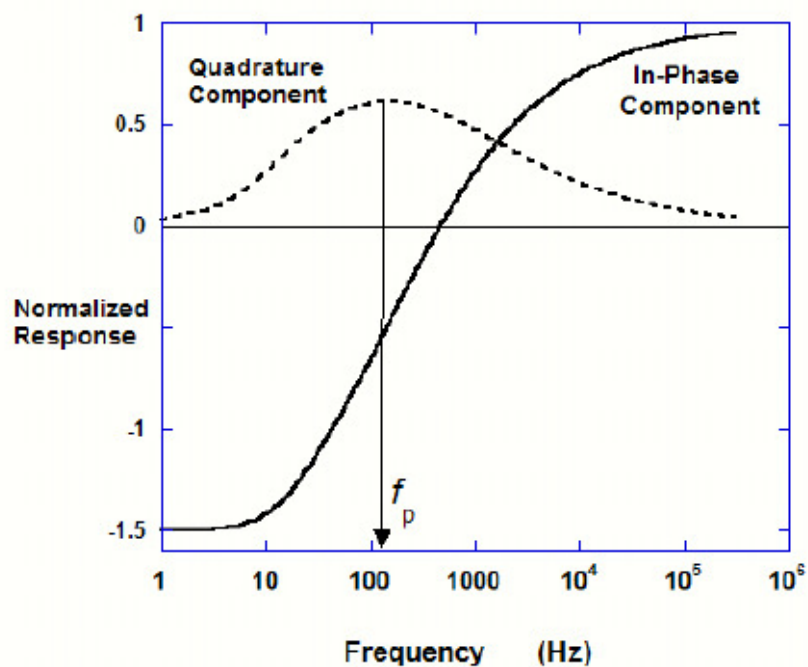


Figure 6.2 - Example frequency-domain complex response of a magnetic object. Peak quadrature response occurs at f_p .

Table 8 - Time-Domain Model Parameters for Selected Ordnance

Target		β	α , 1/ms	δ , ms
20-mm	Axial	8.78e5	1.25	0.036
	Transverse	1.06e5	1.25	0.001
40-mm	Axial	1.40e7	0.3125	0.144
	Transverse	8.44e5	0.3125	0.005
81-mm	Axial	2.36e8	0.0762	0.591
	Transverse	9.81e6	0.0762	0.020
155-mm	Axial	3.16e9	0.0208	2.163
	Transverse	1.31e8	0.0208	0.072
1000-lb	Axial	8.80e10	0.004	11.41
	Transverse	3.65e9	0.004	0.380

Table 9 - Median Frequencies of Peak Quadrature Responses

Target	105 mm	81 mm	60 mm	20 mm (hi)	20 mm (lo)	fragments
Median, Hz	330	330	570	10830	210	1590

Separate medians computed for bimodally distributed of 20-mm responses.

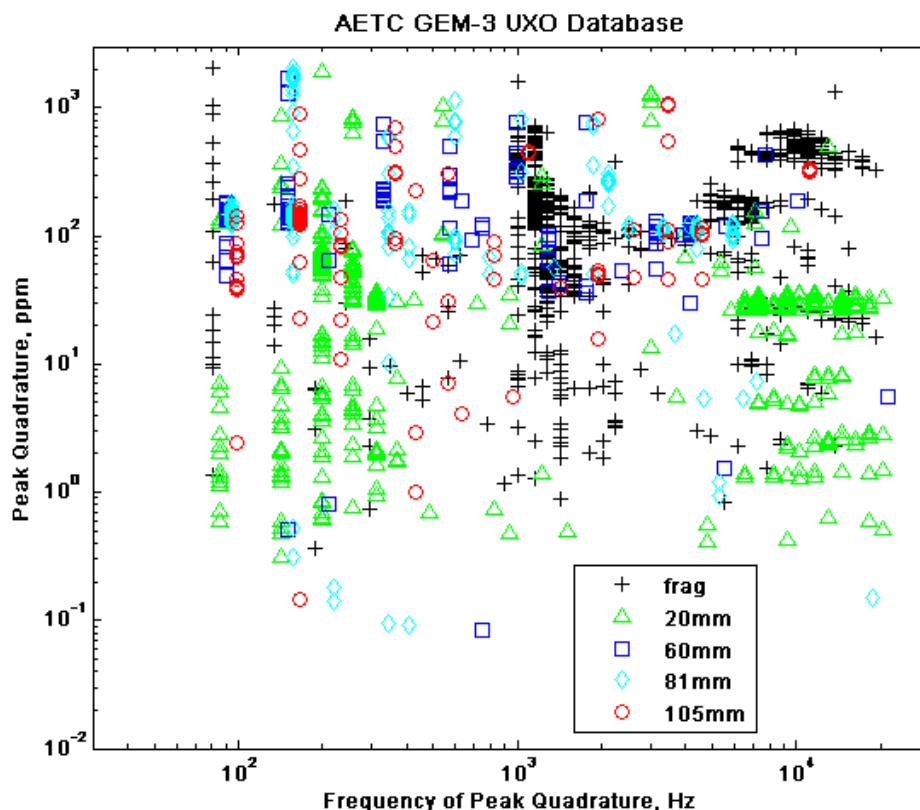


Figure 6.3 - Frequency of peak quadrature response from canonical UXO and fragments in AETC GEM-3 database. There is little correlation between object size and quadrature-peak frequency.

Time-domain EM-induction responses of several dozen test objects buried at the Blossom Point, MD, test range established by NRL were analyzed by *Grimm* (2003); these objects are a small subset of the AETC database. The lack of correlation of model parameters with size was generally confirmed, with the exception that the larger ordnance and ordnance-like objects approximately recovered the theoretically expected $\gamma = 1.5$, whereas γ for scrap-like objects varied widely. This is attributable to a sustained intermediate-time diffusion phase, enabled by magnetic permeability and thick walls of the test objects. Note, however, that this study showed how overall shape could be discriminated using the ratios of parameters in each of the three principal axes. In this way, elongated UXO can be separated from flattened or arbitrarily shaped scrap objects.

In summary, the large empirical distribution in the peak quadrature frequency response in ordnance—or equivalently, the variation in time-domain time constants—precludes model-based definition of sensor bandwidth requirements. This very scatter, however, indicates that useful bandwidths should be comparable to the GEM-3 range. A dual-mode fluxgate/induction sensor can easily completely capture the low end to DC, and the prototype FIS response demonstrated to date indicates that the high end is also achievable.

7. RESULTS AND DISCUSSION - SYSTEM PERFORMANCE

The integrated dual-mode receiver has been designed, built, and characterized in a controlled environment. Its detection and discrimination capability have been compared with commercial sensors during the project. The advantage of 3-axis sensor vs. 1-axis sensor is clearly demonstrated by comparing the model fit for EM measurement with 1-component and 3-component data for a 37 mm shell.

7.1 Sensor performance

7.1.1 EM induction

When the receiver operates in the induction mode, the T_x coil generates bipolar magnetic pulses in the vertical direction with the pulse width of 10 ms or longer. The sensor measures the electromagnetic field generated by the eddy currents in the target, at 100 μ s to 10 ms after the T_x field is turned off. Stacking of 10 to 100 is used to improve the SNR. The sensitivity of the sensor in the induction mode is shown in Figure 7.1. It has a noise spectrum density of about 0.2 pT/rHz at 1 kHz. The total rms noise is less than 20 pT in the band of interest (100 Hz to 10 kHz). All three axes show similar sensitivity. The cross-couplings for the 3-axis unit were measured, and the values are less than 1% between axes.

To verify the sensor performance, the induction sensor has been compared with a Geonics EM63 system by using a 37-mm shell on the testing table shown in Fig. 3.4. The target is moved through an 11x11 grid, with response collected at each location. The surface plot shows the sensor response, at one instant in time, to the EM field generated by decaying eddy currents in the target. The T_x coil #1 was used for collecting the data set. The target response at three time gates for both the FIS and the EM63 are shown in Figure 7.2 for the target in a vertical orientation and in Figure 7.3 for the target in a horizontal orientation. A comparison of target response vs. depth for both sensors at the 336 μ s time gate is also shown in Figure 7.4. Please note: the FIS measures the B-field directly while the EM63 measure the dB/dt.

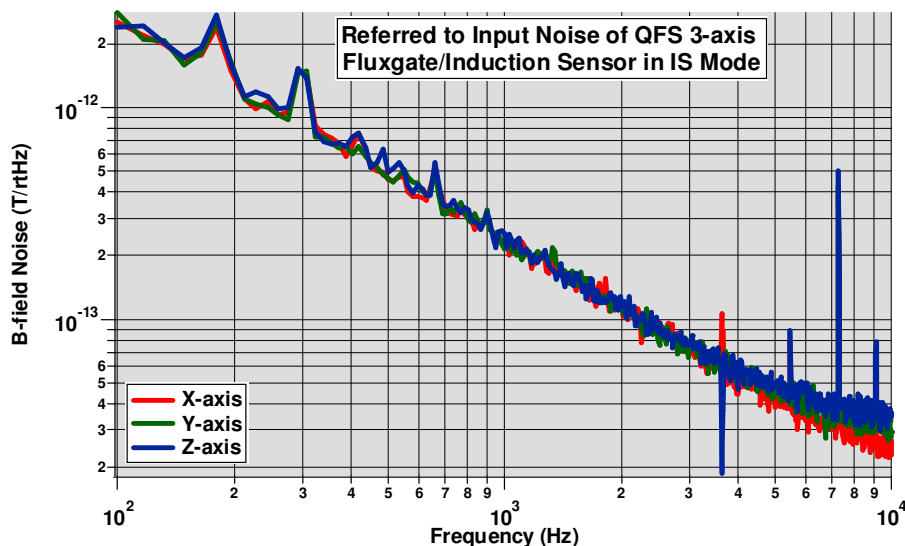


Figure 7.1 - Sensor noise in the induction mode

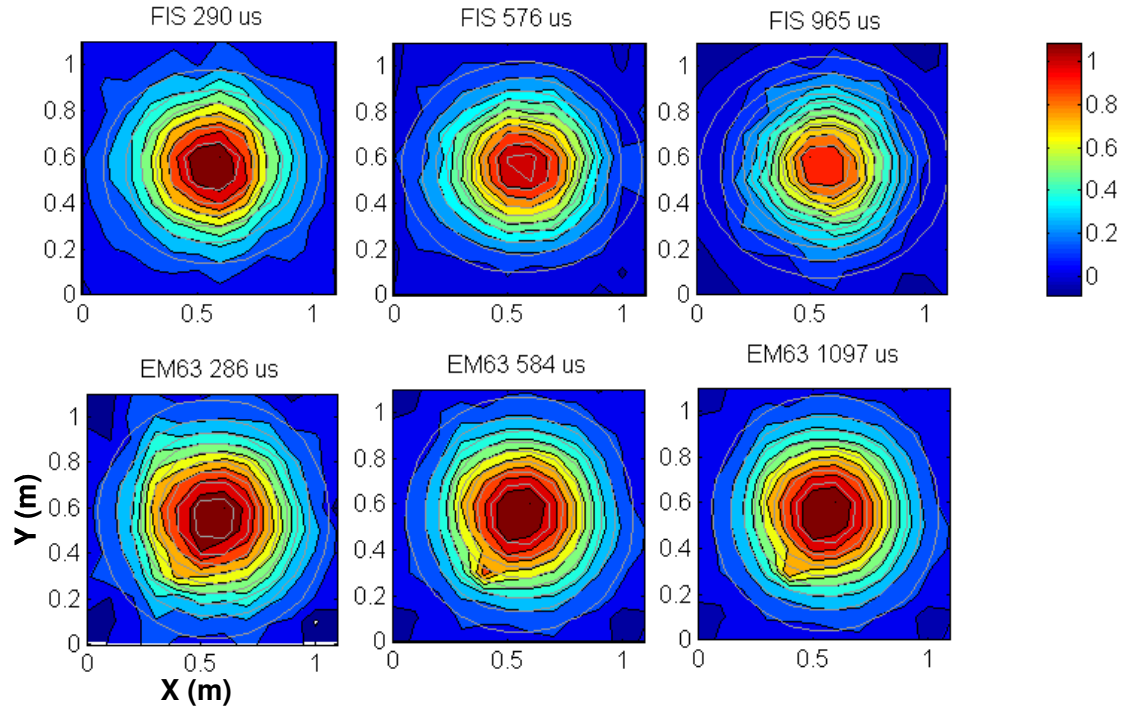


Figure 7.2 - Comparison of FIS and Geonics EM63 induction data for 37 mm shell in vertical orientation (collected at QFS Lab), 55-cm distance. Signals (B for FIS, dB/dt for EM63) are normalized at each time slice. Light contours are model fits.

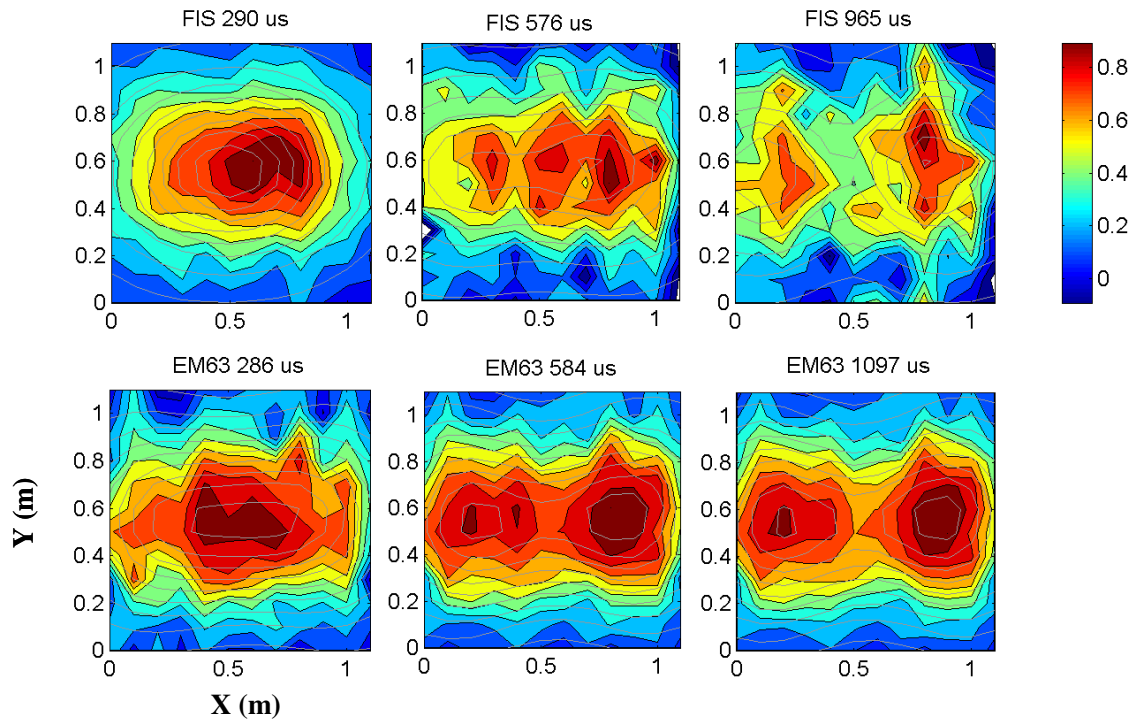


Figure 7.3 - As Fig. 7.2, with 37-mm shell in horizontal orientation.

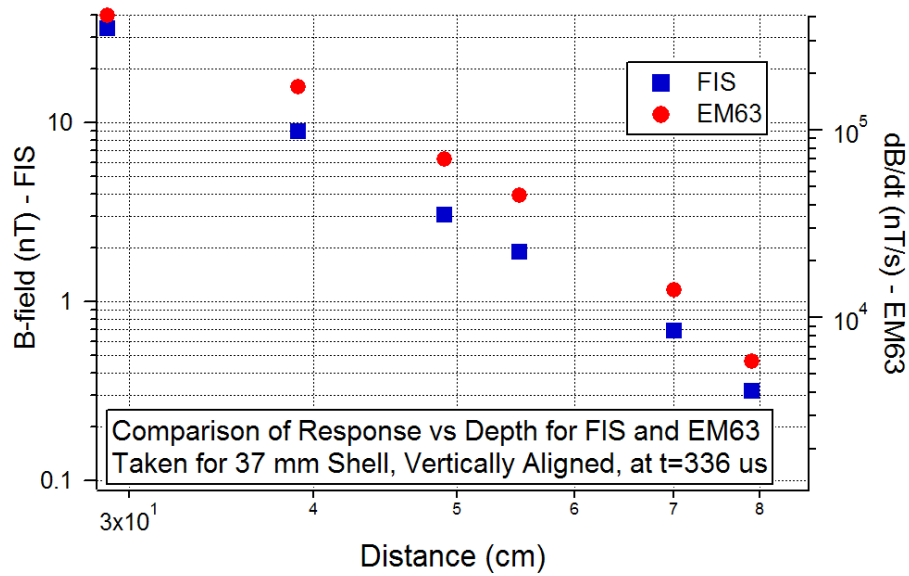


Figure 7.4 - Dependence of the response vs. depth for FIS and EM63 for a vertically aligned 37-mm shell, at the time gate 336 μ s.

Table 10 - TD3D model results

Target Parameter	FIS-Vert	EM63-Vert	FIS-Horiz	EM63-Horiz
Variance Reduction (goodness-of-fit)	94%	99%	90%	96%
x, m	0.57	0.55	0.56	0.56
y, m	0.57	0.56	0.49	0.54
Z*, m	0.08	-0.15	0.05	0.07
azimuth, deg	74	51	29	265
inclination, deg	94	88	92	89
roll**	0	0	0	0
β_1	15	2.2	2800	3.8
β_2	1.5	1.2	440	1.9
β_3	1	1	1	1
γ_1	0.28	0.62	1.65	1.05
γ_2	0.59	0.68	1.39	1.56
γ_3	0.52	0.68	0.14	0.62

* Target distance below ground; sensor is 40 cm above ground

** Roll is the third Euler angle as used in aerospace. It is only used when the target is 3D. It has no meaning on a body of revolution. We note it as zero in the table.

These measured results show that the FIS compared favorably with the EM63. We have also verified the quality of the 37-mm shell data with TD3D modeling. Each data set is a hypercube comprising an 11x11 spatial grid at numerous time gates. Data are binned in logarithmic time gates.

The modeling results are shown in Table 10. Data quality appears to be good throughout the time decay (about 1 ms). The variance reduction (goodness-of-fit) is good for both the FIS and the EM63. The TD3D fit infers an axially symmetric object in the β -parameters with the different axis being the largest—referred to here as a cylinder. The low γ values are, however, are closer to those derived for small, tri-axial objects (scrap) than the canonical value of 1.5 expected for intermediate-time decay expressed in large targets (*Billings, S. et al, 2003*). The transition from early to intermediate time (δ) is unremarkable for all tests, ranging up to ~0.1 ms. No exponential (late-time) decay was observed in any of the tests (all $\alpha = 0$). TD3D modeling of EM63 data of the vertical shell also indicated a vertical cylinder, although the ratio of maximum to minimum polarizability was smaller than for the FIS. The EM63 data are slightly better, yielding somewhat higher variance reduction.

For the horizontal 37-mm shell, the model incorrectly infers a tri-axial (book-like) target with the largest axis vertical and the intermediate axis horizontal and in the direction of the shell (Table 10). The ratio of maximum to minimum polarizability is even larger than in the vertical case. The γ parameters are, however, closer to the theoretically expected value.

In spite of these discrepancies with the actual shape, nearly identical parameters were derived for the FIS and the EM63. Parameters β correctly imply a quasi-cylindrical object for a vertical target, while parameters incorrectly imply a tri-axial object for a horizontal target. The mixed results in shape recovery from TD3D, common to both the FIS and EM63, are simply due to the lack of multiple sensors and/or spatial components. For example, *Grimm (2003)* found that incorrect shape inferences were dramatically reduced when measuring three components of the induced field at a single location. A three-component FIS would similarly enable robust target-shape characterization. Our 3-component data also demonstrated the usefulness of 3-axis sensor (see Section 7.2 below). The comparison indicates that the FIS performs adequately in the induction mode.

7.1.2 DC magnetometry

When the system operates in the fluxgate mode, the sensor measures the magnetic field response of a shell which indicates the field distortion caused by a ferrous target to the Earth's DC magnetic field. The response is a DC field with a fall off rate of $1/\text{distance}^3$ while the EM response has a fall off rate of $1/\text{distance}^6$. Mag measurement is therefore able to detect deeper targets than EM measurement, depending on the target size, the magnetometer internal noise and geology. Mag measurement also provides information about the magnetic properties of the shell and the material inside the shell. A ferrous target is often modeled by the standard dipole model for the Mag measurement.

The measured rms noise of a single axis FIS is 1 nTrms (with a magnetic field noise spectrum density at the sensor input as 0.1 nT/rtHz at 1 Hz), but the noise increased to 2-3 nTrms for 3-axis version. The added noise may be due to sensor noise from other axes coupled to the measured axis from the connected excitation coils. As we discuss later, the two horizontal

fluxgates do not add additional information to the target discrimination capability of the dual-mode receiver; it is enough to keep just one vertical fluxgate in the next version, which will make the receiver simpler and more sensitive in the FG mode.

The single-axis FIS has also been compared in fluxgate mode to a commercial fluxgate (CFG) magnetometer by using a 37-mm shell on the same testing table. The surface plot shows DC field for each target position. The CFG has a sensitivity of 1 nTrms. The magnetic responses for both the FIS and the CFG are shown in Figure 7.5 for the target in a vertical orientation. A comparison of target response vs. depth for both sensors is shown in Figure 7.6. Measured field strength falls off with target distance as $1/r^n$, with $n = 3.4$ for the FIS, and $n = 4$ for the CFG. The discrepancy from the dipole model ($n = 3$) is probably due to the presence of higher-order poles when a target of finite size is close to the sensor, and/or is due to distortion from metals in the (building) ground when the target depth, r , is close to 1 m.

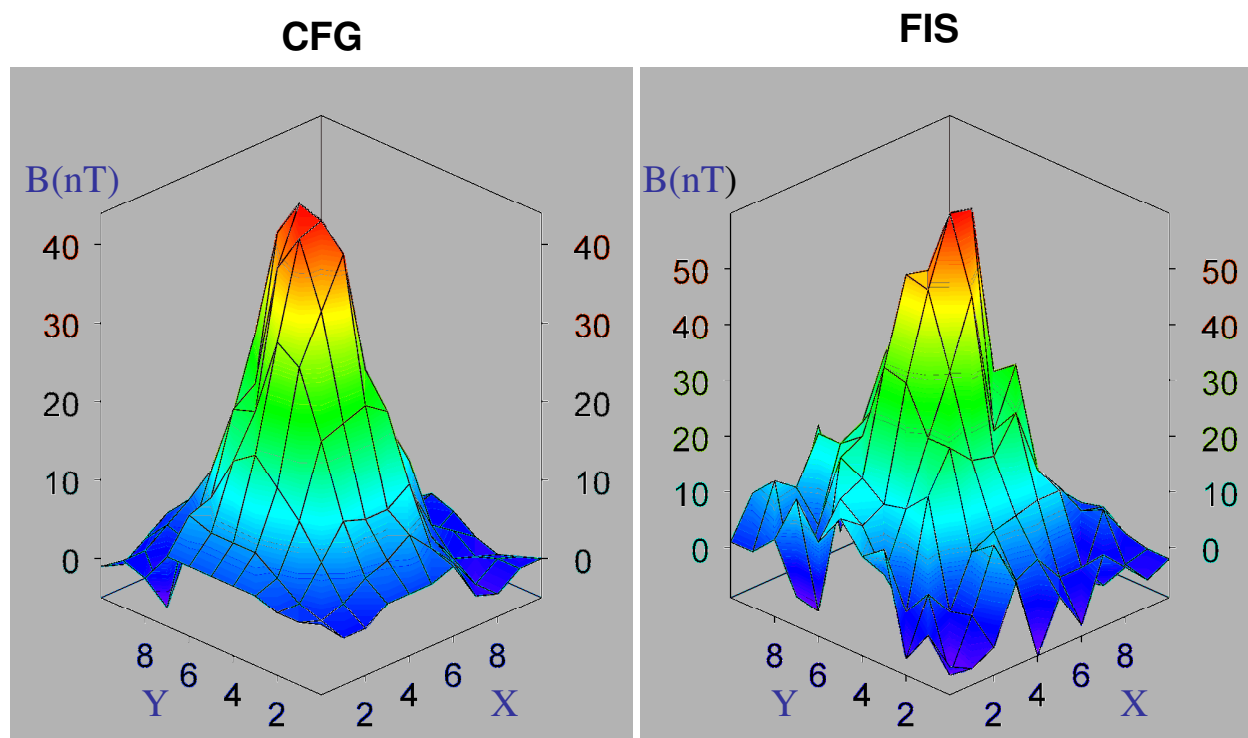


Figure 7.5 - Comparison of Commercial Fluxgate (CFG) and FIS in DC fluxgate mode for 37-mm shell vertically aligned over the grid (same coil and receiver as the induction mode).

We have verified the quality of the grid magnetic data with the standard dipole model. The results are shown in Table 11. The fit quality is good. Data from both sensors indicate near-vertically oriented dipoles and the dipole moments are in reasonable agreement. The recovered target positions are also in good agreement. Although the FIS does not show the expected smooth falloff with distance exhibited by the CFG (Figure 7.5), the modeling results show that the FIS still compares favorably with the CFG. We believe the non-smooth falloff on the FIS data (Figure 7.5, collected in Year 2) is due to thermally induced DC drift in the FG circuitry. The DC drift issue was later greatly reduced with an improved circuit board with a larger thermal

dissipating area, and utilizing a miniature electric fan mounted on the circuit enclosure (implemented in Year 4). As an example, the target over grid data collected in Year 4 for a steel rod has a very good VR and smooth falloff with the distance (Table 19 and Figure 8.9). We conclude that the FIS performs adequately in magnetometer mode.

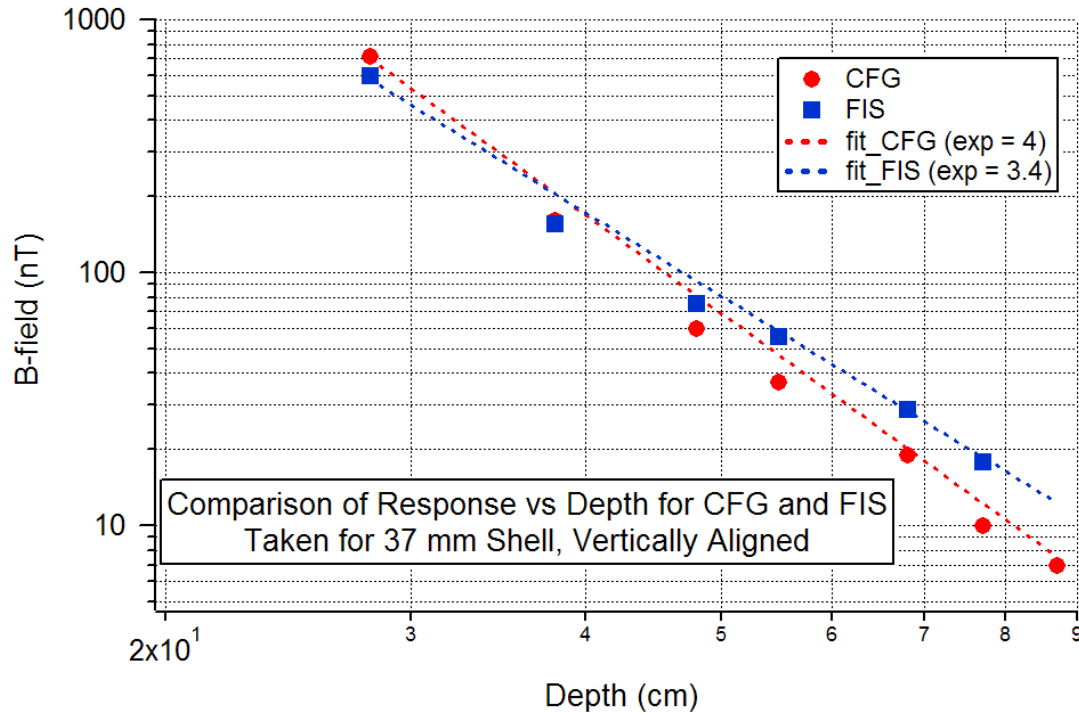


Figure 7.6 - Dependence of magnetic response vs. target distance for FIS and CFG for a vertically aligned 37 mm shell

Table 11 - Dipole Model Fits to Magnetic Grid Data

Target Parameter	FIS	CFG
x, cm	53	54
y, cm	52	50
z, cm	43	42
Azimuth, deg	-34	6
Inclination, deg	85	84
Dipole Moment	5.2×10^{-5}	4×10^{-5}
Variance Reduction	90%	96%

7.1.3 Discussion on the comparison results

The direct comparison of the FIS in the induction mode with the EM63 and in fluxgate mode with the CFG validates the performance of the FIS. In both induction and magnetometry studies, the target properties modeled using FIS data were comparable to those collected from the commercial systems. The compact, dual-mode FIS compares favorably to each of the commercial instruments, albeit at somewhat lower SNR. The vertical orientation of the test 37-mm projectile has been correctly modeled in both modes, and the quasi-cylindrical shape of the

shell has also been recovered in the multi-time channel induction data. However, target shape was not correctly inferred from the induction data when the shell was horizontal. This shortcoming was common to both the one-component FIS and the EM63 and is simply a reflection of an inadequate variety of data for robust modeling (*Grimm, 2003*). A three-component FIS will ultimately overcome the shortcoming.

The variance reduction (goodness-of-fit) for the EM63 is slightly better than for the FIS, but still comparable (see Table 10). This may be due to the fact that the EM63 uses a reference coil to cancel noise and has 3x higher magnetic moment for the T_x coil than the FIS system (with T_x coil #1). The FIS is much more compact than EM63; therefore it is feasible to construct an array or a three-axis sensing system with improved performance.

The FIS data appear to degrade relative to those of the EM63 at times greater than 1 ms, but this does not appear to affect the ability of comparable target characterization to be inferred from both data sets. The response at times greater than 1 ms can be improved by using a T_x coil with larger magnetic moment¹, or/and reducing the corner frequency f_1 of the FIS with a smaller serial resistor R_{coil} in the circuit shown in Fig. 5.9.

7.2 Three-component data

To verify the usefulness of a 3-axis receiver, we quantified the improvement of the 3-axis FIS, in TD3D fit, over the previous single-axis sensor. Target data were collected for the 37-mm shell, at 55 cm depth, in both IS and FG modes. The target was moved through the same testing table, with data collected at each location. In the case of the fluxgate the surface plot shows DC field for each target position. In the case of the IS, the surface plot shows the sensor response, at one instant in time, to the EM fields generating by decaying eddy currents in the target. The IS response is shown below in Figures 7.7 and 7.8. The T_x coil #1 was used. The quality of the induction sensor data was similar to that of the single-axis data, in terms of SNR. The fluxgate data were roughly equivalent to the previous single-axis data, with slightly elevated noise.

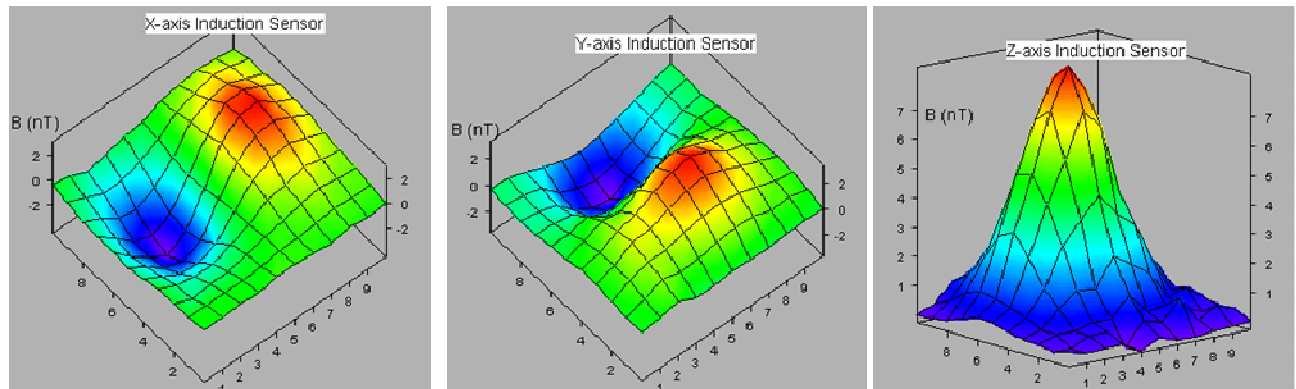


Figure 7.7 - Tri-Axial induction sensor response to 37-mm shell at depth of 55 cm aligned vertically, time gate = 300 μ s; channels x, y, and z respectively.

¹ T_x coil #1 was used for Section 7 data and T_x coil #2 with 3x larger magnetic moment was used for Section 8 data

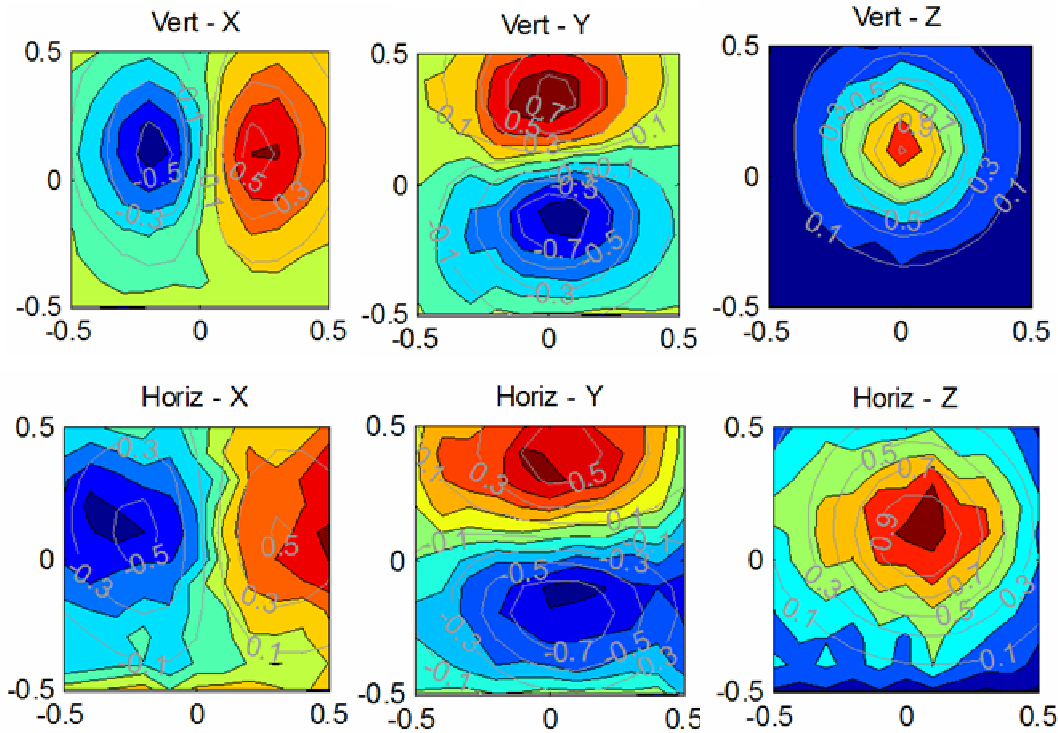


Figure 7.8 - Surface plots generated by TD3D analysis. Shown for a 37 mm shell at depth of 55 cm, aligned both vertically (top) and horizontally (bottom), time gate = 290 μ s.

The results of the TD3D modeling based on 3-component IS data are summarized in Table 12 below. The performance of the 3-axis IS was compared to that of a single vertical IS. The results can be summarized as:

- The variance reduction is good for 3-axis data and is distinctly better for the vertical orientation compared to the horizontal.
- Data quality was found to be very good early in the time decay, but is marginal, particularly in the horizontal components, by ~ 1 ms.
- *Large β and small δ in the primary axis; small β and large, symmetric δ for the orthogonal axes.*
- The inferred azimuths and inclinations are not highly accurate but fall into the correct quadrants.
- Single-axis, vertical data is of higher quality (variance reduction), but the inferred shape is tri-axial ellipsoid or an oblate spheroid (wrong!).

In section 6.1, we state that we will only use those Td3D modeling parameters to which a sensor system is sensitive. For this chapter and Chapter 8 for target discrimination, we limit modeling parameters to intermediate time in the objects analyzed, i.e., ignore α and δ parameters. However, as an example to show the δ parameter can also be used for target discrimination, we list results for δ in Table 12.

The comparison of 3-component vs. 1-component measurement demonstrates the usefulness of the 3-component measurement. The 3-axis sensor clearly recovers nearly axisymmetric cylinders

for both vertical and horizontal orientations while the single-axis vertical sensor does not recover correct shape. The 3-axis receiver gives better discrimination capability than the single z-axis receiver. Signal-to-noise ratio (SNR) could be improved with a higher moment transmitter.

Table 12 - Comparison of TD3D modeling between vertical IS and 3-axis IS.

z is the target distance below the ground with sensor at 55 cm above the ground; the azimuth of target is expressed with respect to β_1

Parameter	3C-Vert	1C-Vert	3C-Horiz	1C-Horiz
Variance Reduction	90%	97%	78%	89%
x, m	0.01	-0.02	0.01	-0.03
y, m	0.04	0.09	-0.13	0.13
z, m	-0.02	-0.02	0.21	-0.05
azimuth, deg	8	48	10	77
inclination, deg	68	75	39	104
roll	0	0	0	0
β_1	1	0.64	1	1
β_2	0.26	1	0.17	0.93
β_3	0.28	0.92	0.15	0.66
γ_1	0.95	1.07	1.74	1.75
γ_2	1.17	1.28	1.58	1.58
γ_3	1.13	1.58	1.87	1.92
δ_1	1.1	80	0	3.8
δ_2	11.6	47	31	14.6
δ_3	13.8	39	33	19.1

7.3 Receiver system performance summary

In section 7.1 and 7.2, we validate the performance of the dual-mode sensor and demonstrate the usefulness of a 3-axis sensor for EM induction measurement. The FIS has been tuned, both in hardware settings and operational parameters, to achieve desired sensitivity with minimal scan time. The operational parameters are outlined in Table 13 below. The results of the hardware tuning are:

- The system recovery time is about 150 μ s after the falling edge of the digital control pulse
- Selected R_{coil} ($= R_{\text{damp}}/2$) to balance the bandwidth and the recovery time. Figure 7.9 shows the sensor bandwidth and sensitivity versus the R_{coil}
- In induction mode, system noise spectrum is 1-2 pT/ $\sqrt{\text{Hz}}$ in the frequency band, with a total noise less than 20 pTrms in the time domain

- In fluxgate mode, the receiver has a noise of 100 pT/ $\sqrt{\text{Hz}}$ at 1 Hz, and about 1 nT RMS noise in the band of DC to 30 Hz (for single axis)
- Can detect 37-mm shell (both vertical and horizontal orientation) at a distance of 0.5 to 1m in the time window of 150 μs to 5 ms.

The resulting FIS system is also sensitive to targets smaller than 37-mm shells in the range of about 150 μs to ~ 5 ms for an EM measurement. We were able to detect a 20-mm standard shell at 31 cm below the sensor when we placed an FIS sensor in the middle of Tx coil #1.

Table 13 - Operational Parameters of FIS system

	Induction mode	Fluxgate mode
Stacking	20	1
Window Gating	10 ms	50 ms
Signal repetition rate	40 ms	1 ms
Length of measurement	0.8 s	50 ms
Low pass filter	50 kHz	30 Hz
Gain	5 mV/nT (x1, 2, 5, 10)	0.75 mV/nT
Resolution/dynamic range	16 bits, 10 V	16 bits, 10 V
DAQ Sampling rate	500 kS/s	5 kS/s

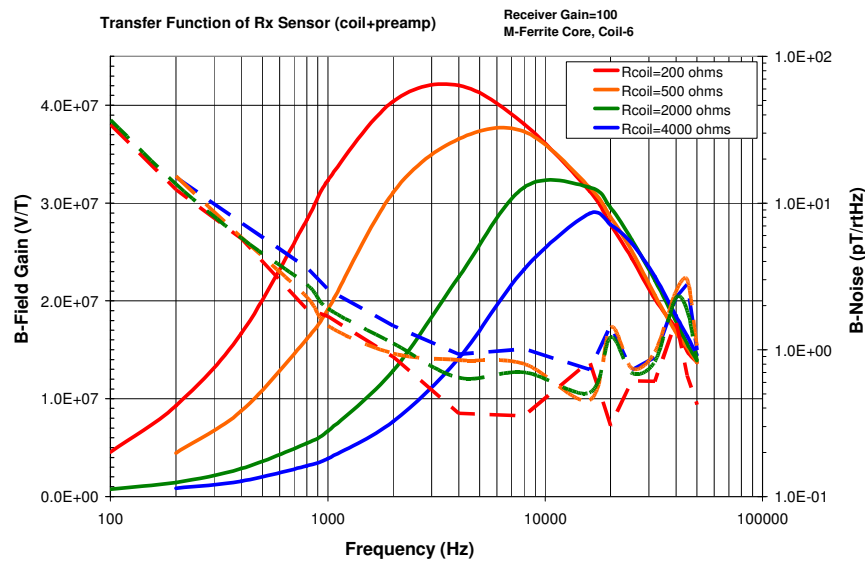


Figure 7.9 - Transfer function and noise power spectrum of IS receiver for fixed series coil resistance. For the final system, $R_{\text{coil}} = 7 \text{ kohms}$, which was optimized for the early time response. The solid curves are sensor gain, and the dashed curves show sensor noise referred to the input.

8. RESULTS AND DISCUSSION – TARGET DISCRIMINATION

To quantify the system performance, we collected extensive data for targets in different positions on the testing grid with the system in dual-mode operation. Both EM and magnetic data for three UXO targets (37 mm, 40 mm, 57 mm shells), and canonical calibration targets such as spheres, disks, and cylinders were collected in the lab and analyzed with TD3D modeling and magnetic dipole modeling.

8.1 TD3D implementation

Our TD3D implementation includes several different approaches to parameter estimation (inversion). Classical gradient-descent methods are most efficient but are susceptible to being trapped in local minima in the error surface. Genetic algorithms offer “smart” sampling of the parameter space (cf. grid searches or Monte Carlo) but can still be slow. In this exercise, we indeed found that many of the objects are characterized by relatively level error surfaces with multiple shallow local minima, leading to different trade-offs between, say, polarizability and orientation. However, we did not wish to slow down the inversions by opening up all parameters to search in the non-descent methods. The selected approach was to use numerous starting models, with different initial shapes and orientations, and to assess the aggregate result for classification (see below). Three different damping parameters to the inversion were also tested; this controls the trade off between speed and stability. Finally, models for 1, 2, and 3 independent axes were run for all objects.

8.2 Ordnance discrimination by shape classification

The approach to discrimination used here does not consider the *absolute* size of derived parameters, but rather addresses the *relative* magnitudes of different principal directions, such that an assessment of target shape might be made. Ordnance is roughly cylindrical whereas much ordnance scrap and other clutter can be crudely described as plate-like. Furthermore, the former are usually axisymmetric, whereas the latter can be any shape, i.e., tri-axial. Because the penalty for leaving UXO in the ground is greater than for digging non-UXO, the classifier should strongly weight Probability of Detection (PD = True Positives = declared ordnance is ordnance) with lower regard for the Probability of False Alarm (PFA = False Positives = declared ordnance is scrap). In the present work, this means successfully identifying as many ordnance and cylindrical test objects as cylinders and accepting a higher failure rate for misclassifying plates as cylinders. The trade-off of PD vs. PFA is a Receiver Operating Characteristic (ROC) curve. It turns out here that the ROC curve is sharply bent so we report only the optimum response, the lowest PFA at the highest PD.

Variation of some discrimination parameter determines the trade-off of PD vs. PFA and hence the values of the ROC curve. We tested the following discrimination parameters:

- β_1/β_2 . Expected to be >1 for a cylinder and <1 for a plate
- γ_1/γ_2 . Expected to be <1 for a cylinder and >1 for a plate
- Joint β_1/β_2 and γ_1/γ_2
- β_2/β_3 . Expected to be $= 1$ for a cylinder and >1 for a plate
- γ_2/γ_3 . Expected to be $= 1$ for a cylinder and <1 for a plate
- Joint β_2/β_3 and γ_2/γ_3

- β axisymmetry, defined by Grimm (2003) as $1 - (\beta_2/\beta_1 - \beta_3/\beta_1) / (\beta_2/\beta_1 + \beta_3/\beta_1)$. This parameter varies from 0 to 1 with increasing resemblance to a cylinder.

Although the expected cutoffs separating cylinders from other shapes should be unity, in practice the parameter is swept over a range of values and the numbers of correctly and incorrectly classified objects is counted (PD and PFA). With numerous starting models taken for every target, the final classification is taken by a simple majority rule.

8.3 Results

8.3.1 EM induction

Data for 36 targets were collected by FIS for analysis; the sensor was 47 cm above the test table or ground for 24 of the objects and 75 cm above for the remainder. Sphere models (all three axes constrained to equal in TD3D) have an average variance reduction (VR) of 89% (Table 14), indicating that this simple model remains a useful starting approximation to target size and position. The sphere can also be considered to represent a dipole response inline with the induced field. No discrimination was attempted on the sphere results. The sphere/dipole can also be considered a “1-axis” model.

Primary classification was performed for the 47-cm height data due to better data quality, using both 2- and 3-axis models (Table 15). Several outdoor grid data (end with “out” in target names) show slightly better data quality (higher VR). For both kinds of models, *the classifier based jointly on β_1/β_2 and γ_1/γ_2 was found to give the best results*. The optimum cutoffs were found to be close to unity, as expected. In practice $\beta_1/\beta_2 > 1.1$ and $\gamma_1/\gamma_2 < 0.9$ were required for classification as a cylinder, whereas $\beta_1/\beta_2 < 1.0$ and $\gamma_1/\gamma_2 > 1.1$ were required for classification as a disk. Results not satisfying these criteria resulted in no classification for that run. The aggregate classification² was determined by the simple majority of those cases that yielded a classification, Figures 8.1 and 8.2.

The second and third columns in Table 15 show the assigned shape and the result of the aggregate classifier, respectively. For the axisymmetric representations (2-axis) PD = 100% and PFA = 32%, i.e., all cylinders were correctly classified and 3/8 disks were misclassified as cylinders. For the triaxial representations (3-axis), PD = 93% (13/14 cylinders correct) and PFA = 50% (4/8 disks correct). It is worth noting that the 4 aluminum disks were always misclassified whereas the 4 steel disks were almost always classified correctly. This discrepancy is presumably due to the smaller induction in aluminum.

Representative fits to the data are illustrated below. Figures 8.3 – 8.5 show a cylinder at azimuth 45° and inclination 45°, whereas Figures 8.6 - 8.8 show a disk at the same attitude. Each figure displays one component of the data (Z, X, or Y). The first two sub-panels show the spatial representation of the data for the first and last time gates whereas the second two sub-panels display the time decay at fixed locations.

² Note the β_1/β_2 and γ_1/γ_2 ratios given in Table 15 cannot be used directly to assess discrimination. These are individual runs selected to show how the β and γ factors relate to shape and orientation. The classifier performance should be based on the aggregate as there are no selection biases.

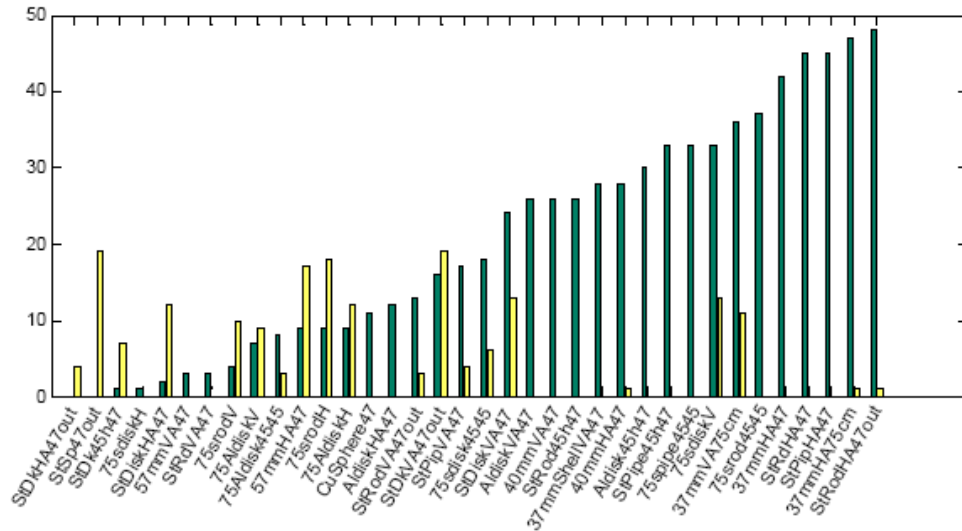


Figure 8.1 - Three-axis dipole performance of aggregate discriminator on canonical and ordnance test articles at $z = 47$ cm. Green bars are number of classifications as cylinders, yellow bars are numbers of classifications as disks. 93% of cylinders are correctly classified (PD), whereas 50% of disks are incorrectly classified (PFA).

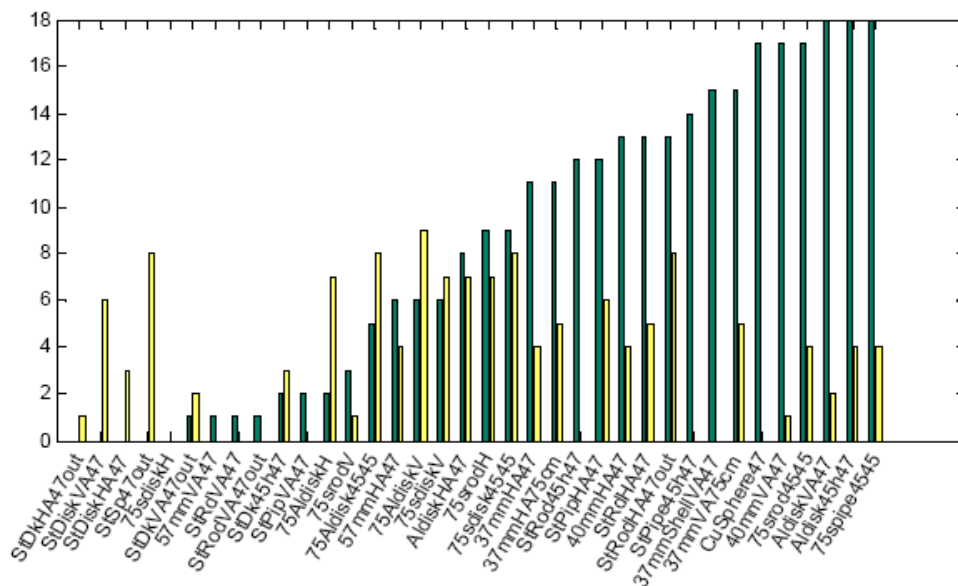


Figure 8.2 - As Fig. 8.1, but for 2-axis dipole (axisymmetry assumption). 100% of cylinders are correctly classified (PD), whereas 38% of disks are incorrectly classified (PFA).

The recovered orientations reported in Table 15 are most accurate when the object's shape is correctly classified. Azimuth refers to map direction clockwise from north, inclination is expressed up relative to the horizontal, and roll is the clockwise rotation about the principal or symmetry axis of a 3D object. However, for a body of revolution, the roll has no meaning (we set it to zero).

The classification criteria developed at 47 cm were also applied to the 75 cm data. Results were poor, with PD = 0-30% and PFA = 33-66%. This reflects the lower data quality at 75 cm. This is limited by the sensitivity of the induction coil which can be improved by using a better coil or a coil array.

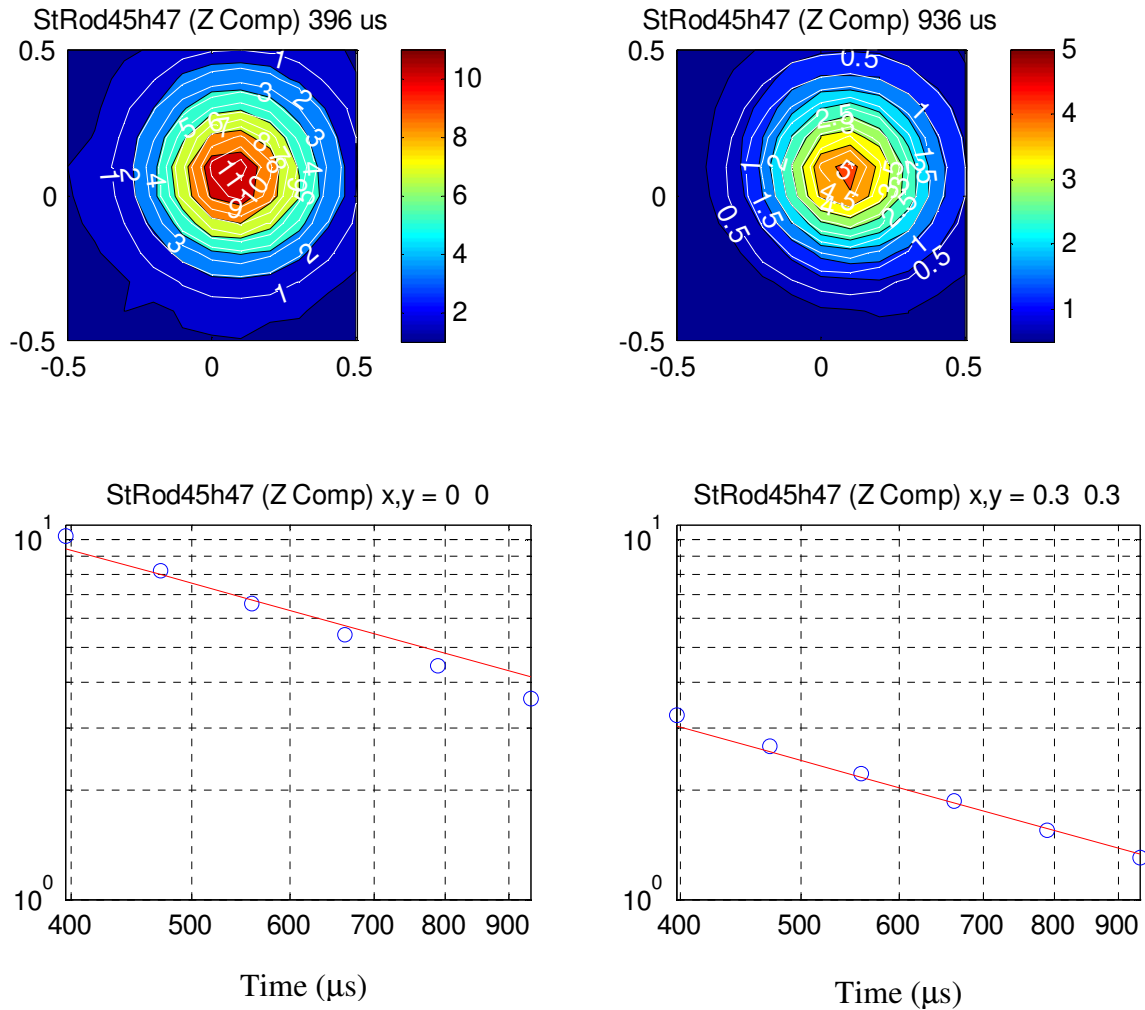


Figure 8.3 - Z component, steel rod at azimuth 45 inclination 45. Data values are multiplied by 1000 for clarity. Upper panels show spatial pattern of data (color) and model fit (white contours). Bottom panels compare time decay of model (red line) vs. data (blue circles).

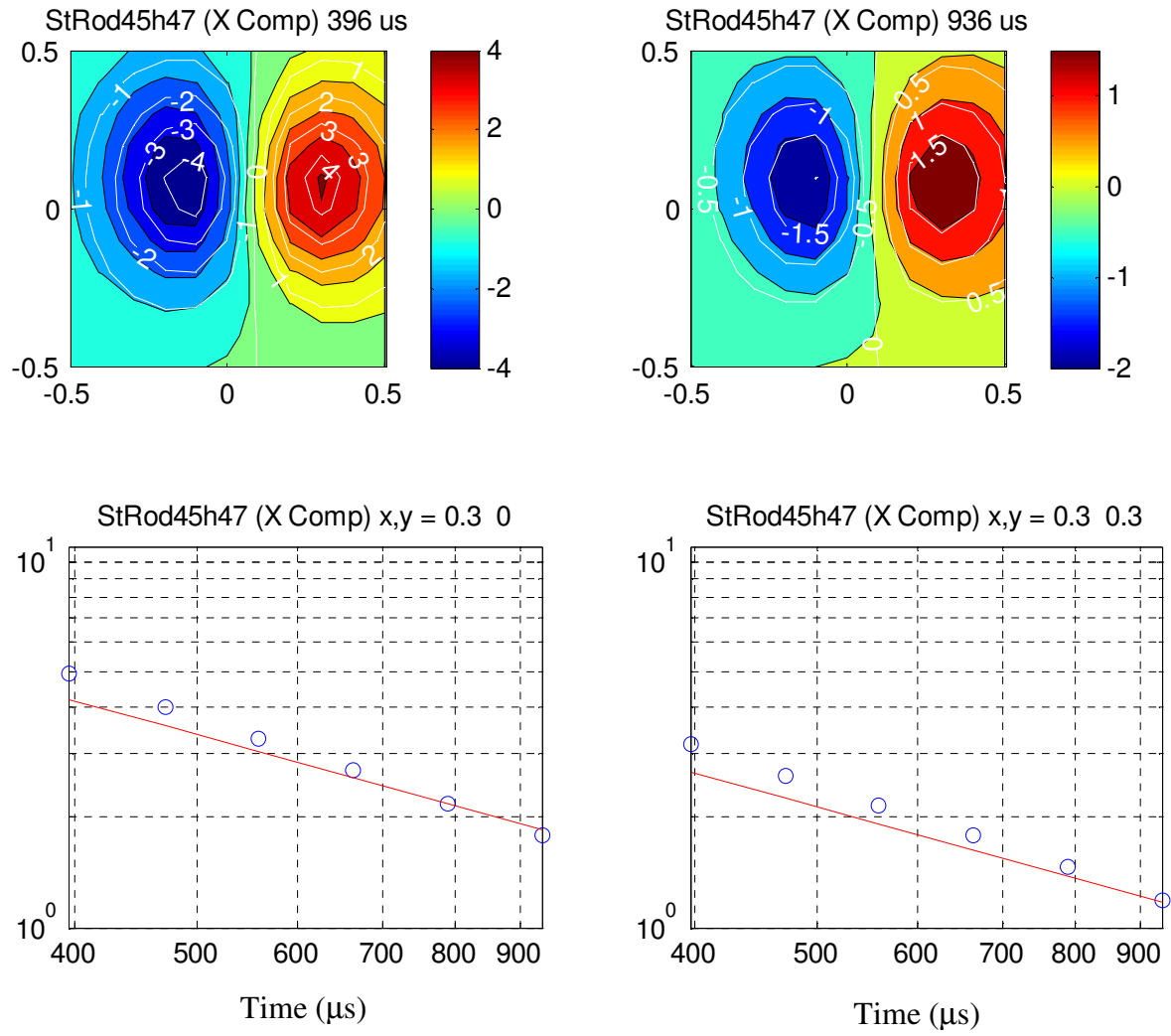


Figure 8.4 - X-component of same rod.

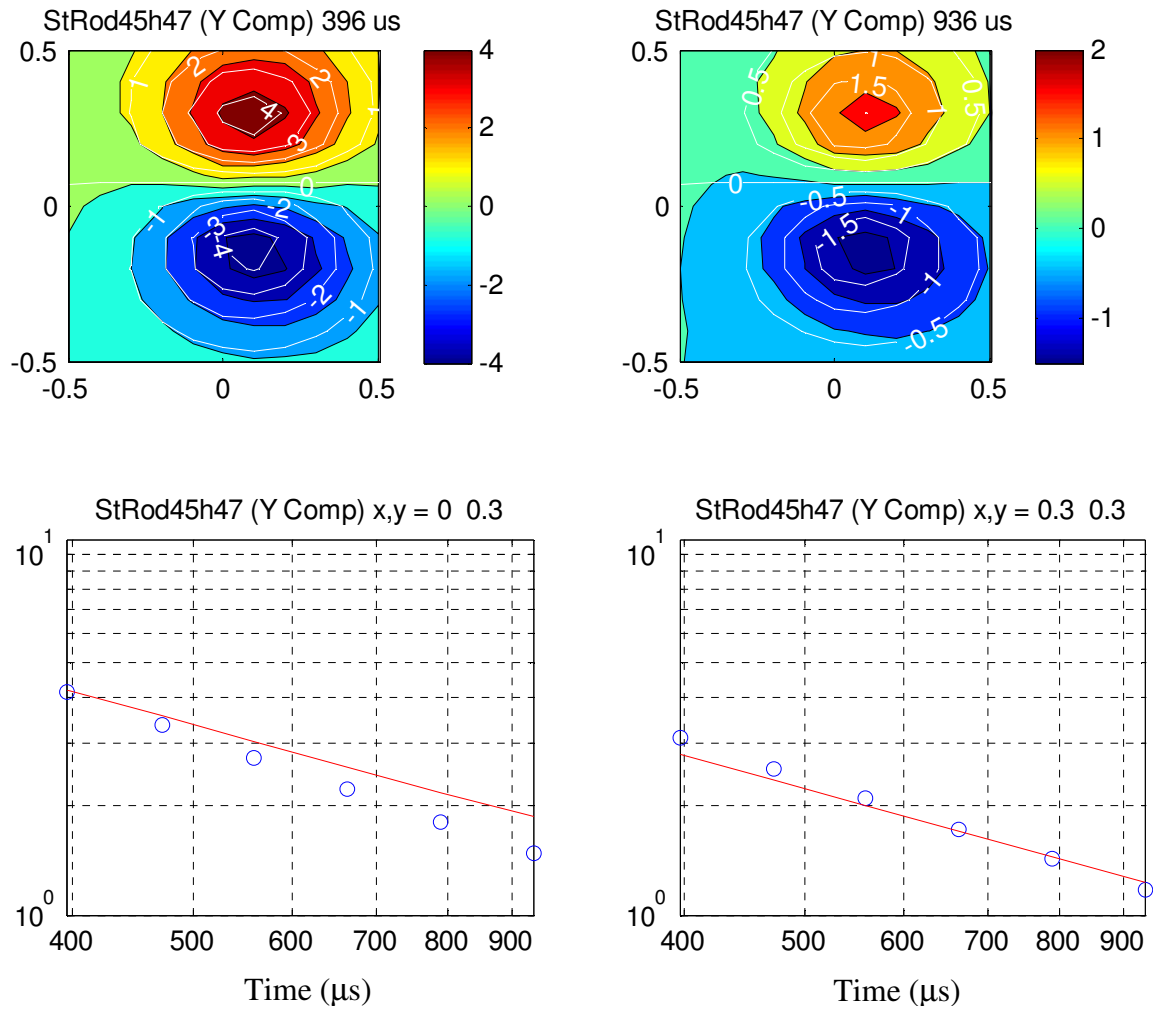


Figure 8.5 - Y-component of same rod.

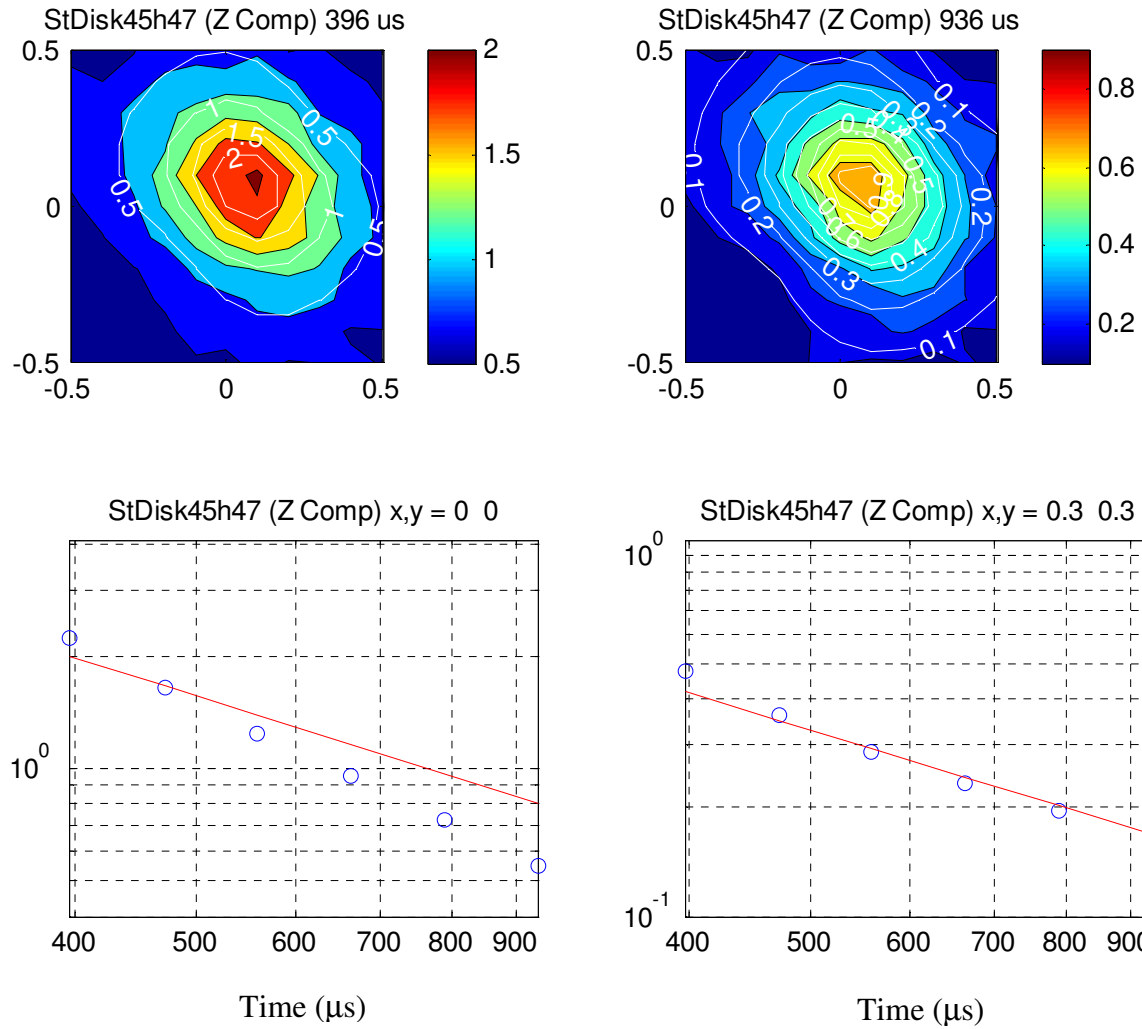


Figure 8.6 - As Figure 8.3, but for Z-component of circular steel disk at azimuth 45° inclination 45°.

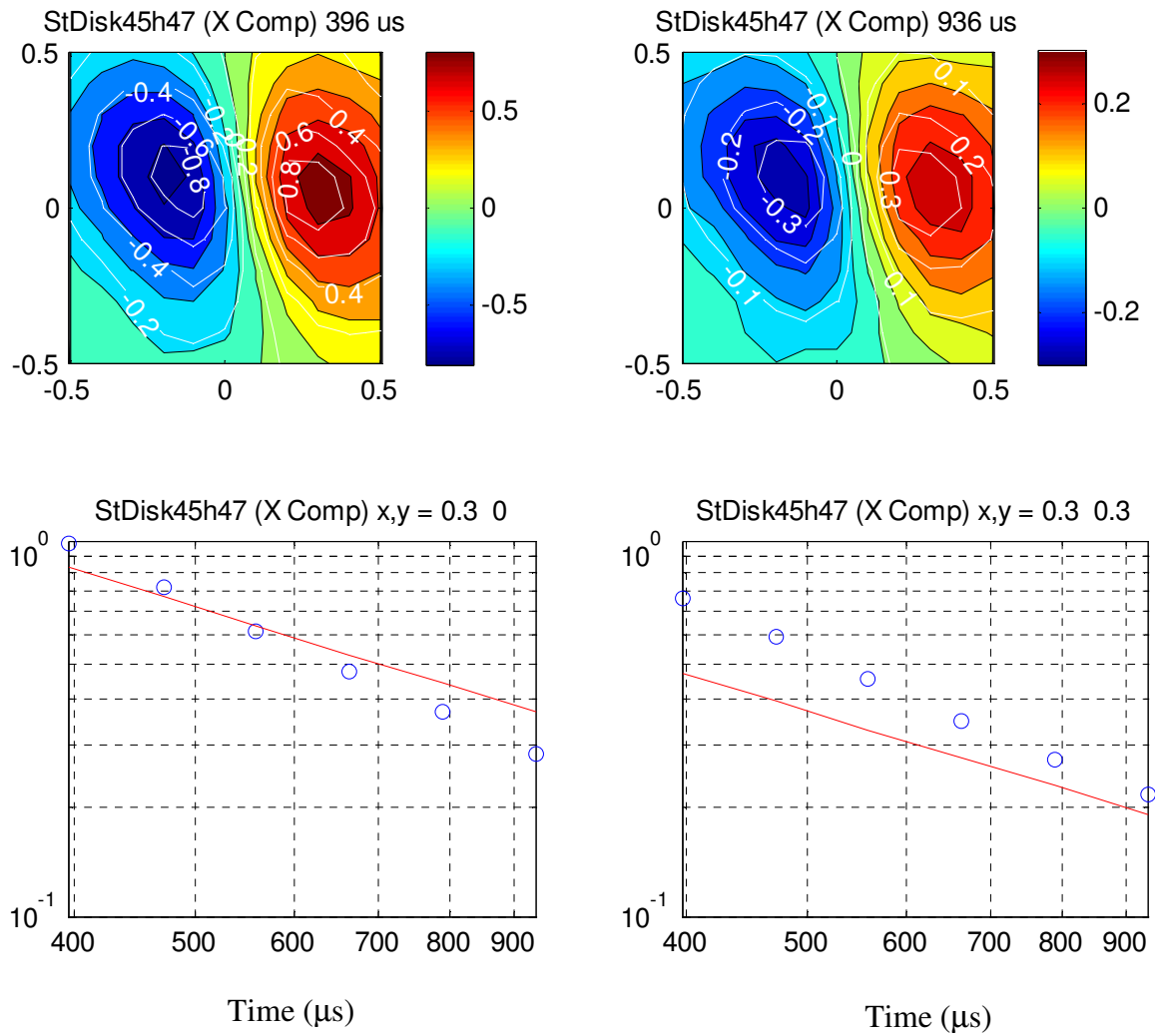


Figure 8.7 - X-component of disk.

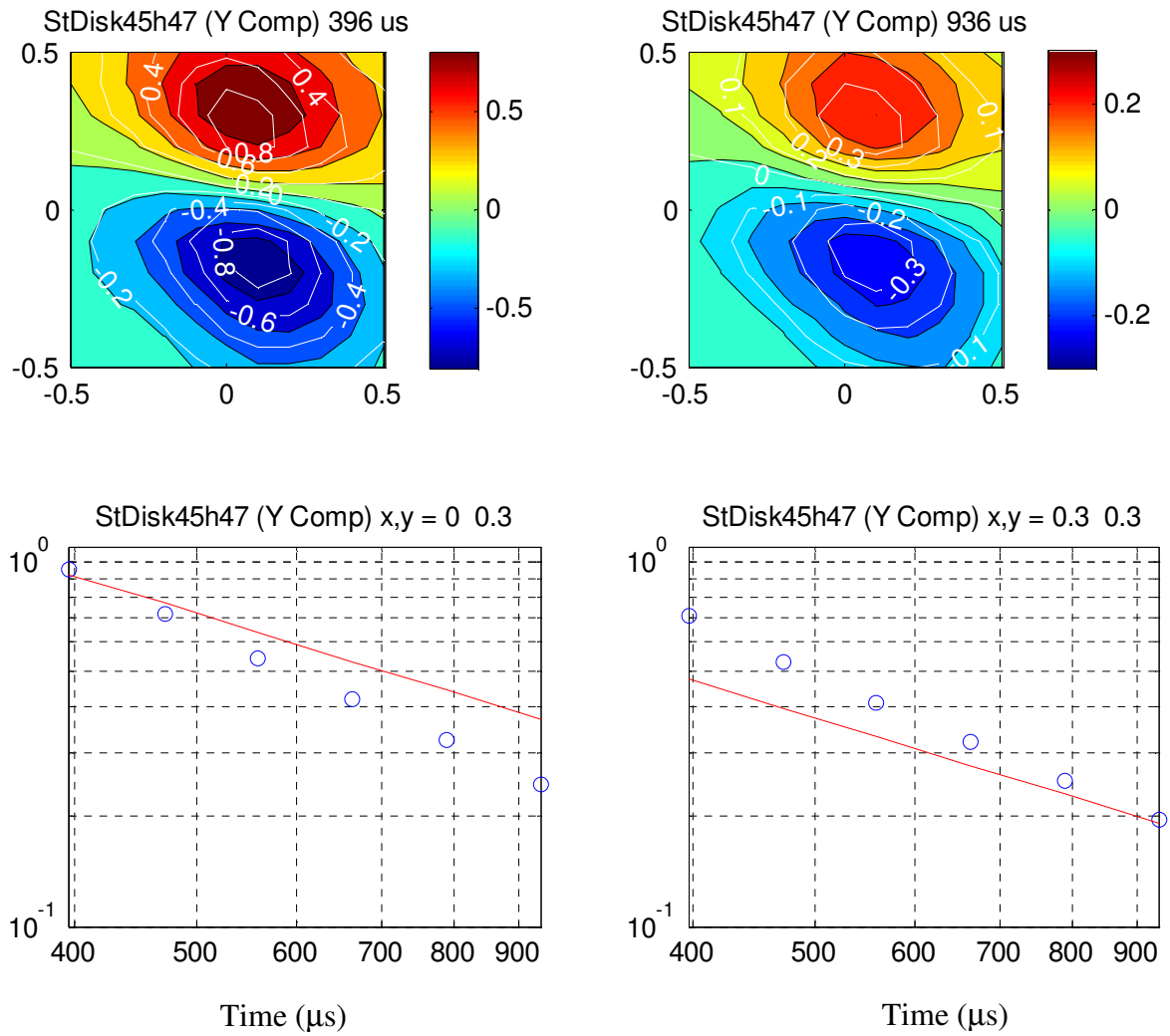


Figure 8.8 - Y-component of disk.

Table 14 - Single-axis (sphere) fits for 47-cm and 75-cm height data

(Target is named as “target_orientation_distance”, with Al - Aluminum, St – Steel, HA- Horizontal, VA-Vertical, sensor distance to the testing table is 47 or 75 cm). Files labeled “out” were collected on test grid outdoors

Target	Damp*	VR	X	Y	Z	β_1	γ_1
Aldisk_HA_47	0.01	83.3	-0.02	0.01	-0.05	7922	1.12
StDisk_HA_47	0.01	94.5	0.00	0.01	-0.11	9755	1.01
StDisk_HA_47out	0.01	94.6	0.01	0.01	-0.11	9947	1.01
Aldisk_VA_47	0.01	95.5	0.00	0.01	-0.07	8827	1.06
StDisk_VA_47	0.01	78.4	0.02	0.01	0.07	9577	1.04
StDisk_VA_47out	0.01	81.8	0.01	0.01	0.06	9483	1.04
StDisk_4545_47	0.01	92.0	0.07	0.07	-0.10	8951	1.07
Aldisk_4545_47	0.01	93.1	-0.07	-0.06	-0.11	8074	1.10
StSphere_47out	0.01	81.0	0.01	0.02	-0.13	10950	0.94
CuSphere_47	0.01	97.5	0.01	0.01	-0.10	12590	0.89
37mm_HA_47	0.01	73.1	-0.02	0.01	-0.01	8330	1.09
37mm_VA_47	0.01	97.8	0.00	0.01	-0.13	9665	1.01
40mm_HA_47	0.01	83.0	0.01	0.02	-0.01	9555	1.03
40mm_VA_47	0.01	98.0	0.00	0.01	-0.13	11000	0.96
57mm_HA_47	0.01	90.2	0.01	0.01	-0.07	10190	0.98
57mm_VA_47	0.01	97.7	0.00	0.01	-0.14	12380	0.90
StRod_HA_47	0.01	72.3	-0.01	0.01	0.00	11030	0.95
StRod_HA_47out	0.01	73.4	-0.01	0.01	-0.01	11210	0.95
StRod_VA_47	0.01	97.4	0.00	0.01	-0.15	13260	0.87
StRod_VA_47out	0.01	97.8	0.00	0.01	-0.15	13690	0.87
StRod_4545_47	0.01	96.4	0.08	0.08	-0.13	11950	0.91
StPipe_HA_47	0.01	73.2	0.01	0.01	0.00	11010	0.95
StPipe_VA_47	0.01	97.9	0.00	0.01	-0.15	13020	0.87
StPipe_4545_47	0.01	96.4	0.09	0.07	-0.14	12170	0.92
37mm_HA_75	0.01	7.8	-0.44	0.07	-0.26	6912	1.18
37mm_VA_75	0.01	13.7	-0.06	-0.06	-0.38	5502	1.24
StPipe_4545_75	0.01	63.1	0.10	0.12	-0.32	8365	1.08
StRod_4545_75	0.01	63.0	0.10	0.12	-0.35	7958	1.11
StRod_HA_75	0.01	5.5	0.06	-0.01	-0.21	6624	1.18
StRod_VA_75	0.01	81.7	-0.01	-0.01	-0.29	10320	0.97
Aldisk_HA_75	0.01	11.1	-0.28	0.10	-0.23	8523	1.17
Aldisk_VA_75	0.01	16.1	0.04	-0.15	-0.11	10070	1.04
Aldisk_4545_75	0.01	13.3	-0.29	0.04	-0.02	11260	0.98
StDisk_HA_75	0.01	0.0	0.23	-0.12	-0.50	1518	1.91
StDisk_VA_75	0.01	13.2	-0.07	-0.03	-0.41	5450	1.29
StDisk_4545_75	0.01	11.5	0.10	0.15	-0.35	5768	1.26

* a damping parameter controls the stability of the inversion for the conjugate gradient (CG) and generalized inverse (GI). In either case, a higher value will cause the inversion to converge more slowly, but with less likelihood of taking too large a step in the wrong direction and getting lost.

Table 15 - Two- and three-axis fits, classification, and representative inversion results (VR, position X, Y, Z of the target in meter, rotations in degree, and shape parameters)

Target	True Shape	Correct Classification?	VR	X	Y	Z	Azimuth	Inclin ation	Roll	β_1	β_2	β_3	γ_1	γ_2	γ_3	β_1/β_2	β_1/β_3	γ_1/γ_2	γ_1/γ_3
2-Axis Fits																			
37mm_HA_47	Cyl	Yes	86.2	-0.03	0.01	-0.15	90	0	0	24560	3405	3405	1.2	1.2	1.2	7.2	7.2	1.0	1.0
37mm_VA_47	Cyl	Yes	99.0	0.00	0.01	0.00	6	90	0	28050	4119	4119	1.0	1.1	1.1	6.8	6.8	0.9	0.9
40mm_HA_47	Cyl	Yes	92.4	0.01	0.02	-0.14	90	0	0	11860	7590	7590	1.1	1.2	1.2	1.6	1.6	0.9	0.9
40mm_VA_47	Cyl	Yes	99.1	0.01	0.01	-0.01	111	94	0	28460	4438	4438	0.9	1.1	1.1	6.4	6.4	0.9	0.9
57mm_HA_47	Cyl	Yes	93.7	0.00	0.01	-0.14	90	2	0	13050	10440	10440	1.0	1.1	1.1	1.3	1.3	0.9	0.9
57mm_VA_47	Cyl	Yes	98.9	0.00	0.01	-0.03	94	88	0	71290	12830	12830	1.0	1.1	1.1	5.6	5.6	0.9	0.9
Aldisk_4545_47	Plate	No	92.1	-0.06	-0.05	-0.05	49	7	0	509	26290	26290	1.1	1.2	1.2	0.0	0.0	0.9	0.9
Aldisk_HA_47	Plate	No	88.4	-0.02	-0.01	0.03	5	-7	0	488	26280	26280	1.1	1.2	1.2	0.0	0.0	0.9	0.9
Aldisk_VA_47	Plate	No	95.2	0.00	0.01	0.00	80	-3	0	471	16230	16230	1.2	1.1	1.1	0.0	0.0	1.1	1.1
CuSphere47	Sphere	N/A	97.5	0.01	0.01	-0.09	84	0	0	12450	12830	12830	0.9	0.9	0.9	1.0	1.0	1.0	1.0
StDisk_HA_47	Plate	Yes	95.7	-0.02	0.01	-0.07	91	-9	0	7784	10690	10690	1.1	1.0	1.0	0.7	0.7	1.2	1.2
StDisk_VA_47	Plate	Yes	85.9	0.04	0.02	-0.23	74	89	0	4525	11760	11760	1.5	1.3	1.3	0.4	0.4	1.2	1.2
StDisk_4545_47	Plate	Yes	93.9	0.05	0.05	-0.05	47	-10	0	6578	9999	9999	1.3	1.0	1.0	0.7	0.7	1.3	1.3
StDisk_HA_47out	Plate	Yes	95.4	0.01	0.01	-0.08	359	1	0	8365	10530	10530	1.1	1.0	1.0	0.8	0.8	1.1	1.1
StDk_VA_47out	Plate	Yes	90.4	0.00	0.01	-0.24	102	90	0	4900	11050	11050	1.6	1.3	1.3	0.4	0.4	1.2	1.2
StPipe_4545_47	Cyl	Yes	98.2	0.04	0.04	-0.03	52	71	0	40270	5150	5150	0.9	1.0	1.0	7.8	7.8	0.9	0.9
StPipe_HA_47	Cyl	Yes	91.2	-0.01	0.01	-0.16	89	1	0	11530	6890	6890	0.9	1.2	1.2	1.7	1.7	0.8	0.8
StPipe_VA_47	Cyl	Yes	98.4	0.00	0.01	-0.08	356	91	0	15550	11940	11940	0.8	0.9	0.9	1.3	1.3	0.8	0.8
StRod_HA_47	Cyl	Yes	90.7	0.00	0.01	-0.16	89	0	0	14510	8346	8346	1.0	1.2	1.2	1.7	1.7	0.8	0.8
StRod_VA_47	Cyl	Yes	99.0	0.00	0.01	-0.05	97	91	0	78930	13280	13280	1.0	1.0	1.0	5.9	5.9	1.0	1.0
StRod_4545_47	Cyl	Yes	98.2	0.04	0.05	-0.02	56	73	0	37130	5853	5853	0.9	1.2	1.2	6.3	6.3	0.8	0.8
StRod_HA_47out	Cyl	Yes	90.9	0.00	0.01	-0.17	90	0	0	14460	7909	7909	1.0	1.2	1.2	1.8	1.8	0.8	0.8
StRod_VA_47out	Cyl	Yes	99.1	0.00	0.01	-0.05	115	90	0	53830	9656	9656	0.9	1.0	1.0	5.6	5.6	1.0	1.0
StSp47out	Sphere	N/A	83.0	0.01	0.02	-0.21	4	90	0	13010	15370	15370	1.1	1.0	1.0	0.8	0.8	1.1	1.1

Target	True Shape	Correct Classification?	VR	X	Y	Z	Azimuth	Inclin ation	Roll	β_1	β_2	β_3	γ_1	γ_2	γ_3	β_1/β_2	β_1/β_3	γ_1/γ_2	γ_1/γ_3
3-Axis Fits																			
37mm_HA_47	Cyl	Yes	86.8	-0.03	0.01	-0.10	90	0	0	28280	18500	476	1.2	1.4	1.2	1.5	59.4	0.9	1.0
37mm_VA_47	Cyl	Yes	99.1	-0.02	0.02	-0.02	118	82	0	11170	8076	7501	0.9	1.1	1.1	1.4	1.5	0.8	0.8
40mm_HA_47	Cyl	Yes	92.5	0.01	0.01	-0.18	90	0	0	10360	6845	6034	1.1	1.2	1.3	1.5	1.7	0.9	0.8
40mm_VA_47	Cyl	Yes	99.2	0.01	0.02	-0.02	254	85	0	12960	8860	8716	0.8	1.1	1.1	1.5	1.5	0.8	0.8
57mm_HA_47	Cyl	No	94.1	0.00	0.01	-0.21	308	89	0	7003	9535	10210	1.2	1.1	1.0	0.7	0.7	1.1	1.2
57mm_VA_47	Cyl	Yes	98.7	0.00	0.01	-0.05	97	88	0	54960	28690	1797	1.0	1.1	0.7	1.9	30.6	0.9	1.5
Aldisk_4545_47	Plate	No	95.9	0.02	-0.03	0.01	68	120	0	3893	6615	7047	0.8	1.2	1.2	0.6	0.6	0.6	0.6
Aldisk_HA_47	Plate	No	90.1	-0.02	0.00	-0.20	95	0	0	8253	6229	5071	1.1	1.2	1.4	1.3	1.6	0.9	0.8
Aldisk_HA_47	Plate	No	65.5	-0.02	0.00	-0.08	52	95	0	21990	5683	2789	1.3	1.0	1.3	3.9	7.9	1.4	1.0
CuSphere47	Sphere	N/A	98.0	0.01	0.02	0.01	314	90	0	15510	11450	10540	0.7	0.9	1.0	1.4	1.5	0.8	0.8
StDisk_HA_47	Plate	Yes	95.6	0.00	0.02	-0.07	270	0	0	7672	10440	10640	1.1	1.0	1.0	0.7	0.7	1.2	1.2
StDisk_VA_47	Plate	No	85.9	0.04	0.02	-0.23	73	89	0	3769	7588	7842	1.5	1.2	1.2	0.5	0.5	1.2	1.3
StDisk_45h_47	Plate	Yes	93.9	0.05	0.07	-0.08	47	-7	0	6382	8698	10350	1.2	1.0	1.0	0.7	0.6	1.2	1.2
StDisk_HA_47out	Plate	Yes	95.4	0.00	0.01	-0.08	179	0	0	8364	10380	11110	1.1	1.0	1.0	0.8	0.8	1.1	1.1
StDisk_VA_47out	Plate	Yes	90.2	0.00	0.00	-0.24	360	90	0	3491	8317	8487	1.5	1.2	1.2	0.4	0.4	1.2	1.2
StPipe_4545_47	Cyl	Yes	98.2	0.04	0.03	-0.03	227	-69	0	42990	27070	1006	0.9	1.2	0.8	1.6	42.7	0.8	1.1
StPipe_HA_47	Cyl	Yes	92.1	-0.01	0.01	-0.12	89	1	0	41330	23070	630	1.1	1.3	1.1	1.8	65.6	0.9	1.0
StPipe_VA_47	Cyl	Yes	99.2	-0.01	0.01	-0.06	108	87	0	58960	32820	2123	1.0	1.1	0.7	1.8	27.8	0.9	1.5
StRod_HA_47	Cyl	Yes	91.3	0.00	0.01	-0.12	89	0	0	39740	22830	625	1.1	1.3	1.1	1.7	63.6	0.9	1.0
StRod_VA_47	Cyl	Yes	98.9	0.00	0.01	-0.06	43	91	0	65810	9028	7148	1.0	0.9	0.8	7.3	9.2	1.1	1.2
StRod_4545_47	Cyl	Yes	98.2	0.03	0.05	-0.02	58	70	0	40850	26970	931	0.9	1.2	0.8	1.5	43.9	0.7	1.2
StRod_HA_47out	Cyl	Yes	91.4	0.00	0.01	-0.13	270	0	0	41230	23320	644	1.1	1.3	1.1	1.8	64.1	0.9	1.0
StRod_VA_47out	Cyl	Yes	99.1	0.01	0.01	-0.06	225	88	0	58660	33350	1965	1.0	1.1	0.7	1.8	29.9	0.9	1.5
StSp47out	Sphere	N/A	82.4	0.01	0.02	-0.21	58	90	0	10510	12290	12450	1.1	1.0	1.0	0.9	0.8	1.1	1.1

8.3.2 DC magnetometry

Four magnetometry data sets were collected for analysis: a vertical steel rod, a horizontal steel rod, a vertical steel pipe, and a steel cylinder. The sensor was 75 cm above the measurement table in all cases.³ High-quality results were obtained from the two vertical cylinders, a mediocre result from the horizontal pipe, and no result from the sphere (Table 16). Figures 8.9 - 8.11 show the useable fits.

The two vertical cylinders were first fit to a sphere model, in which the three orthogonal dipoles are held equal. The source-field direction and magnitude are held fixed. This approach is equivalent to solving for a single polarizability aligned with the source field. It does not include remanent magnetism.

The sphere fits to the vertical cylinders using all three components of the fluxgate are excellent. The lateral positions are close but not exact and the small discrepancy in the vertical coordinates reflects the finite sizes of the targets. Note, however, that nearly identical results can be obtained using the z-component only; there is little extra information added by the x and y components.

The vertical cylinders were then modeled as vertical dipoles. In principle, an axisymmetric model could have been used with the azimuth and inclination as free parameters, but time constraints and the expectation of a poor result led to this more direct test of a model that should nearly exactly fit the data. The goodness-of-fit (variance reduction, VR) did increase slightly in both cases and the x-location misfit was reduced.

The sphere fit to the horizontal rod was significantly worse but still approximately finds the target depth and size (polarizability). The horizontal misfit is not much bigger than that of the vertical cylinders and is still in the range that would be acceptable for field recovery.

Therefore the very high quality of the sphere fits and the relatively accurate locations, including depth, suggest that simple magnetization models of vertical or total-field data are capturing the vast majority of the data structure. Recent multi-axis magnetic modeling (Billings, 2004) rely on extensive prior knowledge to train magnetometry discriminators; we recommend that discrimination efforts should remain focused on induction sensing and magnetometry restricted to simple detection of deep targets.

³ Note that the sensor height is subtracted out of the induction results but not from the fluxgate results.

Table 16 - Model fit based on measured magnetic data

Target	Model	Comps Fit	X, m	Y, m	Z, m	$P^* \times 10^{-3}$	VR
Vert Steel Rod	Sphere	xyz	0.14	0.0	0.70	3.1	98.3%
Vert Steel Rod	Sphere	z	0.14	0.02	0.73	3.3	99.4%
Vert Steel Rod	Vert Dipole	xyz	0.01	-0.02	-0.69	3.1	99.4%
Vert Steel Rod	Vert Dipole	z	0.01	-0.02	-0.71	3.3	99.9%
Vert Steel Pipe	Sphere	xyz	0.17	0.01	0.63	1.7	96.0%
Vert Steel Pipe	Sphere	z	0.16	0.03	0.64	1.8	97.4%
Vert Steel Pipe	Vert Dipole	xyz	0.04	-0.01	0.61	1.7	96.8%
Vert Steel Pipe	Vert Dipole	z	0.03	0.00	0.63	1.9	98.1%
Horiz Steel Pipe	Sphere	xyz	0.18	-0.48	0.73	1.3	73.7%
Horiz Steel Pipe	Sphere	z	0.16	-0.43	0.61	0.8	76.9%

* P is the magnetic dipole moment divided by the background field

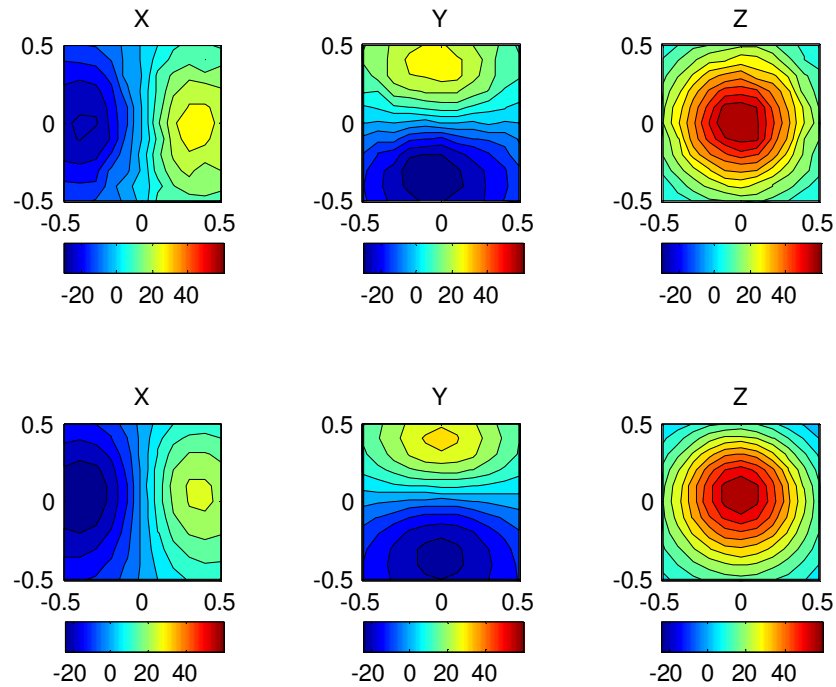


Figure 8.9 - Three-component fluxgate (DC magnetic) data (top row) and sphere model fit (bottom row) to a vertical steel rod.

Model fit to Z-component alone not only results in 99% variance reduction in Z but variance reduction using all three components is indistinguishable from actual three-component fit (98%). Horizontal components therefore do not add to model quality here.

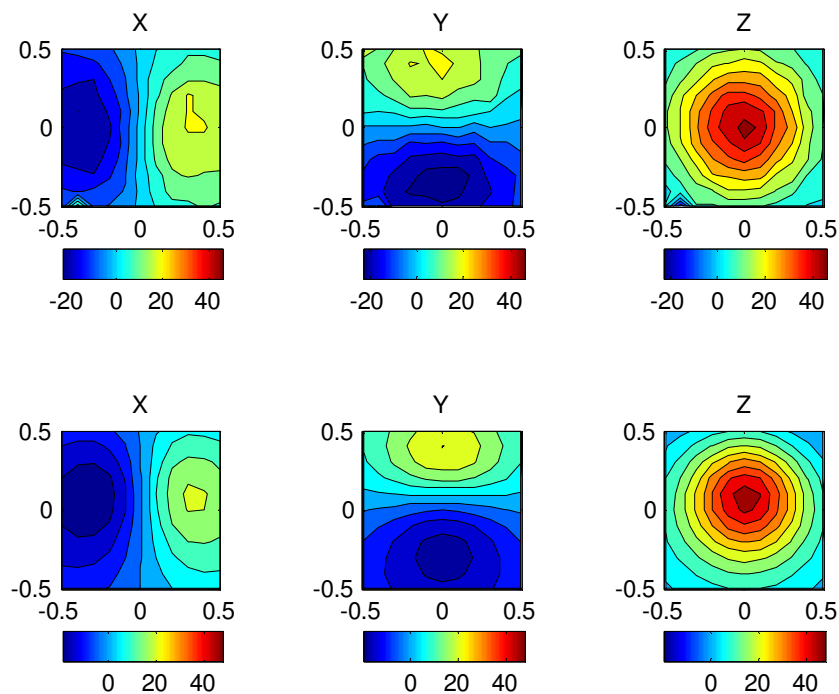


Figure 8.10 - As Fig. 8.9, but for vertical steel pipe. Sphere fit is also to Z-component alone and results in 97% variance reduction in that component and 96% in all three components; cf. 96% variance reduction using all 3 components.

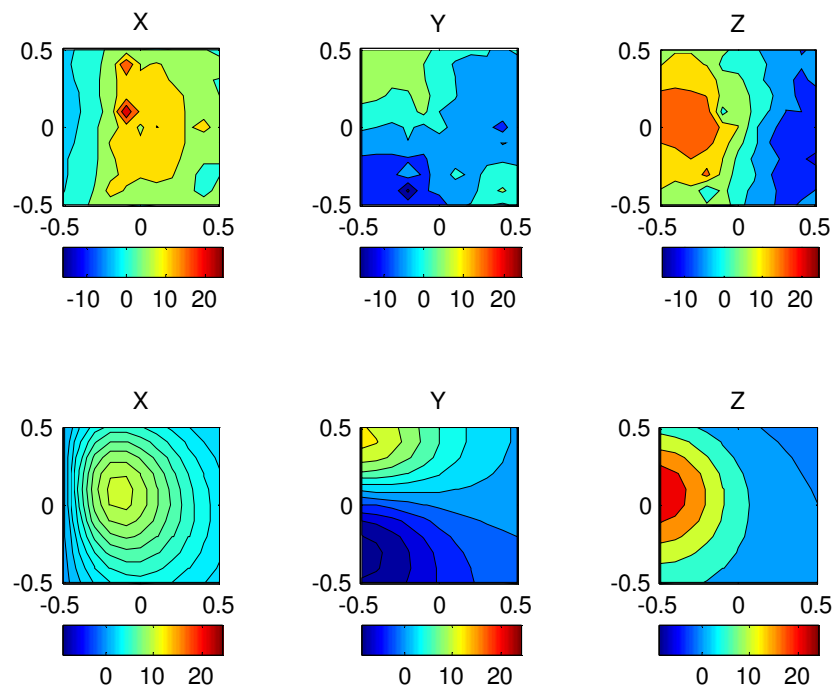


Figure 8.11 - As Fig. 8.9, but for horizontal steel rod. Fit is worse than in previous examples but still useful.

8.4 Concluding discussion on FIS data

The discrimination performance of the FIS in induction mode in these indoor experiments was comparable to that achieved by *Grimm* (2003) using the EM-61-3D at the Blossom Point test grid (PD = 91%, PFA = 32% for 3-axis models). Although the mean sensor-target vertical distance at Blossom Point was somewhat larger (60 cm) than for the objects used here, the targets were larger, giving larger signals. However, the poor performance shown in the FIS data at 75-cm separation suggests that the large secondary coil area of the EM-61-3D may be a key factor in acquiring spatially averaged, robust EM data. A spatial array may be more useful for any follow-on study or demonstration (*Grimm and Sprott, 2002*). In the fluxgate mode, the data gives very high quality of the sphere fits and relatively accurate target positions, suggest that a single vertical sensor can capture the vast majority of the data structure. Nonetheless, the FIS data has demonstrated that a fluxgate and induction sensor may be combined in a single package and yield useful information on detection of deep targets and discrimination of shallow ones.

9. RESULTS AND DISCUSSION - FIELD DEPLOYMENT STUDIES

Following the completion of indoor and outdoor data collection, QFS studied operational issues with the FIS. These operational studies were intended to improve the performance of the current FIS design, as well as inform the design of the next generation FIS. Specifically QFS

- Studied the potential reduction in background drift through installation of a current monitor
- Reconfigured the system for true outdoor operation
- Modeled the spatial resolution of the FIS for scan-in-motion operation
- Studied environmental effects: variation in the environmental background based on solar heating, time of day, location, and soil moisture content. Also, potential effects due to proximity with the ground.
- Studied the effects of motion on FIS performance

9.1 Current monitor and background drift

The FIS employs high permeability ferrite rods in the receiver coil. During the Tx pulse of the IS, eddy currents and magnetic ringing are induced in these rods. The ringing/eddy currents constitute a background signal in IS, which is digitally removed. Accurate background subtraction relies on a stable background.

During indoor data collection the IS background drift was sometimes an issue. This was believed to be due to voltage/current droop in the Tx batteries. QFS tested the effectiveness of a self-monitoring current sensor in the IS. A current monitor was installed on the Tx driver to study how the change in background correlated to change in the battery performance. QFS measured the IS background of the z-axis sensor, at a single time gate (500 μ s) in the acquisition window, over the period of 20 minutes. Simultaneously, the current to ground in the Tx driver, 500 μ s into the Tx pulse, was monitored, shown in Figure 9.1 below. The IS was run similar to dual-mode operation, with 10 ms Tx pulses, 10 ms acquisition windows, and 10 averages, with 0.5 s of dead time between scans. Some noise is seen on both the current and the IS BG curves; however a smoothing of both plots shows a similar trend in each. As the transmitter current drops, so does

the IS background. Taking the ratio of the smoothed BG and the smoothed current monitor data yields a fairly constant ratio of $\sim 6.2 \times 10^{-3}$, Figure 9.2. It is evident that the IS background does not stabilize until ~ 900 s (~ 15 minutes), while the ratio is relatively constant in less than 200 s (~ 3 min). The next-phase system will certainly need to employ a current monitor on the transmitter for improved stability.

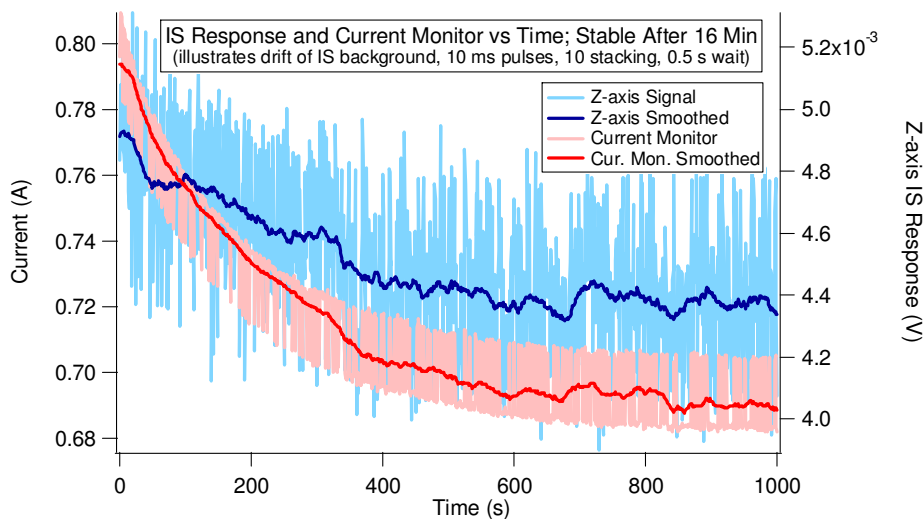


Figure 9.1 - Plot of IS background (during acquisition) and IS transmitter current (during Tx pulse) as a function of time (and scans).

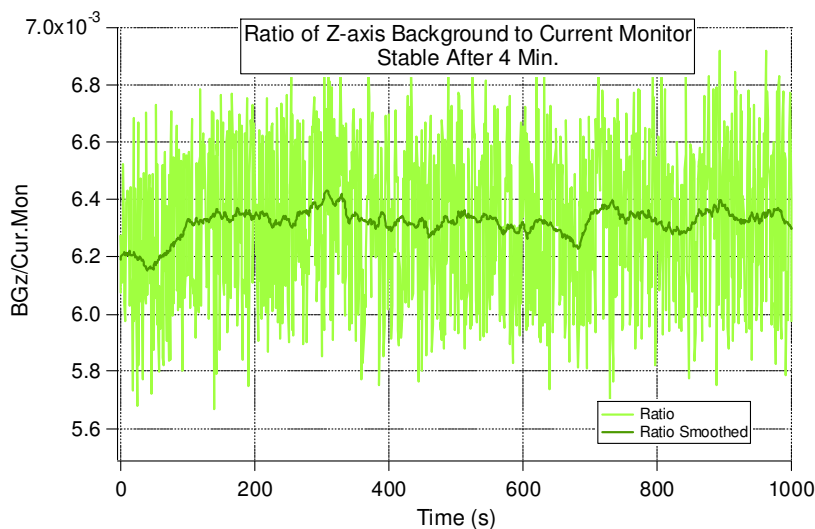


Figure 9.2 - Ratio of IS background (during acquisition) to IS transmitter current (during Tx pulse) as a function of time (and scans).

9.2 Develop system for outdoor operation

The FIS was partially configured for outdoor operation during Year 4. The prototype system had to be modified in several ways, to facilitate outdoor operation; 1) the DAQ needed to be made mobile, and 2) the system needed to be configured to run on battery power.

The prototype system used for Year 1 to Year 3 was a National Instruments DAQ in a desktop PC (NI-6251). The NI-6251 had 16 analog inputs, 2 analog outputs, and acquired 16-bit data at 1.2 MS/s. QFS purchased a new data acquisition system, the NI USB-6259. The new DAQ is DC powered and can be interfaced with a laptop via USB. It is a 16-bit, 1.2 MS/s system, with 16 analog inputs and 4 analog outputs. QFS ported the FIS LabVIEW software to run the new DAQ and test the sensor performance on the indoor test grid. The DAQ performed adequately.

QFS also configured the system to run on battery power. The Tx driver was already powered by two 12 V car batteries, but the DAQ and Dual Mode Rx were reconfigured to run off batteries as well; a 24 V and a bipolar ± 12 V supply respectively.

The prototype system was mounted on a plastic cart with non-metallic wheel for outdoor and mobile data collection. All batteries and the DAQ were mounted atop the cart, with the Tx/Rx coils on the bottom, Figure 9.3. SNR for the receiver was improved when the system was moved from the lab to outdoor, due to the large quantities of metal present indoor.

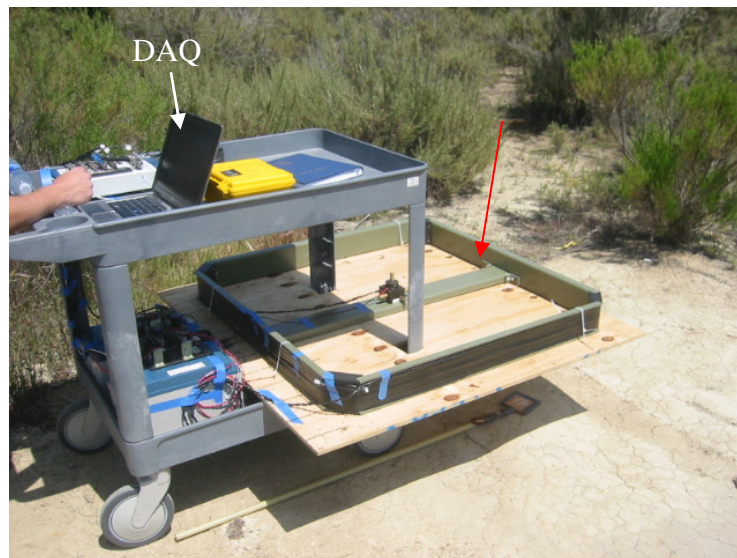


Figure 9.3 - FIS mounted on plastic cart with plastic wheels for outdoor and mobile data collection. The new DAQ is used for data collection.

9.3 Spatial resolution of scan-in-motion operation

The next phase system will favor quick operation to maximize spatial resolution. The spatial

resolution “R” (in meters) that the system will achieve is given by $R = \frac{v * t_s}{n}$, where v is the

moving speed of the system, t_s is the total scan time, and n is the number of sensors in line with the target. The proposed ESTCP follow-on system would employ 4 FIS sensors inside the Tx

halo, ensuring 2 sensors in line with the target. QFS' experience indicates that 0.5 m/s is a reasonable speed for a person to continuously push a sensor cart. The current FIS, in dual mode, takes 20 averages of a 40 ms pulse train in IS mode followed by 200 ms of FG mode, for a total scan time of 1 s. Plugging these variables into the resolution equation yields a spatial resolution of 0.25 m. The IS averaging could be reduced to 10 and the FG scan time could be reduced to 100 ms, which would result in a two-fold increase in spatial resolution to 0.125 m.

It may be desirable to increase spatial resolution further. To this end, QFS experimented with shortening the pulse train of the IS. The nominal IS pulse train is a two bipolar Tx pulses of 10 ms, each followed by a 10 ms data acquisition window; totaling 40 ms. QFS measured the sensor response of the IS to a standard target, for Tx/ACQ windows of 10, 7, 5, and 2 ms; Figure 9.4 below. The magnitude of the sensor response, across the whole acquisition window, is decreased roughly linearly with Tx pulse width. Late time data is also lost for cases of shorter windows, by virtue of not digitizing the data.

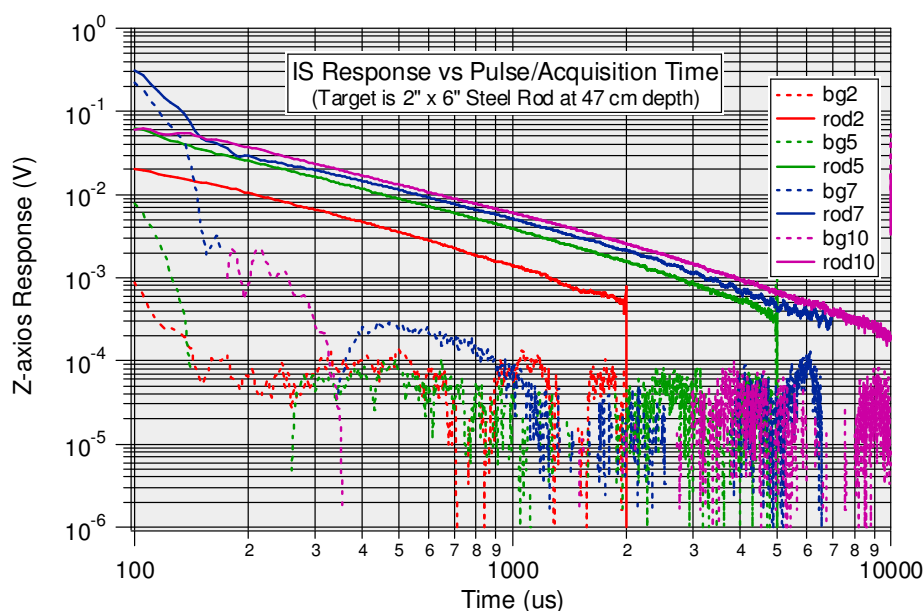


Figure 9.4 - Sensor response to a vertical steel rod, at 47 cm below, for varying Tx pulse/acquisition windows. SNR goes roughly linearly with pulse width. The legend symbol “bg” stands for background response (dashed line) when there was no target.

QFS also measured the variation on the IS background, over time, for varying IS parameters. The parameters varied were pulse width/acquisition window/averaging, with three configurations tested: 5/5/10, 10/10/10, and the nominal 10/10/20. The results of this experiment are shown below in Figure 9.5, along with the standard deviation of each experiment (caption). The nominal configuration, 10/10/20, has the lowest variation; however the increase in variation for 5/5/10 and 10/10/10 is small (<2).

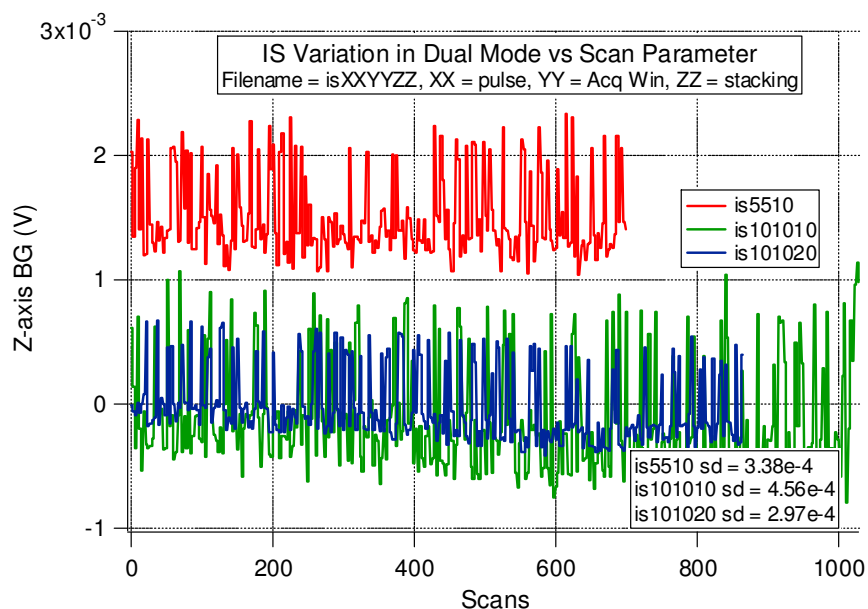


Figure 9.5 - Background variation of IS for varying pulse train parameters, along with standard deviation of each experiment. The nominal configuration, 10/10/20, has the least variation.

If spatial resolution better than 0.125 m is required, it seems possible to decrease the system scan time. A 5/5/10 pulse train could be employed, which would result in a 300 ms total scan time for dual-mode operation; yielding spatial resolution of 0.075 m. Though the current software does not allow unequal Tx pulse and acquisition window times, these two parameters could be controlled separately in the future system. If the TD3D model only needs 2-3 ms response data, the acquisition window could be shortened further. For example, if the IS ran a 5/3/10 pulse train, the spatial resolution is improved to 0.065 m.

In studying the dual-mode operation, QFS revisited the concept of true interleaved operation. That is, the possibility of collecting FG data during the IS pulse - sketched in Figure 9.6 (top), as opposed to the serial time sharing currently employed for dual-mode operation, sketched in Fig. 9.6 (bottom). Currently the time constant of this turn-on/turn-off is ~ 10 ms. Assuming 3 time constants for stability (on each end of the FG data collection), and at least 10 ms of FG acquisition, the FG requires at least 100 ms. Thus, while it is theoretically possible to collect FG data during the Tx pulse, the pulse would need to be ~ 100 ms. This is undesirable given the need to minimize total scan time. It therefore seems practical to continue the serial time sharing currently employed.

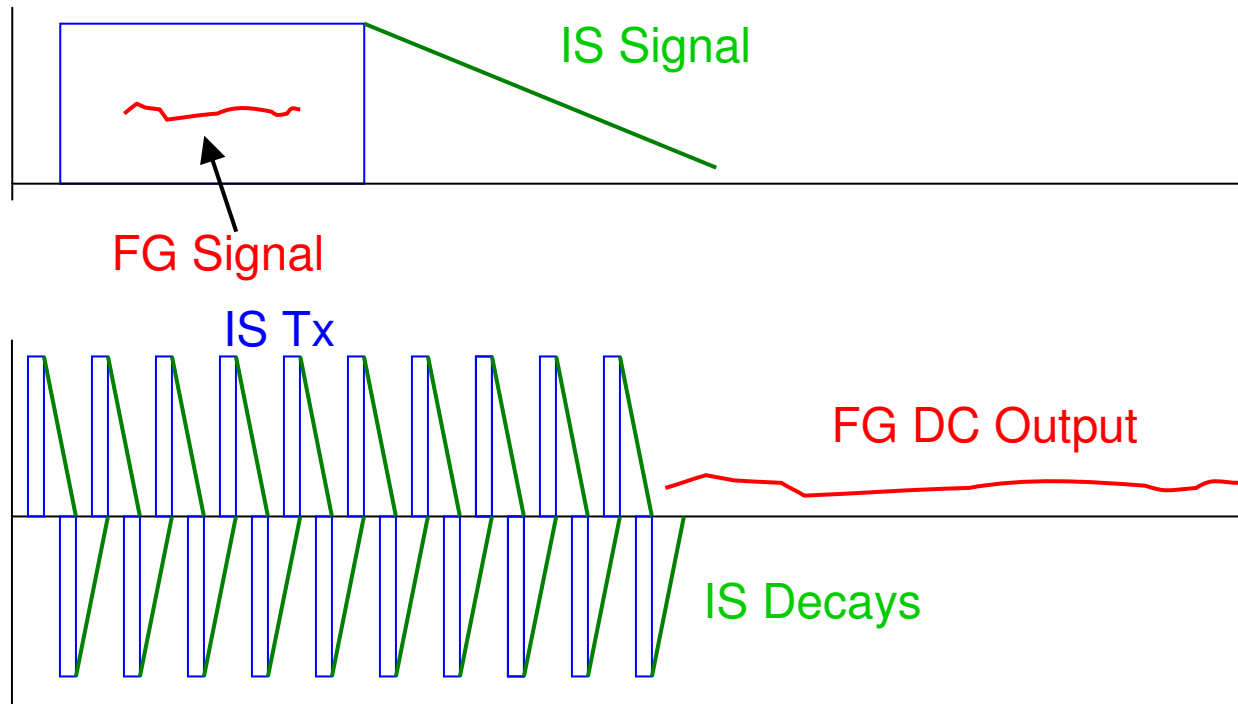


Figure 9.6 - Top: Concept for true interleaved operation, FG acquisition during IS Tx pulse. Bottom: Serial time sharing employed by current system.

We studied the deployment concept of the dual-mode receiver. The goal of the sensor system is to collect data continuously with “scan-in-motion” operation. A single pass would both detect and discriminate suspect objects. One operational concept is to run serial time sharing dual-mode (STSDM) continuously while passing over a suspect target. This method yields between 0.25 and 0.065 m of spatial resolution, but means that there are gaps in the IS data while passing over the target. A second possibility is to run the system in detection/discrimination mode (DDM), where the system scans continuously in FG mode until a suspect object is found. This detection triggers the system changing into continuous IS discrimination mode for some time, illustrated below in Figure 9.7. The benefit of DDM is that the system collects maximized IS data over a suspect object and thereby improves the discrimination capability of the system. DDM also has the potential benefit of decreasing the power draw of the system, since it is the IS transmitter which consumes the most power. If the FIS runs in DDM with a 10/10/10 pulse train for the IS, that would give 0.1 m spatial resolution; and 0.05 m resolution for a 5/5/10 pulse train.

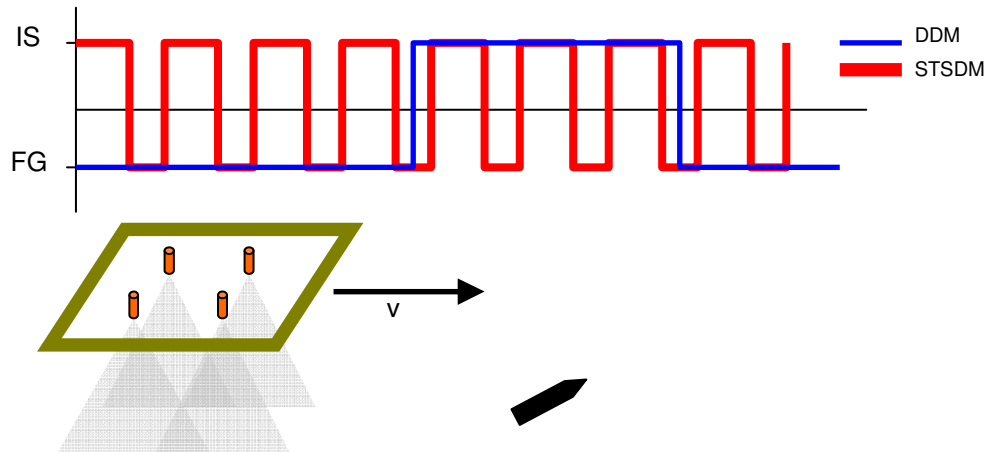


Figure 9.7 - Concept for running the FIS in a detection/discrimination mode rather than continuous serial time sharing dual mode; maximizes IS data collection (and thus discrimination) while over suspect objects.

9.4 Environmental effects

There were question regarding the outdoor operation of the system. Specifically, the questions that QFS sought to answer were:

- 1) What effects, if any, will arise from outdoor operation?
- 2) What effects will the proximity of the ground have on the FIS background and target signals?
- 3) If there are effects from the ground, will they vary based on time, location, weather, etc?
- 4) Will there be induced noise or signal degradation in a moving sensor?

The first step in answering question 1 was simply to take the FIS system outdoors on its new cart and perform some checks. With the system stationary, the FIS was able to run, reliably subtract the background, and show a recognizable response to a target. QFS buried the steel pipe used in indoor data collection at a depth of 47 cm in the soil behind the QFS facility. A study of system warming was made, both over a target and over bare ground. The system was taken outside in a “cool state”, having been shut off and sitting in the climate controlled lab. Several scans were made over the bare ground/target ground, then the system was moved aside, turned off, and left to warm in the sun. After several hours, the system was repositioned over the original site, and several more scans were performed. The z-axis sensor response for the hot/cold experiments with the system over bare ground (top) and over a buried target (bottom) is shown in Figure 9.8. Only minor variation is seen, part of which is explained by $\sim 10 \mu\text{s}$ of jitter in the triggering (seen in there data sets). It appears that sun heating is not an issue of concern.

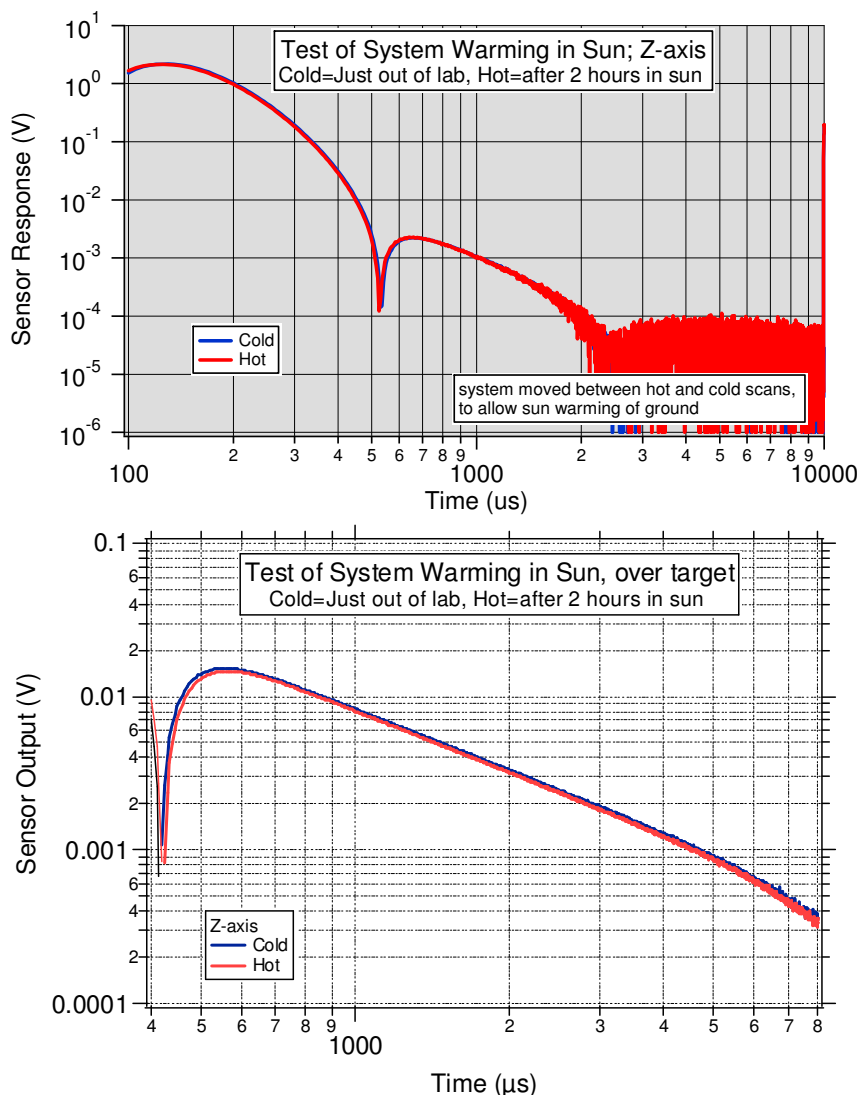


Figure 9.8 - Sensor response over bare ground (top) and over buried target (bottom) with the sensor “cold” (straight from the lab) and “hot” (after warming in the sun several hours).

We investigated questions 2 and 3, whether the proximity of the ground had any effects, and whether these effects (if any) changed with time, weather, or location. There was a concern that the conductive ground might have a shielding effect, resulting in diminished target signals. We did a direct comparison of the target signal between a buried target and one on test grid, shown in Figure 9.9. Aside from some deviation around 200 μ s (likely due to imperfect background subtraction) the signals are identical. More study on the subject will be needed for the field demonstration, with different soil types, but the initial indication is that the ground does not interfere with system performance.

We also carried out a study of wet versus dry ground, with the expectation that saturated ground should have a higher conductivity than dry ground. The system was set over a patch of soil and several scans were performed. The system was then moved aside and the soil was saturated with

5 gallons of water. The system was repositioned over the site and set to run for some time as the water drained through the soil. The results of the wet soil test are shown Figure 9.10; no significant variation is seen in the z-axis background. Once again, further study of soil conductivity is warranted; however initial indications are that it plays an insignificant role.

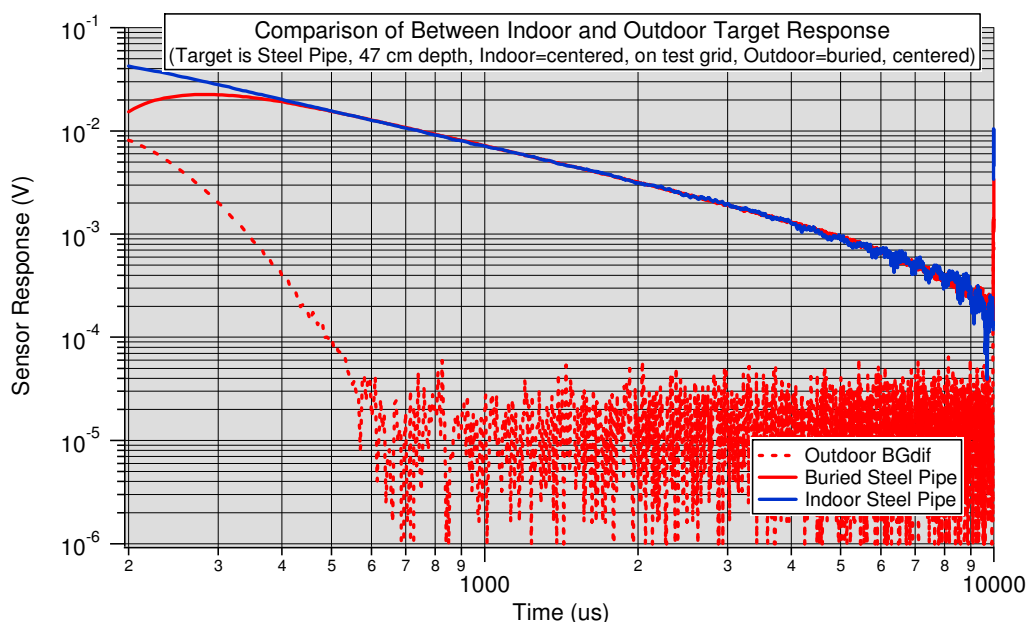


Figure 9.9 - Comparison of sensor response to steel pipe buried and on test grid; no significant difference is seen.

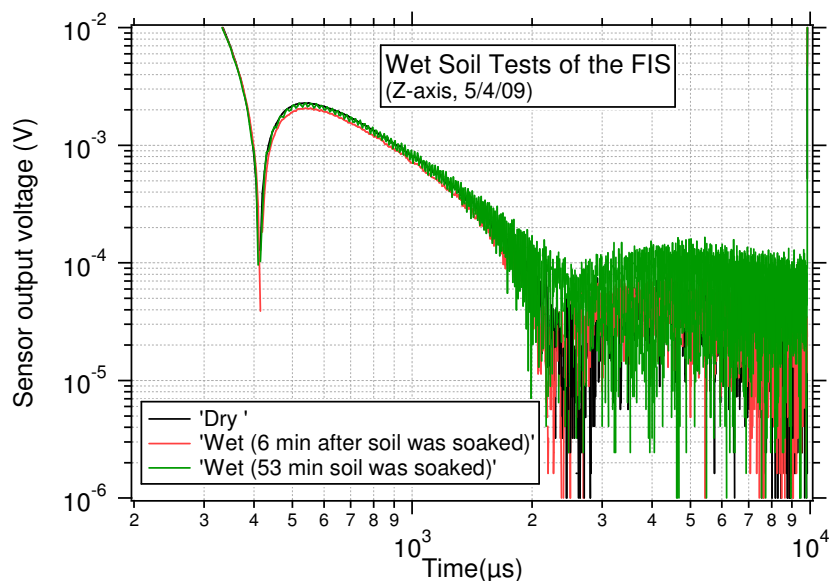


Figure 9.10 - Z-axis IS background outdoors for dry, wet, and drying soil; no significant difference is seen.

To characterize IS variation outdoors as a function of time and location, QFS carried out a multi-day background data collection. Data were collected twice daily at two sites over 3 days. This experiment shows variation between 1 spot and another, and also shows how a spot changes with time and day. Figure 9.11 (top) shows all the runs at 1 site, over 3 days; traces are $dXrY$, where d is day and r is run number in a given day (1 or 2). One trace appears to stand out slightly from the rest, but no significant variation is seen between any of these runs. Fig. 9.11 (bottom) shows data on Day 3, at both sites. Some minor variation is also seen here, but still quite small. The variation seen here is small relative to the target signal.

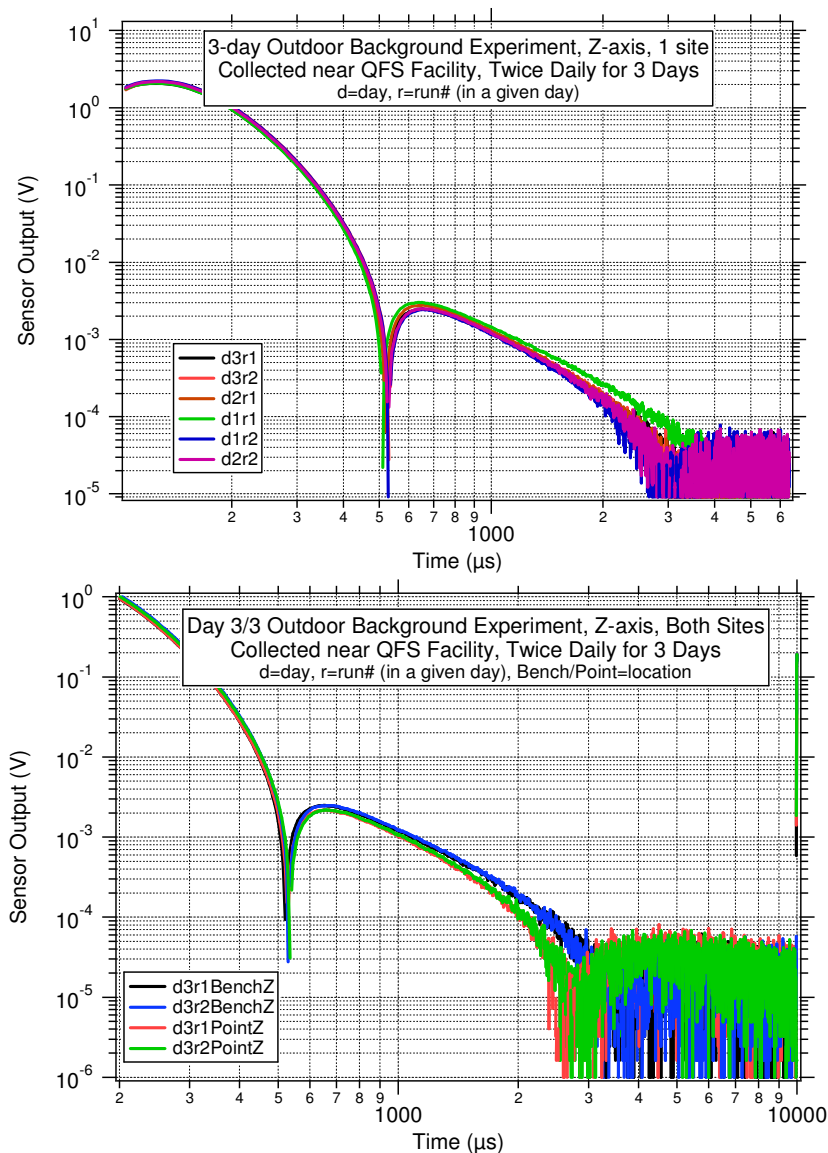


Figure 9.11 - Top: 3-day background collection at 1 site. Bottom: Day 3/3 at both sites. Data was collected twice daily (10 am, 3pm) over 3 days. No significant variation is seen.

9.5 Motion effects

QFS sought to study the effects of moving the induction sensor on the signal and background. The next phase system will have some vibration damping and possibly other motion-induced noise mitigation capabilities. To simulate a “smooth” ride, an experiment was first carried out in the QFS parking lot. The sensor was set over asphalt to run for ~ 5 min. Next the sensor was moved slowly (~ 0.5 m/s) over the concrete. In both cases a 10/10/10 pulse train was used, with 0.5 s of wait between each run. The strength of the background signal, at the time gate of 500 μ s, is plotted for each experiment run in Figure 9.12. The drawback of moving is that the background can change as a function of position. A large spike is seen in the moving data around run 50. This spike is likely due to proximity to a large metal object on the ground as it persists over several data sets. Furthermore the sensor was moved along the QFS parking lot, adjacent to the QFS facility. After ~ 100 runs, the building ends and the driveway continues on and around a corner. Neglecting the spike in the moving data around run 50, and the increased noise following run 100, the noise in both curves does not appear to be different. This experiment was run several times, and similar results (data not shown) were achieved. We conclude that motion-induced noise is very small for the induction mode.

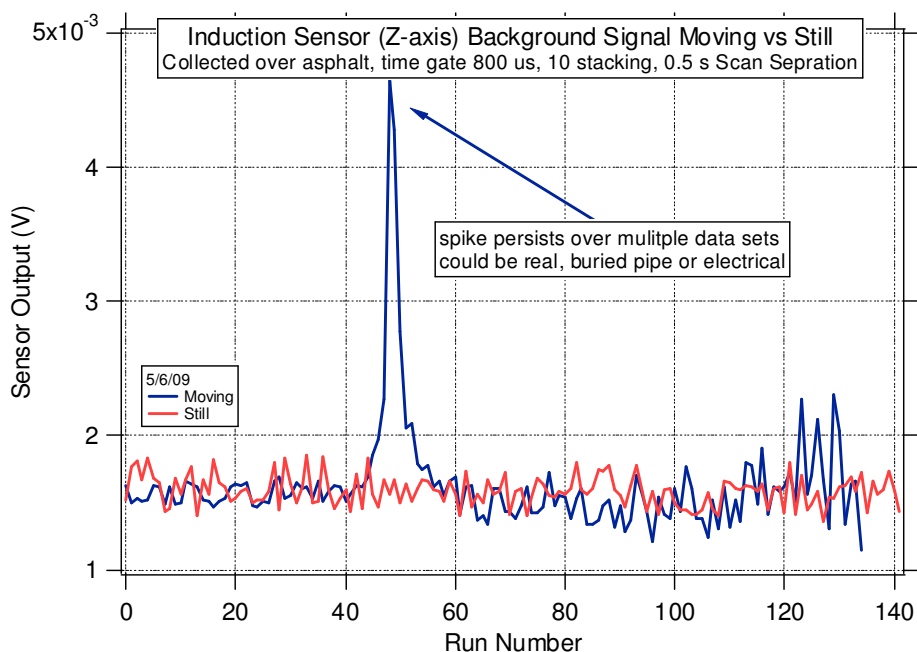


Figure 9.12 - Comparison of IS noise while moving (blue) with the system stationary, over asphalt in QFS back parking. Neglecting several anomalies, noise performance appears roughly similar.

QFS also measured the response of a moving sensor over a buried target, the item of principal interest to the program. The receiver system was moved, slowly and continuously, over the buried steel pipe, using a 10/10/10 pulse train. The data were collected with a pause of 0.5 s between scans to simulate STSDM, and one of 0 s between scans, to simulate DDM. The sensor response at 500 μ s for these two experiments is shown in Figure 9.13. In both cases the peak (centered) signal level is ~ 10 mV, similar to the stationary data set. Also in both cases, the background level (outer edges of peak) appears roughly similar. The DDM appears much cleaner

and has more resolution on the target; it may be the favored mode of operation for the next phase system.

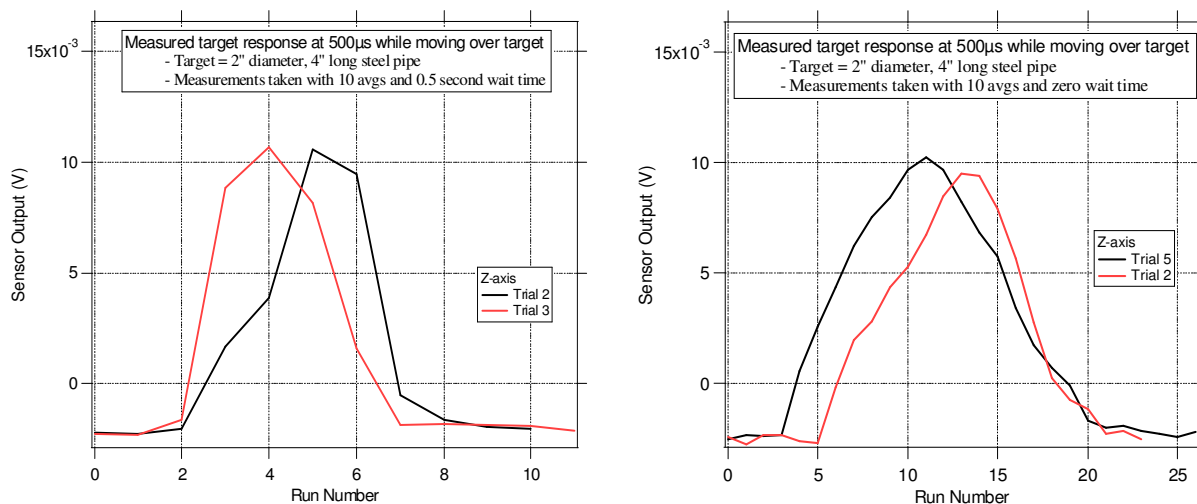


Figure 9.13 - Sensor induction response to buried steel pipe, at 47 cm, as the sensor is moved continuously over the target, a 10/10/10 pulse train was used. Left: 0.5 s wait between runs. Right: 0 s wait between runs.

9.6 Conclusions on field deployment issues

Following the completion of system performance study in Year 4, we addressed some practical issues for future field deployment. We sought to make improvements to the prototype receiver design and to inform the design of the next phase system, with a view to outdoor, mobile operation. An outdoor DAQ system based on a laptop platform was developed. A current monitor was installed on the transmitter coil to compensate IS background drift due to the power droop in the Tx batteries. Spatial resolution of a scan-in-motion system was calculated to be ~ 0.125 m with 0.5 m/s moving speed, but can be reduced further with a multi-sensor array or a reduced Tx pulse width. Multiple experiments were conducted to test background signals generated in the ground and their variation based on time, location, heating, and soil moisture content. No obvious variation was seen for the Z-axis response between wet and dry ground as a function of time and location, or after heating in the sun.

10. CONCLUSIONS AND IMPLICATIONS FOR FUTURE RESEARCH

The goal of the project was to develop a dual-mode receiver based on a high-permeability core coil and demonstrate that the receiver has a suitable performance for UXO detection and discrimination application.

During the project, we built a dual-mode receiver, and demonstrated that a fluxgate and induction sensor can be combined in a single package and yield useful information on detection of deep targets and discrimination of shallow ones. The technical feasibility was demonstrated through the following results:

- 1) It is feasible to use a *high-permeability* compact induction sensor for a time-domain UXO EM detection system
 - Although the primary pulse field induces eddy currents in the sensor core, this challenge can be solved with proper coil design, fast cores, anti-pulsing, and digital subtraction.
 - Demonstrated a compact induction sensor with an impulse response to a primary pulse field decaying from a peak field of 0.1 mT to 100 pT within 100 μ s (Year 1 milestone).
- 2) Demonstrated a prototype of the compact single-axis sensor that operates in both the induction mode and the fluxgate mode (Year 1 Milestone 2). The fluxgate was constructed with the same core material and preamplifier as the induction sensor with noise of 100 pT/rtHz at 1 Hz, and 0.9 nT RMS noise in the band of DC to 30 Hz.
- 3) System study indicates that the FIS sensor has enough bandwidth and sensitivity to detect UXO targets.
- 4) Verified dual-mode sensor meets performance requirements (Year 2 Milestone 1)
 - Developed a complete dual-mode induction-fluxgate sensor system prototype with dual-mode coil, an integrated circuit board, and PC software.
 - Demonstrated a dual-mode sensor with RMS noise of 1 nT in fluxgate (DC) mode and a few pT in induction (AC) mode.
 - The sensor performance has been quantified by comparing it with a Geonics EM63 (in the induction mode), and with a commercial fluxgate that has a 1 nT sensitivity: showing comparable detection of the 37-mm shell at a distance of 0.5 to 1 m.
- 5) Demonstrated a true dual-mode operation and detection with serial time-sharing between two sensing modes
 - Optimum gating time for fluxgate and induction sensor modes with *serial* time-sharing was found to be about 1 s with 40 ms x 20 stacking for induction mode and 50 ms for fluxgate mode.
 - True dual-mode operation with serial time sharing was demonstrated with a 37-mm shell moved slowly on the testing grid.
- 6) Developed an integrated 3-axis, dual-mode prototype system
 - Similar sensitivity was achieved as the single-axis sensor.
 - Verified the operation of the 3-axis FIS.
 - Demonstrated the 3-component EM data give more robust results in target characterization than 1-component data.

- 7) Quantified the system performance on an indoor test grid, with 3-axis EM and Mag data collected for canonical and typical UXO targets,
 - The discrimination performance in the induction mode is comparable to that achieved by *Grimm* (2003) using the EM-61-3D at the Blossom Point test grid (PD = 91%, PFA = 32% for 3-axis models).
 - The sensor data result very high quality sphere fits and the relatively accurate target locations and depths, in fluxgate mode.
 - Simple magnetization models of vertical or total-field data are capturing the vast majority of the data structure.
- 8) Studies on some practical issues confirmed the feasibility for deploying FIS:
 - A current monitor on the Tx coil can compensate IS background drift due to the power droop in the Tx batteries.
 - The prototype system can achieve a spatial resolution of 0.125 m with 0.5 m/s moving speed, but can be reduced further with a multiple sensor configuration or a reduced Tx pulse width.
 - Testing data shows the sun heating does not change the receiver response.
 - No obvious variation is observed for the Z-axis induction response between wet and dry ground, and as a function of time and location.

The dual-mode, 3-axis fluxgate induction sensor system is very attractive as a commercial product for the next generation UXO discriminator. No similar system is available even as a research prototype. The compact design of the receiver coil also makes it feasible to construct a sensor array.

Future Research

The prototype receiver developed under SERDP MM-1444 can be transitioned into a field deployable unit with identical or improved performance. The re-engineered sensor system will have: a moveable platform, a ruggedized mechanical assembly with vibration isolation, a GPS and IMU for position and orientation identification, and a compact low power DAQ with control and interface software. The field systems will be capable of performing multi-axis, dual-mode measurement during one-pass surveys for buried UXO targets. An array of 3-axis sensors will be considered to improve the detection sensitivity and reduce the scan time.

Collaborating with Sky Research, QFS plans to propose an ESTCP program to engineer a field deployable system based on the prototype receiver developed under this project, execute a field demonstration at a standard UXO demonstration site, and assess operational cost. The program will transition the sensor technology from a R&D prototype to a commercial product.

LITERATURE CITED

- Billings, S.* (2004), "Discrimination and Classification of Buried Unexploded Ordnance Using Magnetometry", *IEEE Trans. Geosci. Remote Sens.*, 42, 1241-1251.
- Billings, S. et al.* (2006), "Magnetic Models of Unexploded Ordnance", *IEEE Trans. Geosci. Remote Sens.*, 44, 2115-2124
- BUD*, "Berkeley UXO Discriminator" developed by Berkeley National Laboratory, Gasperikova, E., "ESTCP Project MM-0437 Final Report at Camp Sibert – Gadsden, Alabama", November 2008
- Grimm, R.E. and T.A. Sprott*, (2002) "Model-Based Sensor Design Optimization for UXO Classification", *Proceeding of the UXO Forum*
- Grimm, R.E.* (2003), "Triaxial Modeling and Target Classification of Multichannel, Multicomponent EM Data for UXO Discrimination", *J. Environ. Eng. Geophys.*, 8, 239-250.
- Miller, J., Bell, T, and Soukup, J.*, "Simple Phenomenological Models for Wideband Frequency-Domain Electromagnetic Induction", *IEEE Trans Geosci. Remote Sens.*, 39, 1294-1298, 2001.
- MTADS*, "Multi-Sensor Towed Array Detection System" developed by Naval Research Lab, ESTCP Project UX-9812 Cost and performance Report, "Electromagnetic Induction and Magnetic Sensor Fusion for Enhanced UXO Target Classification", March 2001,
- MSEMS*, "Man-Portable Simultaneous Magnetometer and EM System" developed by SAIC and USACEH, ESTCP Project MM-0414 Final report "Man-Portable Simultaneous Magnetometer and EM System (MSEMS)", Dec 2008,
- McNeill, J.D. and M. Bosnar*, (1996), "Application of Time Domain Electromagnetic Techniques to UXO Detection", *Proceeding of the UXO Forum*, 34-42
- McNeill, J.D.*, (2008), personal communication
- MetalMapper*, Snyder, D.D. "Skip", et al. (2008) "The Data Processing Challenge Posted by Advanced TEM Systems", presented on Partners in Environmental Technology Technical Symposium & Workshop, Washington DC, Dec. 2-4 , Section 3A
- Pasion, L.R. and D.W. Oldenburg* (2001), "Locating and Determining Dimensionality of UXO's Using Time Domain Electromagnetic Fields", *J. Environ. Eng. Geophys.* 6, 91-102
- Ripka, P.* (1992), "Review of Fluxgate Sensors", *Sensor and Actuators A*, **33**,129-141
- Shubitidze, F., O'Neill, K., Haider, S., Sun, K., and Paulsen, K.D.* (2002). "Application of the Method of Auxiliary Sources to the Wideband Electromagnetic Induction Problem," *IEEE Transaction on Geoscience and Remote Sensing*, vol 40, No 4, 928-942.
- Wold, R., D. George, R. Grimm, D. Johnston, and A. Becker* (2003) "EM and Magnetic (Dual-Mode) System for Detection and Classification of UXO", *UXO/Countermine Forum*.
- Zhang, Y.M. et al*, (2005) "Compact, Low-Noise Magnetic Sensor with Fluxgate (DC) and Induction (AC) Modes of Operation", presented on Partners in Environmental

Technology Technical Symposium & Workshop, Washington DC, Nov. 29 - Dec. 1,
Poster #128

Zhang, Y.M, Hibbs, A.D., Grimm, R.E. (2008), “Integrated Fluxgate-Induction Sensor”, US
Patent 7,391,210 B2

APPENDICES

List of Scientific/Technical Publications

Zhang, Y.M., Hibbs, A.D., Grimm, R.E., and Marrakchi, D. (2005) “Compact, Low-Noise
Magnetic Sensor with Fluxgate (DC) and Induction (AC) Modes of Operation”, presented
at *Partners in Environmental Technology Technical Symposium & Workshop*,
Washington DC, Nov. 29 - Dec. 1, Poster #128

Zhang, Y.M., Steiger, M., Hibbs, A.D., Marrakchi, D. , and Grimm, R.E. (2007), “Compact
Fluxgate-Induction Sensor for Advanced Time-Domain UXO Detection System”,
presented at the “*UXO/Countermining/Range Forum 2007*” (August 27-30, 2007, Orlando,
Florida), Section 18

Zhang, Y.M., Steiger, M., Hibbs, A.D., Grimm, R.E., Sprott, T.A. (2008), “Tri-Axial Fluxgate-
Induction Sensor for Advanced Time-Domain UXO Detection and Discrimination”,
presented at *Partners in Environmental Technology Technical Symposium & Workshop*,
Washington DC, Dec. 2-4 , 2008, Section 4C, [http://www.serdp
estcp.org/Symposium2008/Sessions/upload/4C_Zhang.htm](http://www.serdpeestcp.org/Symposium2008/Sessions/upload/4C_Zhang.htm)

Zhang, Y.M, Hibbs, A.D., Grimm, R.E. (2008), “Integrated Fluxgate-Induction Sensor”, US
Patent 7,391,210 B2

Zhang, Y.M., Steiger, M., Marrakchi, D., Hibbs, A.D., Grimm, R.E., Sprott, T.A., “Dual-mode,
Fluxgate-Induction Sensor Receiver for Future UXO Detection and Discrimination”,
manuscript submitted to *Journal of Environmental & Engineering Geophysics* (July
2009)